



**NTNU – Trondheim**  
Norwegian University of  
Science and Technology

# On Determination of $G_{\max}$ by Bender Element and Cross-Hole Testing

**Mirjam Knutsen**

Civil and Environmental Engineering

Submission date: June 2014

Supervisor: Steinar Nordal, BAT

Norwegian University of Science and Technology  
Department of Civil and Transport Engineering





Report Title: On Determination of $G_{\max}$ by Bender Element and Cross-Hole Testing	Date: 09.06.2014		
	Number of pages (incl. appendices): 243		
	Master Thesis	<input checked="" type="checkbox"/>	Project Work
Name: Mirjam Knutsen			
Professor in charge/supervisor: Steinar Nordal			
Other external professional contacts/supervisors:			

**Abstract:** The small-strain shear modulus,  $G_{\max}$ , is an important parameter in geodynamic problems and for advanced modelling.  $G_{\max}$  is influenced by several factors, which complicates the assessment and interpretation of test results. Due to sample disturbance, values measured in the laboratory may be lower than in the field. The use of  $G_{\max}$  as a measure of sample disturbance has previously been investigated.

Different testing methods for determination of  $G_{\max}$  are described in this thesis, with a presentation of advantages and limitations on the basis of literature. Field tests can be performed either from the ground surface or in boreholes. For determination of  $G_{\max}$  in the laboratory, the use of bender elements in conventional test devices, such as the triaxial apparatus, has become a common procedure. With bender elements, several repetitive tests can be performed, and the sample can subsequently be tested for other soil characteristics.

The initial part of this study concerned implementation of bender elements in a triaxial apparatus at the NTNU geotechnical laboratory. Subsequently, determination of  $G_{\max}$  by bender element testing was emphasized. Clay samples from three different sites were used, the Stjørdal, Tiller and Esp sites. At the Esp site, a limited field testing program was also performed, using a cross-hole method for determination of in situ  $G_{\max}$ . Laboratory measurements on two samples of Esp clay gave  $G_{\max}$  of 27 MPa and 30 MPa, after long-term consolidation. In situ measurements gave consistent results, with an average  $G_{\max}$  of 47 MPa. Values measured in the laboratory are seen to be about 40 % lower than values measured in the field. However, it should be noted that in the bender element test, the direction of propagation of the s-wave is vertical, while in the cross-hole test, it is horizontal. Consequently, due to anisotropy, a direct comparison may be somewhat erroneous.

Factors influencing  $G_{\max}$  are presented on the basis of literature. Void ratio, plasticity index and soil structure are seen to be important factors.  $G_{\max}$  also show a stress dependency, increasing with increasing overburden pressure. Literature regarding  $G_{\max}$  as a measure of sample disturbance is also presented.

For evaluation of the development of  $G_{\max}$  with time, long-term consolidation was performed. An evident increase in  $G_{\max}$  with time of consolidation was observed, with a correlation to axial strain. This is assumed to be due to aging effects, bringing the sample closer to its in situ state. Observations also showed a larger increase for 54 mm tube samples than for block samples, indicating some correlation between sample quality and  $G_{\max}$ . Reconsolidation seems to compensate for some effects of disturbance. However, it is suggested that destructuration of the soil is an important factor of sample disturbance which is not eliminated by reconsolidation.

Bender element testing of the Esp clay was also performed on a sample of half height (5 cm). The results showed  $G_{\max}$  values about 25 % lower than those of the full-height samples. This indicates the existence of some near-field effects influencing the shear wave velocity close to the elements.

Interpretation of cross-hole results revealed some difficulties regarding identification of the shear wave. The equipment should be further developed so that receivers are in direct contact with the soil. Lack of knowledge regarding an assumed complex environment in the triaxial cell, may have been a limitation when interpreting laboratory results. A model of the bender element test in a finite element method program, such as Plaxis, may be of interest for investigation of the actual condition of wave propagation. Further work is also proposed regarding the use of  $G_{\max}$  as a measure on sample disturbance.

Keywords:

1. Small-strain shear modulus, $G_{\max}$
2. Bender elements
3. Field and laboratory testing
4. Sample disturbance
5. Geodynamics



## Preface

This study is performed as a Master's Thesis in the specialization course TBA4900 Geotechnics. The thesis is part of the MSc in Civil and Environmental Engineering, and is written at the Geotechnical Division, Department of Civil and Transport Engineering at the Norwegian University of Science and Technology (NTNU).

Main supervisor of the study has been Professor Steinar Nordal.

The thesis is a continuation of the author's specialization project thesis regarding implementation of bender elements in a triaxial apparatus at the NTNU geotechnical laboratory. The project was written in the Autumn of 2013, and was limited to some pilot tests. This study is performed in the Spring of 2014, with a duration of 21 weeks.

The report deals with the topic of geodynamics, particularly the small-strain shear modulus  $G_{max}$ , which is an important dynamic soil property. Laboratory tests have been performed, supplemented by limited field testing. The first part of the report presents theory regarding dynamic soil behavior and wave propagation. Methods for determination of  $G_{max}$ , and the issues of factors influencing  $G_{max}$  and sample disturbance are presented on the basis of literature. The second part of the report presents the laboratory and field testing which has been performed during the study. Lastly, a discussion regarding test results is given.

My interest in the subject has grown during the study, and the work has provided both practical and theoretical knowledge.

Trondheim, June 2014

---

Mirjam Knutsen



## Acknowledgments

I would like to thank the following persons for their great help during this study:

Steinar Nordal, for always welcoming me into his office when I have asked for help. He has been a great supervisor, helping me with literature work, interpretation, and giving clarifying explanations when I have found things difficult.

Per Asbjørn Østensen, for invaluable help and work. He has developed computer software for both bender element and cross-hole testing, and additional equipment used for cross-hole testing. He has also been a great help in the laboratory, teaching me a lot regarding the triaxial setup. He has always made time for me, and I could not have done this study without his effort.

Gudmund Eiksund, for being available for interpretation and discussion of test results.

Helene A. Kornbrekke, for valuable help and guidance in the laboratory.

Anders Samstand Gylland, for providing block samples from Tiller and Esp, and placing the cross-hole setup at the site, together with Gunnar Winther.

Everyone in the workshop at the Geotechnical Division who has been involved in the work concerning the modification of a triaxial apparatus for fitting of bender elements.

All my friends who I have shared an office with, especially Madeleine, Bjørn Kristian, Vegard and Guro, for their contributions to a good academic and social environment. We have shared many good times and discussions, which has made the work easier and more fun. A special thank you to my boyfriend, Martin, who has supported me and given much joy to the everyday work.





## Abstract

The small-strain shear modulus,  $G_{max}$ , is an important parameter in geodynamic problems and for advanced modelling.  $G_{max}$  is influenced by several factors, which complicates the assessment and interpretation of test results. Due to sample disturbance, values measured in the laboratory may be lower than in the field. The use of  $G_{max}$  as a measure of sample disturbance has previously been investigated.

Different testing methods for determination of  $G_{max}$  are described in this thesis, with a presentation of advantages and limitations on the basis of literature. Field tests can be performed either from the ground surface or in boreholes. For determination of  $G_{max}$  in the laboratory, the use of bender elements in conventional test devices, such as the triaxial apparatus, has become a common procedure. With bender elements, several repetitive tests can be performed, and the sample can subsequently be tested for other soil characteristics.

The initial part of this study concerned implementation of bender elements in a triaxial apparatus at the NTNU geotechnical laboratory. Subsequently, determination of  $G_{max}$  by bender element testing was emphasized. Clay samples from three different sites were used, the Stjørdal, Tiller and Esp sites. At the Esp site, a limited field testing program was also performed, using a cross-hole method for determination of in situ  $G_{max}$ . Laboratory measurements on two samples of Esp clay gave  $G_{max}$  of 27 MPa and 30 MPa after long-term consolidation. In situ measurements gave consistent results, with an average  $G_{max}$  of 47 MPa. Values measured in the laboratory are seen to be about 40 % lower than values measured in the field. However, it should be noted that in the bender element test, the direction of propagation of the s-wave is vertical, while in the cross-hole test, it is horizontal. Consequently, due to anisotropy, a direct comparison may be somewhat erroneous.

Factors influencing  $G_{max}$  are presented on the basis of literature. Void ratio, plasticity index and soil structure are seen to be important factors.

$G_{max}$  also show a stress dependency, increasing with increasing overburden pressure. Literature regarding  $G_{max}$  as a measure of sample disturbance is also presented.

For evaluation of the development of  $G_{max}$  with time, long-term consolidation was performed. An evident increase in  $G_{max}$  with time of consolidation was observed, with a correlation to axial strain. This is assumed to be due to aging effects, bringing the sample closer to its in situ state. Observations also showed a larger increase for 54 mm tube samples than for block samples, indicating some correlation between sample quality and  $G_{max}$ . Reconsolidation seems to compensate for some effects of disturbance. However, it is suggested that destructuration of the soil is an important factor of sample disturbance which is not eliminated by reconsolidation. It may not be possible for samples in the laboratory to recover the in situ structure, which is created by sedimentary effects over a geologic period of time.

Bender element testing of the Esp clay was also performed on a sample of half height (5 cm). The results showed  $G_{max}$  values about 25 % lower than those of the full-height samples. This indicates the existence of some near-field effects influencing the shear wave velocity close to the elements.

Interpretation of cross-hole results revealed some difficulties regarding identification of the shear wave. The equipment should be further developed so that receivers are in direct contact with the soil. Lack of knowledge regarding an assumed complex environment in the triaxial cell, may have been a limitation when interpreting laboratory results. A model of the bender element test in a finite element method program, such as Plaxis, may be of interest for investigation of the actual condition of wave propagation. Further work is also proposed regarding the use of  $G_{max}$  as a measure on sample disturbance.

# Contents

Preface . . . . .	v
Acknowledgment . . . . .	vii
Summary and Conclusions . . . . .	x
<b>1 Introduction</b>	<b>1</b>
1.1 Background . . . . .	1
1.2 Task Description . . . . .	2
1.2.1 Objectives . . . . .	3
1.3 Approach . . . . .	3
1.4 Structure of the Report . . . . .	4
<b>2 Theory</b>	<b>5</b>
2.1 Stress-Strain Behavior of Cyclically Loaded Soils . . . . .	5
2.1.1 Energy Dissipation and Hysteretic Damping . . . . .	6
2.1.2 Damping Ratio . . . . .	9
2.2 Wave Propagation . . . . .	10
2.2.1 Equation of Motion and Frequency Independent Shear Modulus . . . . .	10
2.2.2 Seismic Waves . . . . .	13
2.3 Equivalent Linear Model . . . . .	18
2.3.1 Shear Modulus . . . . .	20
<b>3 Small-Strain Shear Modulus</b>	<b>21</b>
3.1 Laboratory Tests . . . . .	22

3.1.1	Resonant Column Test . . . . .	22
3.1.2	Bender Element Test . . . . .	24
3.1.3	Torsional Simple Shear Test . . . . .	27
3.2	Field Tests . . . . .	28
3.2.1	Seismic Reflection Test . . . . .	29
3.2.2	Seismic Refraction Test . . . . .	30
3.2.3	Steady-State Vibration (Rayleigh Wave) Test . . . . .	34
3.2.4	Spectral Analysis of Surface Waves Test . . . . .	35
3.2.5	Multichannel Analysis of Surface Waves Test . . . . .	36
3.2.6	Seismic Cross-Hole Test . . . . .	37
3.2.7	Seismic Down-Hole (Up-Hole) Test . . . . .	40
3.2.8	Seismic Cone Penetration Test . . . . .	41
3.2.9	Shear Beam as Energy Source . . . . .	44
3.3	Soil Parameters influencing $G_{max}$ . . . . .	46
3.3.1	Overconsolidation Ratio . . . . .	47
3.3.2	Stress State . . . . .	48
3.3.3	Void Ratio . . . . .	50
3.3.4	Anisotropy . . . . .	51
3.3.5	Time of Consolidation . . . . .	54
3.3.6	Plasticity Index . . . . .	56
3.3.7	Stress and Strain History . . . . .	58
3.3.8	Soil Structure . . . . .	59
<b>4</b>	<b><math>G_{max}</math> as a Measure of Sample Disturbance</b>	<b>63</b>
4.1	Conventional Method for Sample Quality Assessment . . . . .	64
4.2	Use of Shear Wave Velocity to Assess Sample Disturbance . . . . .	65
4.2.1	Use of Portable Bender Elements for $v_s$ Measurements in Field . . . . .	66
4.2.2	Combination of Shear Wave Velocity and Suction Measurements for Sample Quality Classification . . . . .	68
<b>5</b>	<b>Installation of Bender Elements in a Triaxial Apparatus</b>	<b>71</b>
5.1	Bender Element Specifications . . . . .	71

5.2	Programming Signal and Interface . . . . .	72
5.3	Prior Testing of Bender Elements . . . . .	73
5.4	Equipment Setup . . . . .	74
<b>6</b>	<b>Material and Procedures of Seismic Cross-Hole Testing</b>	<b>77</b>
6.1	The Esp Site . . . . .	78
6.2	The Esp Material . . . . .	78
6.3	Cross-Hole Test Setup . . . . .	80
6.4	Performance of the Cross-Hole Test . . . . .	81
6.4.1	Verticality Check of Tubes with Accelerometers . . .	81
6.4.2	Producing and Registration of Seismic Signal . . . .	83
<b>7</b>	<b>Material and Procedures of Bender Element Testing</b>	<b>85</b>
7.1	Consolidation and Shear Test . . . . .	86
7.2	Interpretation of Tests . . . . .	88
7.3	Testing on Stjørdal clay . . . . .	89
7.3.1	The Stjørdal Site . . . . .	89
7.3.2	The Stjørdal Material . . . . .	89
7.3.3	Consolidation . . . . .	90
7.3.4	Shear Test . . . . .	91
7.4	Testing on Tiller Clay . . . . .	92
7.4.1	The Tiller Site . . . . .	92
7.4.2	The Tiller Material . . . . .	93
7.4.3	Consolidation . . . . .	94
7.4.4	Shear Test . . . . .	95
7.5	Testing on Esp Clay . . . . .	95
7.5.1	Consolidation . . . . .	95
7.5.2	Shear Test . . . . .	96
7.6	Testing on Short Sample of Esp Clay . . . . .	96
7.6.1	Consolidation . . . . .	97
<b>8</b>	<b>Summary of Results</b>	<b>99</b>
8.1	Results of Bender Element Testing . . . . .	99
8.2	Empirical determination of $G_{max}$ . . . . .	107

8.3	Results of Cross-Hole Testing . . . . .	108
<b>9</b>	<b>Discussion of Cross-Hole Test Results</b>	<b>111</b>
9.1	Sources of Error . . . . .	111
9.1.1	Response of Accelerometers . . . . .	111
9.1.2	Determination of S-Wave Travel Time and Distance	112
9.1.3	Wave Propagation . . . . .	113
9.2	Determination of S-Wave Travel Time . . . . .	113
9.2.1	Corresponding Points . . . . .	114
9.2.2	Change in Polarity of the S-Wave . . . . .	116
9.3	Assessment of Shear Wave Velocities . . . . .	118
9.3.1	Consistency of Measured $v_s$ Values . . . . .	118
9.3.2	Comparison to Previous Results . . . . .	118
9.3.3	Response shown in a Distance-Time Diagram . . . .	119
<b>10</b>	<b>Discussion of Laboratory Test Results</b>	<b>123</b>
10.1	Sources of Error . . . . .	124
10.1.1	Expelled Pore Water . . . . .	124
10.1.2	Performance of the Test . . . . .	125
10.1.3	Disturbance from Bender Elements . . . . .	127
10.1.4	Wave Propagation in the Triaxial Apparatus . . . .	127
10.1.5	Near-Field Component . . . . .	128
10.2	Assessment of Measured $G_{max}$ . . . . .	128
10.2.1	Comparison to Results of Previous Studies . . . . .	129
10.2.2	Comparison to Field Measured $G_{max}$ of the Esp Clay	132
10.2.3	Comparison to $G_{sec}$ from Shear Test . . . . .	134
10.2.4	Comparison to Empirical $G_{max}$ . . . . .	139
10.3	Effect of Consolidation Time on $G_{max}$ . . . . .	140
10.3.1	Representation of In Situ State . . . . .	144
10.4	Test on Sample of Half Height . . . . .	145
10.4.1	Determination of S-Wave Arrival . . . . .	145
10.4.2	Near-Field Component . . . . .	147
10.4.3	Comparison of $v_s$ of Half- and Full-Height Samples .	147
10.4.4	Development in $v_s$ with Time of Consolidation . . .	148

<b>11 Observations and Further Work</b>	<b>149</b>
11.1 Summary of Test Observations . . . . .	149
11.2 Further Work . . . . .	150
<b>A Task Description</b>	<b>171</b>
<b>B LabView Block Diagram</b>	<b>173</b>
<b>C Index Testing on the Esp Clay</b>	<b>175</b>
<b>D Empirical Determination of <math>G_{max}</math></b>	<b>181</b>
D.1 Stjørdal Clay . . . . .	182
D.1.1 First Test . . . . .	182
D.1.2 Second Test . . . . .	183
D.2 Tiller Clay . . . . .	184
D.3 Esp Clay . . . . .	185
<b>E Results of Cross-Hole Testing at Esp, Byneset</b>	<b>187</b>
E.1 Cross-Hole Test 1 . . . . .	188
E.2 Cross-Hole Test 2 . . . . .	192
E.3 Cross-Hole Test 3 . . . . .	195
E.4 Cross-Hole Test 4 . . . . .	198
E.5 Cross-Hole Test 5 . . . . .	201
E.6 Cross-Hole Test 6 . . . . .	204
E.7 Cross-Hole Test 7 . . . . .	207
E.8 Cross-Hole Test 8 . . . . .	210
<b>F Results of Shear Tests</b>	<b>213</b>
<b>G Variation in <math>v_s</math> with Time of Consolidation</b>	<b>219</b>
G.1 Observations from Bender Element Tests . . . . .	219
G.2 Observations from Previous Study . . . . .	224
<b>H Signals of Opposite Polarity for Identification of the S-Wave</b>	<b>227</b>





# Chapter 1

## Introduction

This chapter gives a description of the background for this study. The task description and objectives are presented. The approach is discussed briefly, before the structure of the report is presented.

### 1.1 Background

Geological materials can not be idealized as assemblages of individual masses and sources of stiffness in the same way as most structures. Due to its continuous nature, soil properties vary smoothly within the material. Dynamic loading and subsequent response must be described in the context of wave propagation. The properties governing the behavior of soil subjected to dynamic loading are called *dynamic soil properties* (Kramer, 1996).

Many problems related to dynamic loading, such as earthquakes and vibrations from traffic, are dominated by wave propagation effects where only low levels of strain are induced in the soil. Stiffness and damping are the most important soil properties influencing such small-strain phenomena. Small strains, typically shear strains below 0.001%, do not cause

significant nonlinear stress-strain behavior in the soil. Consequently, an equivalent linear model can be assumed. The important stiffness parameter at this strain level is the maximum, or small-strain, shear modulus,  $G_{max}$  (Kramer, 1996).

In addition to being an essential parameter in geodynamic problems,  $G_{max}$  is an important parameter for advanced soil modelling. By considering  $G_{max}$  in the analysis, the stiffness at small strains are included. This accounts for the effect of increasing stiffness with distance from the load, as a consequence of damping.

$G_{max}$  can be determined from both laboratory and in situ tests. Due to its simplicity, the use of bender elements has become a common laboratory procedure for measurement of  $G_{max}$ . Also, empirical relationships have been proposed on the basis of test data.  $G_{max}$  is influenced by several factors, which complicates the assessment and interpretation of test results. Due to sample disturbance, values measured in the laboratory may be lower than in the field. The use of  $G_{max}$  as a measure of sample quality has previously been investigated.

This topic has previously been treated at the Geotechnical Division at NTNU, but has not been studied for several years. The work of this Master's Thesis addresses the topic once again, and facilitates further work.

## 1.2 Task Description

The task description is given in Appendix A.

Laboratory testing shall be performed, using bender elements in a triaxial apparatus for determination of  $G_{max}$ . As a supplement, a limited field testing program is suggested.

The task requires a literature study regarding parameters influencing  $G_{max}$ , and assessment of test results and sample disturbance.

### 1.2.1 Objectives

The main objectives of this study are:

- Evaluation of bender element testing.
- Investigation of development of  $G_{max}$  with time.
- Presentation of literature regarding determination of  $G_{max}$  and interpretation of results, with an emphasis on bender elements.

## 1.3 Approach

The initial part of this study was performed in the Autumn of 2013, concerning implementation of bender elements in a triaxial apparatus and some pilot testing.

For the continuation of the work, the first part of the spring semester 2014 was mainly dedicated to a literature survey to acquire essential knowledge regarding the topic. A lot is reported, and getting hold of that of proper relevance was perceived to be a challenge. Further, laboratory work using bender elements for determination of  $G_{max}$  was emphasized. A limited field testing program was developed, resulting in the performance of a cross-hole test. Interpretation of results turned out to be quite time consuming, however literature provided a good basis for assessment. Values measured in the field were valuable for comparison of values measured in the laboratory.

Literature has been obtained from the NTNU University Library and by searching the internet, mainly using google scholar, the databases of the NTNU University Library and the search engine at the websites of the Norwegian Geotechnical Institute (NGI). Lists of references of relevant publications have been searched to provide supplementary information regarding the topic of interest.

## 1.4 Structure of the Report

The thesis consists of eleven chapters.

- Chapter 2 presents theory regarding the behavior of cyclically loaded soils and wave propagation.
- Chapter 3 presents laboratory and field tests for determination of  $G_{max}$ . Of the laboratory tests, the bender element test is emphasized. Factors influencing  $G_{max}$  is also presented here.
- Chapter 4 presents the topic of  $G_{max}(v_s)$  as a measure of sample disturbance.
- Chapter 5 presents the work done prior to the bender element testing, regarding installation of bender elements in a triaxial apparatus.
- Chapter 6 describes the setup and procedure of the cross-hole test performed during this study. A presentation of the site and material is also given.
- Chapter 7 describes the procedure of the bender element tests which are performed during this study. Presentations of the sites and the material of the samples are also given.
- Chapter 8 presents  $G_{max}$  values determined by laboratory and field testing, summarized in tables.
- Chapter 9 gives a discussion of the cross-hole test. Challenges regarding performance and interpretation of results are presented.
- Chapter 10 gives a discussion of the bender element tests. Challenges regarding performance and interpretation, and assessment of the results are presented. Observations of the development of  $G_{max}$  with time of consolidation is also presented here.
- Chapter 11 summarizes observations and assessments of the tests, and gives proposals for further work.

# Chapter 2

## Theory

This chapter presents theory, mainly regarding the behavior of cyclically loaded soils and wave propagation. This is meant to give some understanding regarding soil dynamics, as a basis for the topic treated in the thesis.

Kramer (1996) is used as main reference.

### 2.1 Stress-Strain Behavior of Cyclically Loaded Soils

The mechanical behavior of soil is complex, even under static loading conditions. Dynamic loading makes it even more complex. Nonlinearity in soil leads to an attenuating behavior which influences the stiffness. Presenting dynamic soil behavior in simple models is a constant challenge in geotechnical engineering. Rational models have to balance the conflicting requirements of simplicity and accuracy in a good way (Kramer, 1996).

### 2.1.1 Energy Dissipation and Hysteretic Damping

Soil subjected to symmetric cyclic loading has a non-linear behavior which results in dissipated energy due to hysteresis, illustrated by the stress-strain loop in Figure 2.1. For a wave propagating through soil, this dissipated energy will cause a decrease in the amplitude of the wave as it travels away from the source (Kramer, 1996, Chapter 5). Increasing shear strain amplitude from dynamic loading results in more dissipated energy, and following an increasing damping ratio. As the damping ratio increases, the shear stiffness of the soil decreases, weakening the material (Kramer, 1996). This is illustrated in Figure 2.2.

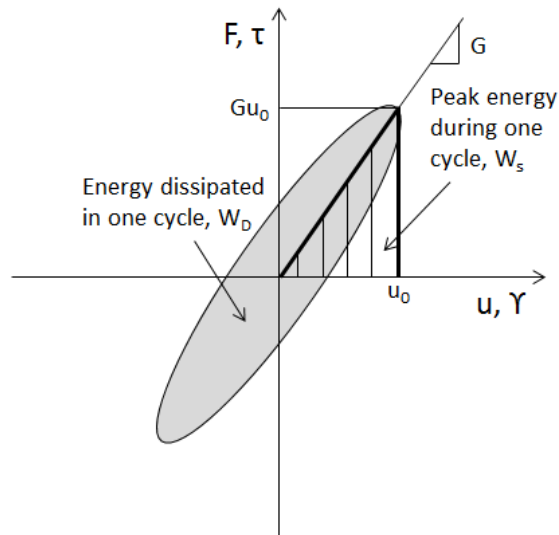


**Figure 2.1:** *Stress-strain loop illustrating energy dissipated through hysteresis. (After Kramer 1996.)*

Due to mathematics, it is convenient to represent the dissipated energy by viscous damping. The use of a Kelvin-Voigt model, schematically illustrated in Figure 2.3, is convenient for expressing the resistance of the material as a sum of an elastic and a viscous part. Here, the elastic part is represented by a spring and the viscous part is represented by a viscous

## 2.1. STRESS-STRAIN BEHAVIOR OF CYCLICALLY LOADED SOILS

dashpot. The stress-strain relationship for an element subjected to shear, described by the Kelvin-Voigt model, is expressed as:

$$\tau = G\gamma + \eta \frac{\partial \gamma}{\partial t} \quad (2.1)$$

The second part introduced in equation (2.1) accounts for strain rate dependency.

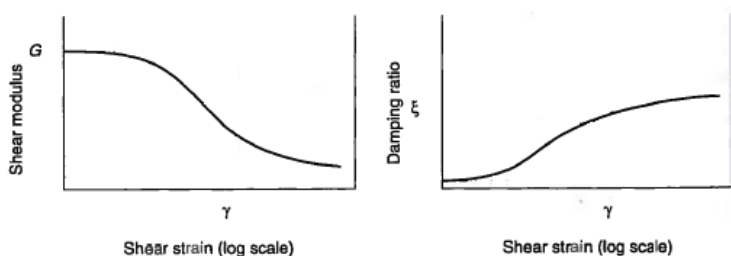


**Figure 2.2:** Variation in shear modulus and damping ratio with shear strain. (After Kramer 1996.)

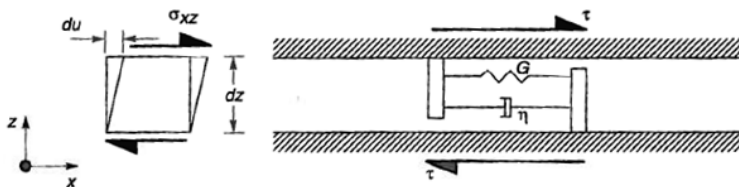


**Figure 2.3:** Kelvin-Voigt element subjected to shearing. Total resistance to shearing deformations is given by the sum of an elastic spring component and a viscous damper component. (From Kramer 1996.)

Dissipated energy is equal to the work conducted when soil is subjected to shear stress, expressed by:

$$W_D = \oint \tau d\gamma \quad (2.2)$$

Given a general equation of motion,  $m\ddot{u} + \eta\dot{u} + Gu = P(t) = p_0 \sin \omega t$ , the work conducted by the elastic force  $f_S = Gu$  is given by:

$$\int Gudu = \int_{t_0}^{t_0+2\pi/\omega} Gu\dot{u}dt = \int_{t_0}^{t_0+2\pi/\omega} G[u_0 \sin(\omega t - \phi)][\omega u_0 \cos(\omega t - \phi)]dt = 0 \quad (2.3)$$

Since the resulting integral consists of factors of sine and cosine, which are 90 degrees out of phase, zero energy will be produced. Equation (2.3) thereby shows that during one cycle, no elastic energy is produced. The same will apply for the internal mass force. The damping force,  $f_D = \eta\dot{u}$ , however, will result in trigonometric factors which are in phase, and thereby produce energy. The work conducted by the damping force is given by:

$$W_D = \int \eta\dot{u}du = \int_{t_0}^{t_0+2\pi/\omega} \eta\dot{u}^2 dt = \eta \int_{t_0}^{t_0+2\pi/\omega} [\omega u_0 \cos(\omega t - \phi)]^2 dt = \pi\eta\omega u_0^2 \quad (2.4)$$

This can be shown graphically by deriving an equation relating the damping force  $f_D$  to the displacement  $u$ . This results in the equation of an ellipse (Chopra, 1995, Chapter 3). The area of this ellipse, shown in Figure 2.4, is  $\pi\eta\omega u_0^2$ .

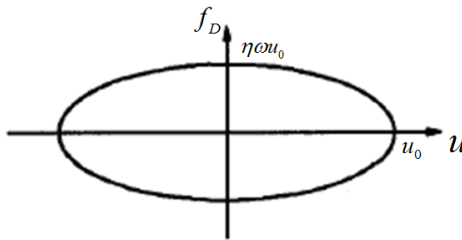


**Figure 2.4:** *Hysteresis loop for a viscous damper. (After Chopra 1995).*



## 2.1. STRESS-STRAIN BEHAVIOR OF CYCLICALLY LOADED SOILS

---

Relating these findings to the hysteresis loop in a stress-strain diagram (Figure 2.1),  $\tau$  is the shear stress resulting from the total resisting force, both elastic and damping. Since the damping force is the only force producing energy, the area of this loop is equal to the area of the ellipse in Figure 2.4, which turns out to be the total energy dissipated in one cycle.

Maximum strain energy dissipating during one cycle is equal to the maximum elastic work, represented by the area shown in Figure 2.1. This is expressed by:

$$W_S = \frac{1}{2}Gu_0^2 \quad (2.5)$$

### 2.1.2 Damping Ratio

Using equation (2.4) and (2.5), the damping ratio can be expressed in terms of energy. Examining the damping capacity,  $W_D/W_S$ , gives

$$\begin{aligned} \frac{W_D}{W_S} &= \frac{\frac{\eta}{\eta_{cr}} 2\sqrt{m}Gu_0^2\omega\pi}{\frac{1}{2}Gu_0^2} \\ \frac{W_D}{W_S} &= \xi 4\sqrt{\frac{m}{G}}\omega\pi \\ \frac{W_D}{W_S} &= \xi 4\frac{\omega}{\omega_n}\pi \end{aligned}$$

Maximum dynamic responses occur at  $\omega = \omega_n$ . Following, the damping ratio can be expressed as:

$$\xi = \frac{W_D}{4\pi W_S} \quad (2.6)$$

### Frequency Independence

Equation (2.4) shows that the dissipated energy is proportional to the frequency of loading, which is not the case for real soils. It is desirable to

express damping and stiffness in soils without the frequency dependence, and still maintain the viscoelastic formulation (Kramer, 1996, Chapter 5).

Inserting expressions for  $W_D$  and  $W_S$  in equation (2.6) gives

$$\xi = \frac{1}{4\pi} \frac{\pi\eta\omega\gamma_0^2}{\frac{1}{2}G\gamma_0^2} = \frac{\eta\omega}{2G} \quad (2.7)$$

An equivalent viscosity, inversely proportional to frequency, is then formulated as

$$\eta = \frac{2G}{\omega}\xi \quad (2.8)$$

The use of this equivalent viscosity ensures that the damping ratio is independent of frequency. The equation of motion for a s-wave propagating through soil can now be expressed in a manner which takes both frequency independence and viscosity into account (Kramer, 1996, Chapter 5).

## 2.2 Wave Propagation

### 2.2.1 Equation of Motion and Frequency Independent Shear Modulus

A vertically propagating s-wave can be represented as many infinitesimal elements of the Kelvin-Voigt model type (Figure 2.3), as illustrated in Figure 2.5. Assuming a cross-sectional area of 1, the change of shear stress with propagation is expressed as:

$$\frac{\partial\tau}{\partial x}dx = \rho dx \frac{\partial^2 u}{\partial t^2} \Rightarrow \frac{\partial\tau}{\partial x} = \rho \frac{\partial^2 u}{\partial t^2} \quad (2.9)$$

The stress-strain relationship for a Kelvin-Voigt model in terms of displacement with wave propagation is given as:

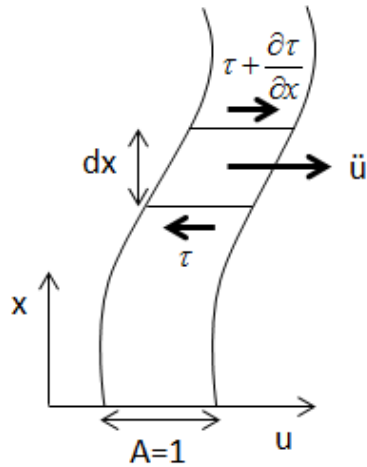


**Figure 2.5:** Propagating wave divided into infinitesimal elements.

$$\tau = G \frac{\partial u}{\partial x} + \eta \frac{\partial^2 u}{\partial x \partial t} \quad (2.10)$$

Differentiation of equation (2.10) with respect to the direction of wave propagation,  $x$ , and insertion into equation (2.9) gives the wave equation:

$$\rho \frac{\partial^2 u}{\partial t^2} = G \frac{\partial^2 u}{\partial x^2} + \eta \frac{\partial^3 u}{\partial x^2 \partial t} \quad (2.11)$$

This is a harmonic wave, and the solution can be written as:

$$u(x, t) = U(x)e^{i\omega t} \quad (2.12)$$

Differentiation gives:

$$\frac{\partial^2 u}{\partial t^2} = -U\omega^2 e^{i\omega t} \quad (2.13)$$

$$\frac{\partial^2 u}{\partial x^2} = \frac{\partial^2 U}{\partial x^2} e^{i\omega t} \quad (2.14)$$

$$\frac{\partial^3 u}{\partial x^2 \partial t} = \frac{\partial^2 U}{\partial x^2} i\omega e^{i\omega t} \quad (2.15)$$

Substitution into the wave equation (2.11) results in the differential equation on the form:

$$(G + i\omega\eta) \frac{d^2 U}{dx^2} = -\rho\omega^2 U \quad (2.16)$$

$G + i\omega\eta$  is called the *complex shear modulus* and denoted as  $G^*$ . Using equation (2.8),  $G^*$  can be expressed by the damping ratio. This results in a shear modulus which accounts for the viscoelastic behavior of soil, expressed by the damping ratio independent of frequency (Kramer, 1996, Chapter 5).

$$G^* = G(1 + 2i\xi) \quad (2.17)$$

Equation (2.17) defines a frequency independent shear modulus.

### Solution to the Equation of Motion

It can be shown mathematically that the solution of the equation of motion can be rewritten as:

$$u(x, t) = Ae^{i(\omega t - k^* x)} + Be^{i(\omega t + k^* x)} \quad (2.18)$$

with  $k^* = \omega \sqrt{\frac{\rho}{G^*}}$  (Kramer, 1996, Chapter 5).

Equation (2.18) describes the displacement at any point of a propagating wave. The term expressed by  $t$  describes how the displacement varies

## 2.2. WAVE PROPAGATION

---

with time at a constant point  $x$  along the wave. The term expressed by  $x$  describes the displacement at any point along the wave when time is held constant. The sign in front of the  $k^*x$ -part determines the direction of wave propagation. Equivalent for equation (2.12),  $U(x) = W_0 e^{\pm ik^*x}$  describes displacement at any position  $x$  when time is held constant, while  $e^{i\omega t}$  describes displacement varying with time at a given position,  $x$ .

### 2.2.2 Seismic Waves

#### Compressional Wave

The compressional wave, also called primary wave (p-wave), has particle displacements parallel to the direction of wave propagation. The wave propagates by compression and expansion of particles. An illustration of the propagation and particle movement of the p-wave is given in Figure 2.6.

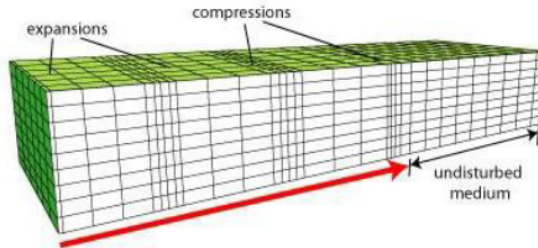


**Figure 2.6:** Illustration of the p-wave, showing direction of propagation and particle movement. (From Eiksund 2013.)

The differential equation of the p-wave is given as (Kramer, 1996, Chapter 5):

$$\frac{\partial^2 \varepsilon_V}{\partial t^2} = \frac{\lambda + 2\mu}{\rho} \nabla^2 \varepsilon_V = v_p^2 \nabla^2 \varepsilon_V \quad (2.19)$$

The wave equation is a function of volumetric strain,  $\varepsilon_V$ , which describes deformations that involve no shearing or rotation. Therefore, the compressional wave is an *irrotational*, or *dilatational*, wave, which means there is no rotation of the material the wave passes through.

$\lambda$  and  $\mu$  are the *Lamé constants*, and for the shear modulus and Poisson's ratio we have the relationships (Kramer, 1996, Chapter 5):

$$G = \mu \tag{2.20}$$

$$\nu = \frac{\lambda}{2(\lambda + \mu)} \tag{2.21}$$

From equation (2.19), we get the velocity at which the p-wave will propagate through a body, as a function of the Lamé constants:

$$v_p = \sqrt{\frac{\lambda + 2\mu}{\rho}} \tag{2.22}$$

Using equations (2.20) and (2.21),  $v_p$  can be written in terms of shear modulus and Poisson's ratio as:

$$v_p = \sqrt{\frac{G(2 - 2\nu)}{\rho(1 - 2\nu)}} \tag{2.23}$$

This is referred to as the *p-wave velocity* of the material (Kramer, 1996, Chapter 5).

### Shear Wave

The shear wave (s-wave) has particle motion constrained to a plane perpendicular to the direction of wave propagation. S-waves may propagate

## 2.2. WAVE PROPAGATION

---

in vertical direction with horizontal particle motion, in horizontal direction with vertical particle motion, or in horizontal direction with horizontal particle motion. These are denoted as VH-waves, HV-waves, and HH-waves, respectively. An illustration of the propagation and particle movement of the s-wave (HV-wave) is given in Figure 2.7.

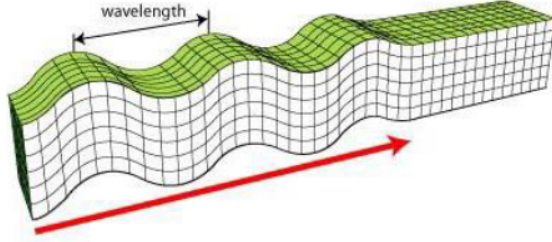


**Figure 2.7:** Illustration of the s-wave (HV-wave), showing direction of propagation and particle movement. (From Eiksund 2013.)

The differential equation of the s-wave is given as (Kramer, 1996, Chapter 5):

$$\frac{\partial^2 \omega_x}{\partial t^2} = \frac{\mu}{\rho} \nabla^2 \omega_x = v_s^2 \nabla^2 \omega_x \quad (2.24)$$

where  $\omega_x$  is rotations around the  $x$ -axis,  $\omega_x = \frac{1}{2}(\frac{dw}{dy} - \frac{dv}{dz})$ . This equation describes an *equivoluminal*, or *distortional* wave, of rotation about the  $x$ -axis. Equivalent expressions exist for rotation about the  $y$ - and  $z$ -axis. S-waves involve no volume change of the material of which they pass through. From equation (2.24) we get the velocity at which the shear wave will propagate through a body:

$$v_s = \sqrt{\frac{\mu}{\rho}} = \sqrt{\frac{G}{\rho}} \quad (2.25)$$

This is referred to as the *shear wave velocity* of the material (Kramer, 1996, Chapter 5).

### Rayleigh Wave

The Rayleigh wave (r-wave) is a surface wave traveling through solids, strongly limited with depth. It is the most important surface wave, of particular interest in earthquake engineering. The r-wave can be described as a combination of p- and s-waves, with particles having a "rolling" (ellipsoidal) movement, where both compression/extension and vertical displacement is present (Kramer, 1996; Nordal, 2013b). An illustration of the propagation and particle movement of the Rayleigh-wave is given in Figure 2.8. The movement of the Rayleigh wave is similar to that of waves on the surface of water.

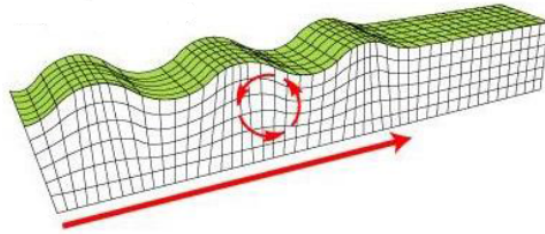


**Figure 2.8:** *Illustration of the Rayleigh-wave, showing direction of propagation and particle movement. (From Eiksund 2013.)*

The velocity at which the Rayleigh wave propagates is approximately equal to the s-wave velocity (Nordal, 2013b).

$$v_R \approx v_s \tag{2.26}$$



### P- and S-wave Relationship

The p- and s-waves are the only waves that can exist in an unbounded elastic solid, and are collectively referred to as *body waves* (Kramer, 1996, Chapter 5). The ratio between the p- and s-wave velocities is:

$$\frac{v_p}{v_s} = \sqrt{\frac{2(1-\nu)}{1-2\nu}} \quad (2.27)$$

This shows that the p-wave velocity is greater than the shear wave velocity with a magnitude dependent on the Poisson's ratio (Kramer, 1996, Chapter 5). This is also illustrated in Figure 2.9. The p-wave is seen to propagate at a velocity significantly higher than that of the s-wave and Rayleigh wave. This may cause difficulties in field and laboratory tests where identification of the s-wave arrival is required for determination of  $v_s$ . This is further discussed later in the thesis.

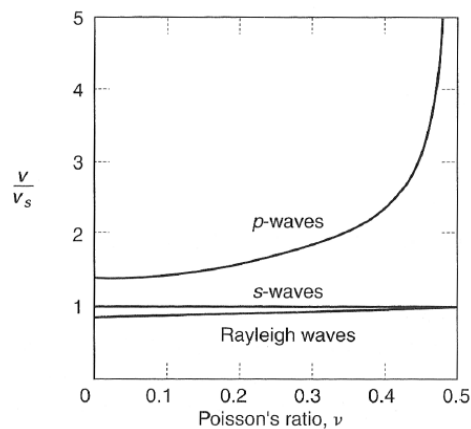


**Figure 2.9:** Variation of propagation velocities of the Rayleigh wave and body waves, as a function of Poisson's ratio. (From Kramer, 1996.)

## 2.3 Equivalent Linear Model

Several models have been proposed to present dynamic soil behavior in a good, yet simple manner. The equivalent linear model is the simplest and most commonly used. At low strain levels, nonlinear stress-strain behavior is not induced in the soil at significant extent. Therefore, linearity of the soil is a reasonable assumption, and an equivalent linear model is a good basis for evaluation of dynamic soil properties (Kramer, 1996, Chapter 6).

Equivalent linear models describe the general shape of the stress-strain loop resulting from hysteresis, shown in Figure 2.10. The shape of the loop is described by its inclination and breadth. The inclination is determined by the shear stiffness of the soil, which can be described by the tangent shear modulus,  $G_{tan}$ . Each point along the path of the loop has a different  $G_{tan}$  value. To describe a general inclination of the hysteresis-loop, an average value of  $G_{tan}$  over the entire loop is used as an approximation. This is called the secant shear modulus, and is defined as:

$$G_{sec} = \frac{\tau_c}{\gamma_c} \quad (2.28)$$

where  $\tau_c$  is the cyclic shear stress and  $\gamma_c$  is the cyclic shear strain amplitude. Note that the viscous term from equation (2.1) is not included for this model.

The breadth of the hysteresis loop is related to the area enclosed by the stress path, which represents the energy dissipated during one cycle.

It is shown in section 2.1.1 that the damping ratio can be expressed in terms of energy by:

$$\xi = \frac{W_D}{4\pi W_S} = \frac{1}{2\pi} \frac{A_{loop}}{G_{sec}\gamma_c^2} \quad (2.29)$$

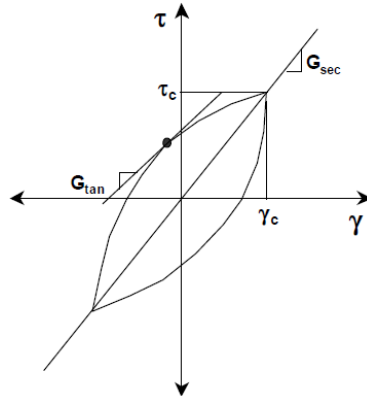


**Figure 2.10:** *Hysteresis loop showing secant shear modulus,  $G_{sec}$ , and tangent shear modulus,  $G_{tan}$ . (From Kramer 1996.)*

where  $W_D$  is the dissipated energy during one cycle,  $W_S$  is the maximum strain energy, and  $A_{loop}$  is the area of the entire hysteresis loop.

The parameters  $G_{sec}$  and  $\xi$  are often referred to as *equivalent linear* material parameters. In more complex models, a description of the actual path of the hysteresis loop is needed to describe the soil behavior. However, for equivalent linear models, where linearity and small strains is assumed, the parameters can be used directly in analysis. Because ground response analysis based on this type of models is commonly used, characterization of  $G_{max}$  and  $\xi$  are given considerable attention.

It is important to note that the assumption of linearity makes the equivalent linear model useless in situations with permanent deformation or failure. It is implied in the model that all strains are zero after cyclic loading. In addition, a linear material does not have a limiting strength, which means it cannot reach failure. The equivalent linear model is only an approximation of the non-linear behavior of soil, discussed in section 2.1.1 (Kramer, 1996, Chapter 6).

For convenience and consistency with commonly used notation, the secant shear modulus will hereafter be denoted  $G$ , without the “sec” subscript.

### 2.3.1 Shear Modulus

The secant shear modulus varies with cyclic strain amplitude. Increasing cyclic strain amplitude gives decreasing  $G$ . This is illustrated by plotting the points corresponding to the tips of the hysteresis loop for different cyclic strain amplitudes. The resulting curve is called a backbone curve, presented in Figure 2.11(a). The inclination of the curve at zero cyclic strain amplitude is the maximum value of the shear modulus,  $G_{max}$ . This stiffness parameter is applicable at strains below approximately 0.001 %.

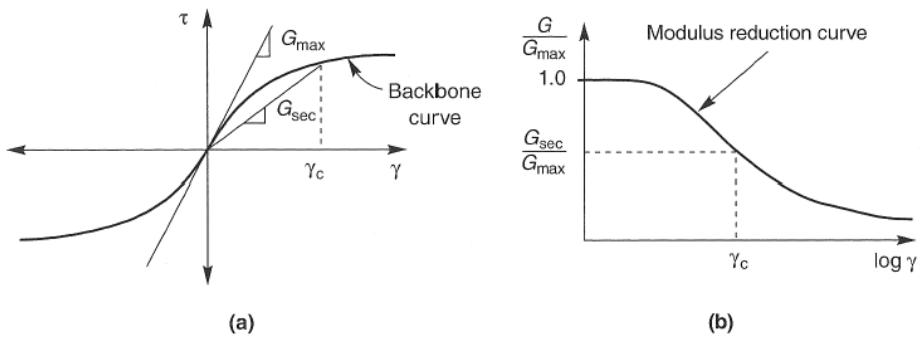


**Figure 2.11:** Backbone curve and modulus reduction curve showing typical variation of  $G_{sec}$  with shear strain. (From Kramer 1996.)

Often, the variation in shear modulus with cyclic strain amplitude is represented by the modulus ratio  $G/G_{max}$ . This gives the modulus reduction curve, presented in Figure 2.11(b). The modulus reduction curve represents the same information as the backbone curve, only in a different manner. Figure 2.11(b) clearly shows that for cyclic strain amplitudes larger than zero, the shear modulus ratio is less than one.

Because of its variation with cyclic strain amplitude, consideration of both the ratio  $G/G_{max}$  and  $G_{max}$  is important when defining the stiffness of a material (Kramer, 1996, Chapter 6).

## Chapter 3

# Small-Strain Shear Modulus

A common way of determining the small-strain shear modulus,  $G_{max}$ , is to measure the shear wave velocity,  $v_s$ , and compute  $G_{max}$  as:

$$G_{max} = \rho v_s^2 \quad (3.1)$$

This approach can be applied for both laboratory and field tests. It is taken to be the most reliable way of determining  $G_{max}$ , but care must be taken in the interpretation of results. Several factors are seen to influence  $G_{max}$ . Also, identification of the s-wave may be difficult due to complex environments consisting of disturbances and different types of waves (Kramer, 1996).

Empirical relationships between  $G_{max}$  and influencing parameters have also been developed.

This chapter will present laboratory and field tests for determination of  $G_{max}$ . Of the laboratory test, the bender element test is emphasized. Section 3.3 deals with the influence of different factors on  $G_{max}$ , on the basis of previously performed studies.

## 3.1 Laboratory Tests

Laboratory tests are performed on soil samples assumed to be representative for the area of interest. Test apparatuses seek to recreate the in situ condition of the sample. Different tests provide different types of stress-strain conditions, and whatever is most suitable must be chosen for each problem (Kramer, 1996).

Normally, properties of existing soil in field are required, which further requires testing on undisturbed samples. It is however, impossible to avoid every aspect of disturbance. Some measure of sample quality is important for assessment of the reliability of test results (Kramer, 1996).

For determination of small strain properties of soil, there are not many alternatives of laboratory tests. Those commonly used, are presented here. The bender element test is emphasized, since this has been performed during this study. The torsional simple shear test is briefly mentioned, although it is a high-strain test, because it is mentioned in literature discussed later in the chapter.

### 3.1.1 Resonant Column Test

The resonant column test is a commonly used laboratory test for measurement of dynamic properties of soils at small and medium strain. The soil sample is placed and consolidated in a cell where it is fixed at the bottom and free at the top. The top is subjected to torsional or axial loading, normally harmonic with a controlled frequency and amplitude. The cyclic loading is initially set at a low frequency, which is further increased until maximum response occurs. The lowest frequency at which maximum strain amplitude is reached, is the first-mode resonance frequency of the sample (Kramer, 1996; EPRI, 1993). Figure 3.1 shows a typical resonant column apparatus (b), with a top view giving a simple illustration of the loading system (a).

### 3.1. LABORATORY TESTS

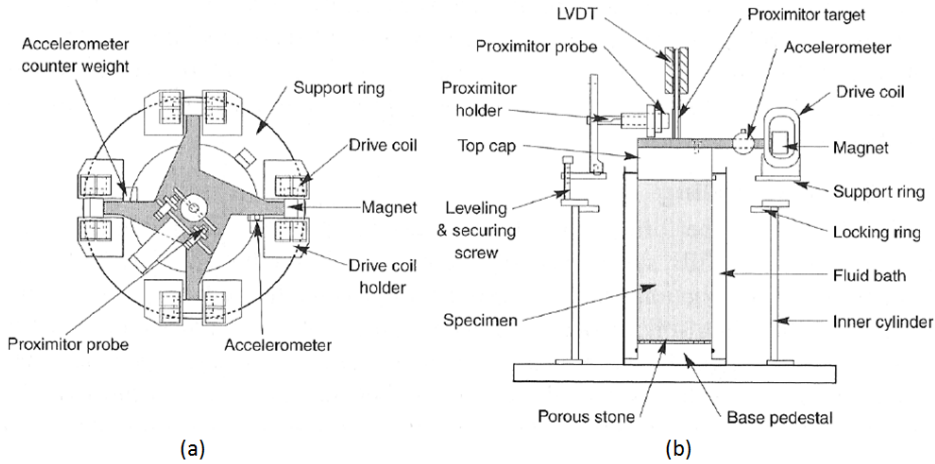


**Figure 3.1:** Typical resonant column test apparatus. (a) Top view (b) Profile view of system and sample. (From Kramer 1996.)

Details on how the resonance frequency,  $f_n$ , can be related to the shear modulus, is described by Kramer (1996, p.217). In short, the solution of the equation of motion for a column-mass system is used, and the mass polar moment of inertia of the sample,  $I$ , and of the loading system,  $I_0$ , is required. It can be shown that:

$$\frac{I}{I_0} = \frac{\omega_n h}{v_s} \tan \frac{\omega_n h}{v_s} \quad (3.2)$$

where  $h$  is the height of the sample, and  $\omega_n$  is the angular frequency of the  $n$ th mode. From equation (3.2),  $v_s$  can be calculated, and  $G_{max}$  can be determined from equation (3.1).

Material damping may also be determined from the resonant column test (Kramer, 1996; EPRI, 1993). This requires somewhat more thorough analysis, which will not be further explored here.

### 3.1.2 Bender Element Test

A common way of determining the shear wave velocity, and from this obtain the small-strain stiffness,  $G_{max}$ , is to use bender elements in conventional laboratory test devices. Bender elements consists of two thin plates of piezoelectric material bonded together, with two conductive outer layers and a metal shim at the center, as illustrated in Figure 3.2(a) (Lee and Santamarina, 2005). Two such elements are placed opposite one another in the soil sample, one acting as a transmitter and the other as a receiver element. A voltage pulse is applied to the transmitter element, causing one of the plates to contract while the other expands so that the element bends as shown in Figure 3.3. This produces a s-wave which travels through the sample. When the s-wave reaches the receiver element, this element will distort and cause another voltage pulse. The time difference between the two voltage pulses is measured. Since the lengths of the soil sample and the bender elements are known, the s-wave velocity can be determined by dividing the wave travel distance with the travel time. The travel distance of the s-wave is taken as the distance between the tips of the bender elements.  $G_{max}$ , can now be obtained using equation (3.1) (Kramer, 1996; Ibrahim et al., 2011).

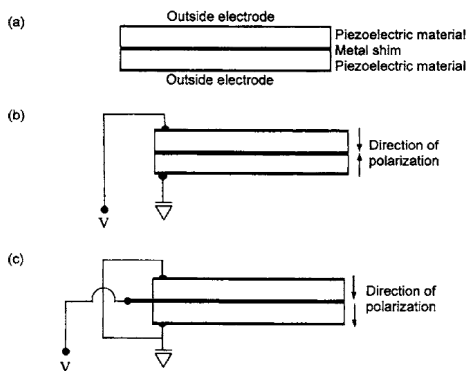


**Figure 3.2:** Schematic illustration of bender elements: (a) general, (b) series type, and (c) parallel type. (From Lee and Santamarina 2005.)



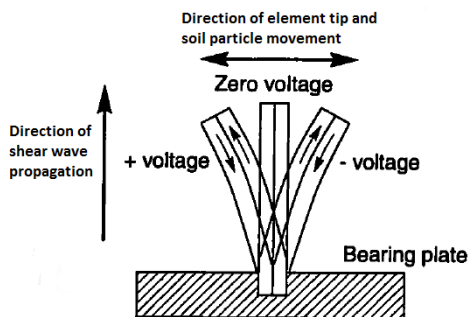


**Figure 3.3:** Piezoelectric bender element. Positive voltage causes element to bend one way, negative voltage causes it to bend the other. (From Kramer, 1996.)

Bender elements generate both p-waves and s-waves, which can cause difficulties when interpreting the arrival of the shear wave. Two p-waves are generated at the sides of the bender element, one in compression and one in rarefaction, and a s-wave is generated at the front, as shown in Figure 3.4 (Lee and Santamarina, 2005).

There are both series and parallel type bender elements. The series type have poling directions of the piezoelectric plates opposite to each other, and both the core and the ground cable is connected at the outer electrodes, as shown in Figure 3.2(b). In the parallel type, the poling direction is the same for the two piezoelectric plates. The ground cable is connected

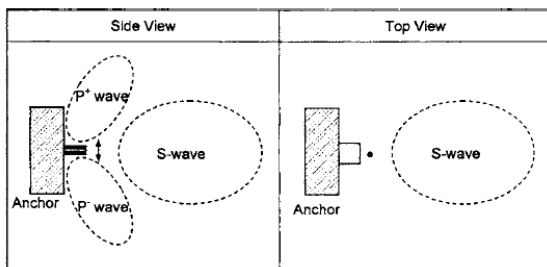


**Figure 3.4:** Waves generated by bender elements, transverse and in-plane direction. (From Lee and Santamarina 2005.)

to both outer electrodes, while the core cable is connected to the metal shim lying at the center, as shown in Figure 3.2(c). It is often recommended to use the parallel type bender elements as transmitter and the series type as receiver. This is because the same applied voltage produces twice the displacement for the parallel type connection as for the series type (Lee and Santamarina, 2005).

### Advantages and Recommendations

The use of bender elements has some clear advantages. It does not disturb the soil sample, which means that several repetitive tests can be performed, and the sample can be subsequently tested for other soil characteristics (Youn et al., 2008; Kramer, 1996). Another advantage is that it can be set up in most laboratory apparatuses, thus facilitating comparison with other results (Youn et al., 2008). The greatest difficulty comprising the determination and reliability of  $G_{max}$  obtained from bender element measurements, is the determination of shear wave arrival time,  $t_s$  (Ibrahim et al., 2011). The arrival of the s-wave may be misinterpreted with the p-wave arrival. In addition, the recorded output signal may contain ambient noise which makes it difficult to read the exact arrival time. Due to this, it is important that interpretation of  $t_s$  is done with caution (Ibrahim et al., 2011).

Some recommendations governing the bender element test, especially associated with the arrival time determination, has been proposed (Wang et al., 2007). The receiver element should be placed at a distance at least two wavelengths away from the source, giving  $\frac{L_{tt}}{\lambda} \geq 2$ . For this case, near field effects are expected not to prevail. The  $\frac{L_{tt}}{\lambda}$ -ratio can be increased by increasing the frequency of the voltage applied to the transmitter element. An amplifier should be used both for the transmitted and received signal. The transfer function of the receiver system,  $H_{be-R}$ , can cause time delay which can be corrected after identification and consideration of the time delay of each corresponding point induced by  $H_{be-R}$  (Wang

### 3.1. LABORATORY TESTS

et al., 2007). A sinusoidal wave is usually preferred as an input signal rather than a square wave, since its received signal shows more resemblance to the original transmitted signal and has less distortion (Ibrahim et al., 2011). Transmitting two signals, one after reversing poles of the voltage, can ensure that the received signals are produced by shear waves (Hu et al., 2010). This will cause a shift in the deflection of the registered s-wave, while p-wave signals will be unchanged, as shown in Figure 3.14(Butcher et al., 2005).

#### 3.1.3 Torsional Simple Shear Test

The torsional simple shear test is performed on hollow cylindrical samples. The sample is placed in a cell and consolidated to desired isotropic or anisotropic stress state. A torque is applied for continuous shearing of the sample (Pradhan et al., 1988).

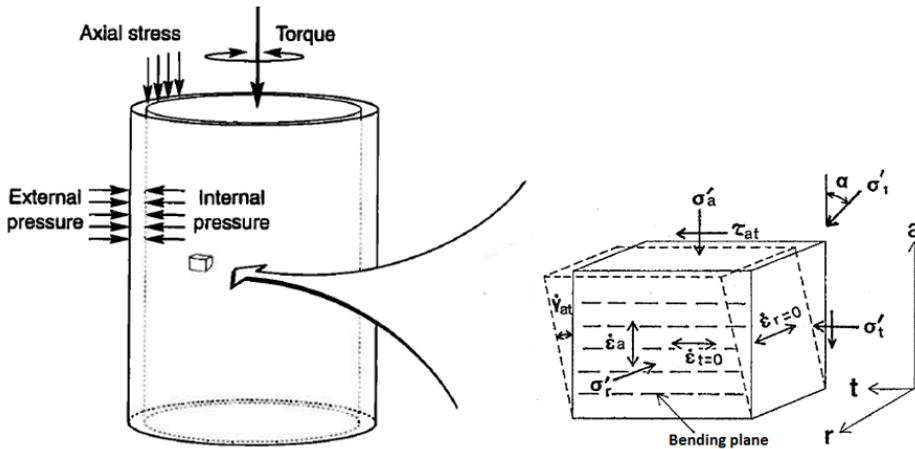


**Figure 3.5:** *Simplified illustration of the torsional simple test. A small element shows the conditions required for simple shear deformation. (From Kramer 1996; Pradhan et al. 1988.)*

The simple shear situation requires parallel movement of all parallel planes

in the direction of shear, without any change in original shapes. All horizontal normal strains are kept zero. To obtain this condition, the sample is subjected to both an outer ( $p'_o$ ) and inner ( $p'_i$ ) pressure, which can be controlled independently, and  $p'_o \neq p'_i$ . The volume change is controlled by measuring the amount of water expelled from or soaked into the inner cylinder. Axial pressure is applied in terms of air pressure, independent of  $p'_o$  and  $p'_i$ . All pressures are automatically controlled by a computer, to ensure the intended stress-strain condition (Pradhan et al., 1988).

## 3.2 Field Tests

With field tests, soil properties can be measured in situ, where the effects of existing stress, chemical, thermal and structural conditions are present. A compelling advantage of performing field investigations is that there is no need for sampling, thus sample disturbance is not an issue. Also, the risk of basing evaluation upon small, unrepresentative samples is avoided, as measurements are performed on a larger volume of soil. However, effects of the in situ conditions are the only ones that can be investigated, and pore water drainage can not be controlled (Kramer, 1996).

Field tests can be performed both from the ground surface, in boreholes or by probes driven into the soil. Surface tests are useful where drilling and sampling are difficult to conduct. Often, they are relatively cheap, and can be performed quickly. Borehole tests are more expensive, but the interpretation is usually more direct, and information as visual soil characteristics and water table location can be gained directly from the boring (Kramer, 1996). Advantages and disadvantages of different field testing methods are given in Table 3.1.

Since this study deals with small-strain properties ( $\gamma < 0.001\%$ ), particularly the small-strain shear modulus, high-strain tests will not be discussed. Small-strain field tests will however, be presented in the following.

## 3.2. FIELD TESTS

---

**Table 3.1:** *Assessment of field testing methods. (From Frost and Burns 2003)*

Method	Advantages	Disadvantages
Downhole	Only one borehole required Relatively inexpensive Measurement of seismic soil properties	Attenuation with depth Invasive No sample recovered Limited by depth of borehole
Crosshole	Minimum of two boreholes required No attenuation with depth Measurement of seismic soil properties	Expensive Invasive Possible refraction interference No sample recovered Limited by depth of borehole Complex data analysis Special equipment and skilled operators required
Surface	Noninvasive Inexpensive Measurement of seismic soil properties No boreholes required Environmental applications due to limited contamination exposure	No sample recovered Attenuation with depth Refraction method applicable only when velocities increase with depth Possible refraction interference

### 3.2.1 Seismic Reflection Test

The seismic reflection test is a surface test with the simplest configuration consisting of one source and one receiver. More receivers can possibly be used. The test is rarely used for investigations of shallow soil layers, but rather used for determination of wave propagation velocity and layer thickness at large-scale and/or very deep stratigraphy (Kramer, 1996). An illustration of the test setup is shown in Figure 3.6.

The impulse produced by the source is usually rich in p-waves. Waves radiate away from the source in all directions with a hemispherical wave-front. With the distance from the source to the receiver known, measuring the wave travel time will give the p-wave velocity at the surface layer,  $v_p$ .

The travel distance of a p-wave traveling down into the surface and being reflected by a horizontal layer boundary is twice the distance given in Figure 3.6, i.e.  $\sqrt{4H^2 + x^2}$ . With this travel distance and the p-wave velocity from surface calculations known, the thickness of the upper layer,  $H$ , can be determined. The travel time,  $t_r$ , of the wave is measured, and then the relation  $v_p t_r = \sqrt{4H^2 + x^2}$  gives:

$$H = \frac{1}{2} \sqrt{t_r^2 v_p^2 - x^2} \quad (3.3)$$

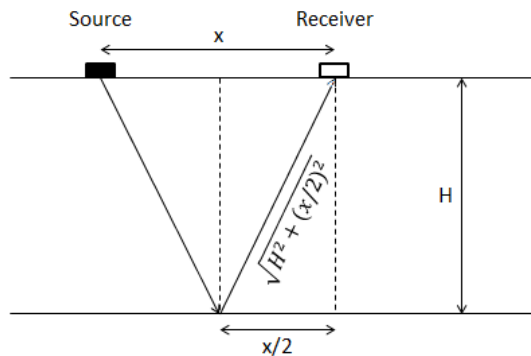


**Figure 3.6:** *Simplified illustration of the seismic reflection test, showing the path of a p-wave reflected from a horizontal layer boundary.*

The arrival time of the reflected wave differs from the arrival time of the direct wave which travels along the surface. This difference decreases with increasing source-receiver distance. The assumption of horizontal layering is often not valid for real cases. Then, several measurements must be done. The inclination of inclined boundaries can be determined from travel-time measurements (Kramer, 1996).

### 3.2.2 Seismic Refraction Test

The seismic refraction test provides for the determination of elastic wave velocities of a layered soil profile. Wave velocities and the thickness of each

### 3.2. FIELD TESTS

---

layer can be determined, as long as the wave velocities increase with each successively deeper layer (Luna and Jadi, 2000). The configuration consists of an explosive or mechanical impulsive source and several receivers. Both p- and s-waves can be transmitted by the source. The arrival time of the first wave reaching each receiver is measured regardless of path, and the distance and travel time measured from one receiver to the next is used for determination of wave velocity. The measured arrival times can be plotted against source-receiver distance, giving a curve as shown in Figure 3.7. The non-linearity of the curve reveals a complex mechanism, where a single wave traveling with constant velocity is not the case (Kramer, 1996).

P-waves travel faster than s-waves, and will hence arrive first at a receiver. The p-wave velocity is used for determination of the elastic modulus,  $E$ . However, in most dynamic soil problems, the shear modulus is the most important parameter. In this case, a source rich of shearing energy that is able to propagate over long distances must be used for direct measurement of the s-wave velocities (Luna and Jadi, 2000).

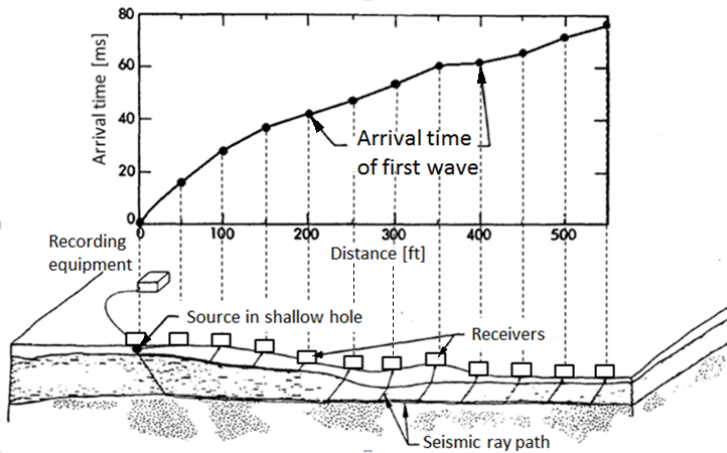


**Figure 3.7:** *Illustration of the seismic refraction test. (After Redpath 1973.)*

### Determination of Soil Layer Thickness

For soil layers with horizontal boundaries, relatively simple calculations can be done for determination of layer thickness. Stress waves traveling directly from the source to a receiver is called a *direct wave*. Some energy rays travel downward towards layer boundaries, where they are reflected and refracted. At some point, refraction at the layer boundary will cause a *head wave*, traveling through the overlying layer towards the surface. At short source-receiver distances, the direct wave will produce the first arrival, while at larger distances, the head wave will arrive before the direct wave. The point where this shift happens is called the *critical distance*,  $x_c$ . From the arrival time-distance diagram, the velocity of each layer is determined as the inclination of each line segment. With the velocities and critical distance known, the thickness of the  $k$ th layer can be determined by equation (3.4), valid for  $k \geq 2$  (Corps of Engineers, 1995).

$$H_k = \frac{x_{ck}}{2} \sqrt{\frac{v_{k+1}-v_k}{v_{k+1}+v_k}} + \sum_{j=1}^{k-1} \frac{H_j}{v_j} \frac{v_{k+1} \sqrt{v_k^2 - v_j^2} - v_k \sqrt{v_{k+1}^2 - v_j^2}}{\sqrt{v_{k+1}^2 - v_k^2}} \quad (3.4)$$

### Inclined or Irregular Layering

For inclined or irregular layering, the wave velocities are influenced by the slope of the layer boundaries and their critical angles. In this case, the velocities can not be found directly from the arrival time-distance diagram. The velocity measured by a refraction test in the down-dip direction of an inclined boundary is lower than that measured in the up-dip direction. Reversed profiling is therefore routinely performed to reveal inclined layering. The true velocity is a function of the two apparent velocities and the dip angle. A more thorough interpretation is required for determination of velocities and layer thickness (Kramer, 1996).



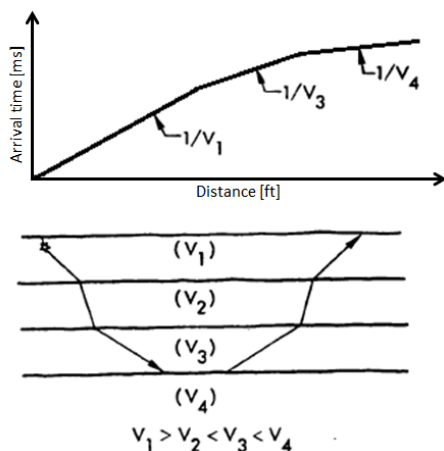


**Figure 3.8:** Schematic description of velocity reversal, a limitation of the seismic refraction test. (From Redpath 1973.)

### Advantages and Limitations

The use of first wave arrival times, regardless to path, makes the refraction test superior to the reflection test, with interpretation being more straightforward (Kramer, 1996; Frost and Burns, 2003). Limitations of the refraction method includes the *blind zone* phenomenon. This refers to the possible existence of certain soil layers not discovered by the refraction seismograph due to insufficient thickness or velocity contrast. This will cause the computed depth of a deeper layer to be less than the actual depth. (Redpath, 1973). *Velocity reversal* is another functional problem that can occur when a low-velocity layer lies below a high-velocity layer. The seismic ray will then be refracted downwards towards the vertical (Figure 3.8), and will not be detected at the surface, hence the low-velocity layer will not appear as an individual segment on the arrival time-distance curve. This can result in erroneous computations of depths to underlying beds (Redpath, 1973; Luna and Jadi, 2000; Kramer, 1996).

### 3.2.3 Steady-State Vibration (Rayleigh Wave) Test

Jones (1958) introduced the steady state Rayleigh wave - continuous surface wave (CSW) technique into the field of geotechnical engineering. He performed experiments, exposing the surface to vibrations of a particular frequency, and measuring the phase velocity of the surface waves. The object was to develop an in situ testing method for derivation of the dynamic shear elasticity of soil and provide an estimate of its strength, without any special preparation of the surface being necessary. Jones (1958) presented a method for determination of the dynamic shear modulus of the soil from the resonant frequency of a mass vibrating perpendicular to the surface. The results indicated that the uncertainty in the shear modulus, due to an unknown stress distribution beneath the vibrator, was likely to be about  $\pm 11\%$  (Jones, 1958).

The steady-state vibration test interpret the characteristics of surface displacements caused by Rayleigh waves, primarily, transmitted from a vertically vibrating footing. One receiver is placed at the footing, and several others at different distances away from the footing for localization of points vibrating in-phase. The distance between adjacent points vibrating in-phase is equal to the wavelength of the Rayleigh wave,  $\lambda_R$ . Figure 3.9 shows a schematic illustration of the test setup, with exaggerated surface movement. Further, the Rayleigh wave phase velocity,  $v_R$ , can be determined using equation (3.5) (Kramer, 1996).

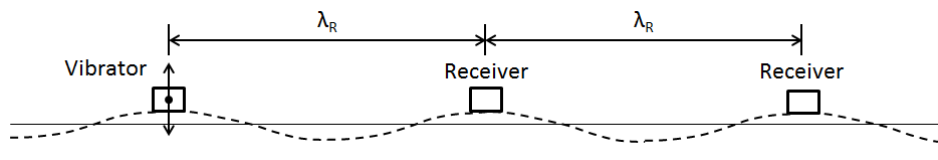


**Figure 3.9:** Simplified illustration of a typical setup of the steady-state vibration test. (After Kramer 1996.)

$$v_R = \frac{\omega \lambda_R}{2\pi} = f \lambda_R \quad (3.5)$$

At small strains, the s-wave velocity is nearly the same as the Rayleigh wave velocity (Luna and Jadi, 2000). According to Kramer (1996),  $v_s \approx 1.09v_R$  is an approximation valid for many soils. Velocity variation with depth can be estimated by varying the frequency of the source (Kramer, 1996; Luna and Jadi, 2000).

### Advantages and Limitations

With the characteristics of steady-state vibrations as a basis for interpretation, the problem of detecting wave arrivals and measuring arrival times is eliminated. However, application of the steady-state vibration test is mainly limited to determination of near-surface s-wave velocities (Kramer, 1996). For exploration of deep soil profiles, large force-generation equipment that can operate at low frequencies are required (Luna and Jadi, 2000). Also, when stiffness vary with depth, dispersion will occur, giving a frequency dependence of the Rayleigh wave phase velocity. Due to the limitations of the steady-state vibration test, other tests, such as the spectral analysis of surface waves (Section 3.2.4), are more commonly used (Kramer, 1996).

#### 3.2.4 Spectral Analysis of Surface Waves Test

Dispersion is the phenomenon in which the phase velocity of a wave depends on its wavelength, or frequency. Rayleigh waves, which are the most widely used surface waves in geotechnical engineering, are dispersive. Rayleigh waves with long wavelength, or low frequency, will have a deeper range than Rayleigh waves with shorter wavelength, or high frequency. Hence, high-frequency waves will reflect properties of material closer to the surface than low-frequency waves, which will be influenced by deeper material (Long et al., 2008).

With Spectral Analysis of Surface Waves (SASW), a wide range of frequencies is generated from an impulsive or random noise load. Two vertical

receivers are placed on the surface at distance  $d_1$  and  $d_2$  from the source, as illustrated in Figure 3.10. The source can for example be a sledge hammer. The phase difference and corresponding travel time between receivers can be calculated, and with the distance between receivers being known, the Rayleigh wave phase velocity is also known (Kramer, 1996). Dispersion is then used to produce velocity and frequency correlations called dispersion curves. By inversion, profiles giving s-wave velocity variations with depth can also be generated (Long et al., 2008).

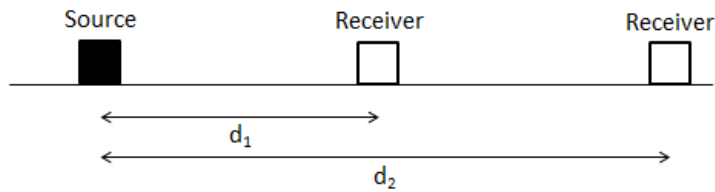


**Figure 3.10:** *Simplified illustration of a typical setup of the SASW test, showing two receivers at distance  $d_1$  and  $d_2$  from the load source. (After Kramer 1996.)*

### Advantages and Limitations

Since the SASW test require no borehole, it is particularly useful at sites where drilling and samplig is difficult. In addition, it allows for detection of low-velocity layers, and can be used to considerable depth ( $>100$  m). However, specialized equipment and experienced operators are needed (Kramer, 1996). The SASW test can be performed relatively quickly, but when several measurements at different source-receiver configuration is needed, it is more time consuming and labour intensive (Long et al., 2008).

### 3.2.5 Multichannel Analysis of Surface Waves Test

The Multichannel Analysis of Surface Waves (MASW) was introduced in the late 1990s by the Kansas Geological Survey (Park et al., 1999).

It is similar to the SASW test. The most significant difference is that it involves several receivers, usually 12 to 60, which makes it less time and labour intensive than the SASW test. An advantage of the MASW approach is its ability to identify and separate fundamental and higher mode surface waves (Long et al., 2008).

To generate s-wave velocity-depth profiles from MASW results, techniques of inversion is required. Xia et al. (1999) presented a method of inverting high-frequency Rayleigh-wave dispersion data to near-surface s-wave velocities. The Rayleigh-wave phase velocity is a function of s-wave velocity, p-wave velocity, density, and layer thickness. Each parameter contributes to the dispersion curve in an unique way, and together they define a layered earth model. S-wave velocity is the dominant property for the fundamental mode of high frequencies ( $\geq 5$  Hz), hence the dominant influence on a dispersion curve. The inversion method presented by Xia et al. (1999) is an iterative method, using a least-squares technique. An initial earth model is chosen, and a synthetic dispersion curve is generated. It is found reasonable to assign p-wave velocities and densities as known constants with a relative error of 25 % or less. The s-wave velocity is updated after each iteration until the synthetic dispersion matches the field curve (Xia et al., 1999).

#### 3.2.6 Seismic Cross-Hole Test

The seismic cross-hole test is performed in boreholes. The simplest setup uses two boreholes, with a source transmitting an impulse in one borehole, and a receiver placed at the same depth in the other borehole. However, the use of more than two boreholes, measuring the wave travel time difference between adjacent receivers, are preferable, since it minimizes possible inaccuracies resulting from such as trigger time measurement and site anisotropy (Kramer, 1996; Luna and Jadi, 2000). A schematic illustration of the test setup is shown in Figure 3.11.

Both p- and s-wave velocities are measured from the cross-hole test. The

arrival of the impulse at each receiver is registered by a digital recording system, such as an oscilloscope or software on a personal computer. From this, the arrivals of the p- and s-wave is identified, and their velocities determined by the time difference between the receivers. The wave propagation velocity for the material at a specific depth is measured by fixing the source and receiver at the same depth. By doing this for several different depths, a velocity profile can be obtained (Kramer, 1996; Luna and Jadi, 2000; EPRI, 1993).

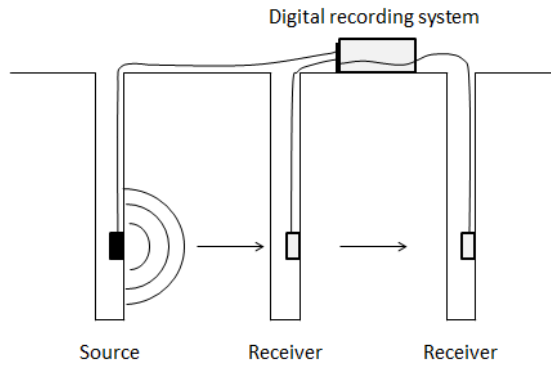


**Figure 3.11:** *Simplified illustration of a typical setup of the seismic cross-hole test.*

An explosive source may be used, however the impulse of a mechanical source is usually preferable. Examples of mechanical sources are the driving of a standard penetration test sampler, or the strike of a hammer on a rod, threaded at the bottom end, or connected to borehole packers or jacks (Kramer, 1996; EPRI, 1993). The use of a hammer blow gives the possibility of producing both HH- and HV-waves, by applying vertical and horizontal loading to the rod. It also enables for reversal of the polarity of the wave signal, by striking the rod from opposite horizontal directions. Reversing the signal may simplify the identification of the s-wave, since the registered fluctuations will be opposite for the s-waves, yet the same for the p-wave (Butcher et al., 2005; EPRI, 1993). For receivers, geophones or accelerometers may be used.

The cross-hole test is useful for depths up to 60 meters when using a mechanical source. An explosive source may give reliable results to even greater depths. However, evaluation of the wave travel distance must be done, particularly at larger depths, because the distance between receivers is likely to deviate from the surface distance between boreholes, due to inclination of boreholes (Kramer, 1996).

Analysis of cross-hole data is relatively simple for thick layers of homogeneous soils. For stratified materials of thinner layers however, it is more complicated. Multiple reflections at interfaces may cause complex wave patterns, and first arrivals may not be from the direct wave path. Shorter spacing between boreholes (3-5 m) could possibly limit this problem (EPRI, 1993).

#### **Advantages and Limitations**

Surface tests show difficulty in revealing hidden layer velocity anomalies in the material (section 3.2.2). Consequently, measurements conducted in boreholes, such as the cross-hole test, is preferable to conventional surface methods when the soil consists of layers with varying material properties (Kramer, 1996). The cross-hole technique is one of the best methods used for determining of the small-strain  $v_s$  variation with depth (Luna and Jadi, 2000).

The cross-hole test is more expensive than surface tests, and skilled operators are required (Frost and Burns, 2003). For a successful experiment, the source should be rich in shearing energy so that s-waves can be detected easily, without disturbance of p-waves. Also, the receivers should have proper frequency response, be oriented in the direction of particle motion, and be in contact with the soil (Luna and Jadi, 2000). With the strike of a sledge hammer on a rod serving as source, a complex mix of waves is created, with vibration induced to the soil throughout the whole length of the rod. This makes it difficult to interpret which waves are actually registered by the receivers. They may not be waves having a perfectly

horizontal travel path. It is also difficult to control whether the receivers are oriented in the direction of particle motion or not.

A cross-hole test is performed during this study, for determination of  $G_{max}$ . A thorough description of the setup and performance of this particular test is given in chapter 6.

### 3.2.7 Seismic Down-Hole (Up-Hole) Test

Performance of the seismic down-hole, or up-hole, test requires only one borehole. In a down-hole test, the impulse source is placed at the ground surface, close to the borehole, and one or several receivers are fixed against the borehole walls. If one receiver is used, this is lowered to different depths for repetitive measurements. Alternatively, several receivers can be placed at predetermined depths. For both cases, one receiver is also placed at the source. In the up-hole test, one or several receivers are placed at the surface, and a movable source is located at various depth in the borehole (Kramer, 1996; Luna and Jardi, 2000). An illustration of the test setup is shown in Figure 3.12. The down-hole test is preferable to the up-hole test, because s-waves are generated more easily (Kramer, 1996, Chapter 6).

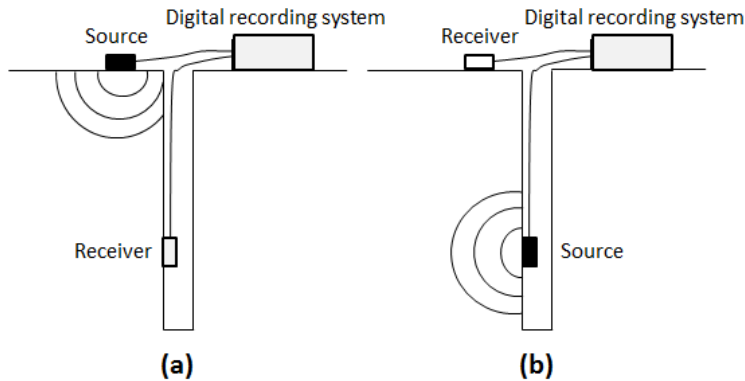


**Figure 3.12:** *Simplified illustration of a typical setup of (a) the seismic down-hole test, and (b) the seismic up-hole test. (After Kramer 1996.)*



Both p- and s-waves can be measured in the down-hole or up-hole test. The travel times from the source to each receiver are measured. The travel times can then be plotted against depth, giving the wave velocities as the inclination of each line segment, as for the seismic refraction test. Different soil layers will show different wave velocities (Kramer, 1996; Luna and Jadi, 2000).

### **Advantages and Limitations**

Since only one borehole is required, the down-hole or up-hole tests is a cheaper alternative to the cross-hole test. In addition, soil layers that can be hidden in seismic refraction investigations ("blind zones", discussed in section 3.2.2) are more easily detected in the down-hole or up-hole test, since the waves travel through all materials from the source to the receiver (Kramer, 1996). Another advantage of the down-hole test is the possibility of reversing the polarity of the source for detection of shear wave arrival.

It is more difficult to generate s-waves in an up-hole test (Luna and Jadi, 2000). Difficulties in performance and interpretation of down-hole and up-hole tests can result from "disturbance of the soil during drilling of the borehole, casing and borehole fluid effects, insufficient or excessively large impulse sources, background noise effects and groundwater table effects". At large depths, s-wave arrivals can be difficult to detect due to both material and radiation damping (Kramer, 1996).

### **3.2.8 Seismic Cone Penetration Test**

In the mid 1980's, the cross-hole and down-hole tests were established as standard techniques for dynamic testing and determination of s-wave velocity in field. However, these are relatively expensive testing methods. The seismic cone penetration test (SCPT) was developed, being a cheaper alternative to the down-hole test (Robertson et al., 1986). The SCPT is similar to the down-hole test, but does not require any prebored

hole. A seismometer is mounted in the cone barrel of a conventional cone penetrometer. During a pause in the penetrometer sounding, an energy impulse is created at the ground surface, transmitting a shear wave. The arrival time of the wave, traveling from the source to the seismometer, is measured. This is repeated at several depths, and average s-wave velocities are determined from interval arrival times measured at subsequent depths. Arrival time-depth curves can be generated, with velocities defined as the inclination of line segments (Kramer, 1996; Sully and Campanella, 1995; Luna and Jadi, 2000; Butcher et al., 2005). An illustration of the SCPT configuration is shown in Figure 3.13. An alternative configuration of the seismic cone includes two seismometers, the second one placed some distance above the cone barrel. Here, the wave arrival time of the same source activation is measured, and errors due to possible rotation of the cone drive rods are limited (Butcher et al., 2005). The SCPT is typically used in soft ground (Heymann, 2003).

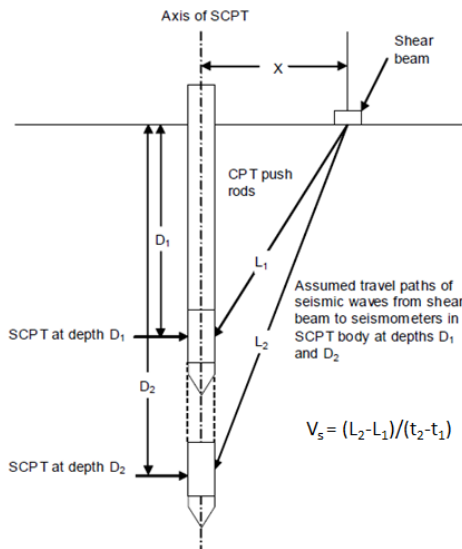


**Figure 3.13:** *Illustration of the configuration of the seismic cone penetration test. Butcher et al. (2005) suggests that the distance  $X$  should be about 1 m. (From Butcher et al. 2005.)*

#### **Cross-Hole SCPT**

At the end of the 1980's, the down-hole SCPT was modified so that cross-hole SCPT could also be performed. For accurate determination of arrival times, the University of British Columbia (UBC) considered it necessary to use two receivers in the cross-hole SCPT setup, placed at a distance of about 2-4 m (Sully and Campanella, 1992). Sully (1991) described the performance of the procedure. In a cross-hole SCPT, a strike on the top of the penetrometer rods serves as the source, generating a horizontally propagating shear wave with vertical particle motion (HV-wave). With the use of only one receiver, the s-wave velocity has to be determined from the first arrival time, which may give significant error, depending on soil conditions and signal quality. Consequently, the use of arrival time measured between two adjacent receivers are preferable (Sully and Campanella, 1992, 1995). By performance of down-hole testing together with cross-hole testing, s-wave velocities of both VH-waves (down-hole) and HV-waves (cross-hole) can be measured for examination of in situ anisotropy. A setup used for this purpose was developed at the UBC (Sully and Campanella, 1995).

#### **Advantages and Limitations**

The seismic cone penetration test has economic advantages, since no bore-holes are required. Also, several soil properties can be provided during the same test (Luna and Jadi, 2000; Robertson et al., 1986). This also makes the test less time consuming than other seismic in situ tests (Luna and Jadi, 2000). For the cross-hole SCPT however, more resources are needed due to the requirement of two or more purpose-designed vehicles, thus limiting such performances to large high-profile projects (Sully and Campanella, 1995).

### 3.2.9 Shear Beam as Energy Source

A commonly used energy source is the shear beam, which involves the strike of a sledge hammer on the ends of a beam in good contact with the ground surface (Kramer, 1996; Luna and Jadi, 2000; Butcher et al., 2005). This has been used by Heymann (2003), Sully and Campanella (1992, 1995) and Georgia Institute of Technology (Burns and Mayne, 1996), amongst others. This mechanical source is useful for the down-hole (up-hole), cross-hole and SCP tests.

"The beam can be of metal or wood encased at the ends and bottom with minimum 25 mm thick steel" (Butcher et al., 2005). Most importantly, good contact between the whole length of the beam and the ground surface must be ensured. Cleats at the bottom, penetrating the ground will prevent sliding. Also, loading from the outriggers of the cone rig or vehicle wheels will keep the beam in place (Kramer, 1996; Butcher et al., 2005). The strike of a fixed hammer with head mass between 5 and 15 kg will produce a clean shear wave with essentially no compression wave. The strike should be in the direction parallel to the long axis of the beam (Butcher et al., 2005; Sully and Campanella, 1995). This will generate a vertically propagating wave with horizontal particle motion (VH-wave) (Sully and Campanella, 1995). Repeating the procedure with strikes on both ends of the shear beam will produce shear waves of opposite polarity, due to change in direction of initial particle motion. By observing received signals from s-waves of both polarities together, the s-wave can more easily be distinguished from the p-wave, thereby giving a more reliable determination of the s-wave arrival time (Butcher et al., 2005; Luna and Jadi, 2000). An example of opposite polarized s-wave traces is given in Figure 3.14, showing the clear appearance of the s-wave. The first major cross-over may be used as a "reference" arrival for determination of interval arrival time and s-wave velocity (Butcher et al., 2005).

The same principal apply to a setup where a hammer blow on a rod penetrated into the ground is used as a mechanical source. This may be

### 3.2. FIELD TESTS

---

a good approach for the cross-hole test.

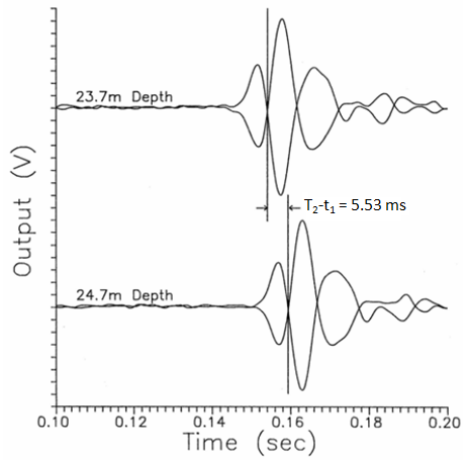


**Figure 3.14:** An example of opposite polarized shear wave traces. The clear crossover of traces can be used for determination of interval arrival time and *s*-wave velocity. (From Butcher et al. 2005.)

### 3.3 Soil Parameters influencing $G_{max}$

Research has shown that  $G_{max}$  is dependent of several other parameters. This complicates the interpretation of measured  $G_{max}$  values, and assessment must be done with care. In this section, literature concerning the effect of soil parameters on  $G_{max}$  will be presented. Continuous assessments not cited, are the authors own.

#### General

Hardin (1978) presented an expression giving  $G_{max}$  as a function of the parameters it seemed to be influenced by:

$$G_{max} = AF(e)\sigma'_m{}^n\sigma_r^{(1-n)}(OCR)^k \quad (3.6)$$

$AF(e)OCR^k$  is a stiffness quantity showing dependence on  $e$  and  $OCR$ . Further,  $A$  is an empirical constant dependent on type of soil and choice of reference stress,  $F(e)$  is a function of void ratio,  $\sigma'_m$  is the mean effective confining stress,  $\sigma_r$  is the reference stress, often taken as the atmospheric pressure,  $p_a = 100kPa$ , and  $OCR$  is the overconsolidation ratio.  $n$  and  $k$  are exponents taking different values for different soils. Equation (3.6) suggests that  $G_{max}$  is dependent on soil structure, void ratio, stress state and overconsolidation ratio. The exponent  $k$  is a function of plasticity index,  $I_p$ , hence showing a dependence also of  $I_p$ .

Jamiolkowski et al. (1991) supports the relation proposed by Hardin (1978) (equation (3.6)) by stating:

$$G_{max} = M_G p_a^{(1-n)} \sigma'_m{}^n \quad (3.7)$$

with  $M_G$  being a dimensionless modulus number depending on soil structure, void ratio function  $F(e)$  and clay mineralogy expressed via  $I_p$ .

### 3.3. SOIL PARAMETERS INFLUENCING $G_{MAX}$

In addition, laboratory testing has shown variation in  $G_{max}$  with time of consolidation (Westerlund, 1978; Kokusho et al., 1982; Jamiolkowski et al., 1991; Kramer, 1996), with  $I_p$  being an influential parameter on the rate of this change in  $G_{max}$  (Kokusho et al., 1982; Kramer, 1996). Vucetic and Dobry (1991) also reported a dependency of  $G_{max}$  on plasticity index.

On the basis of previous studies, Vucetic and Dobry (1991) summarized the effects of different factors on the shear modulus and damping. The result of this is shown in Table 3.2.

**Table 3.2:** *Effect of different factors on the shear modulus and damping ratio,  $\xi$ , of normally consolidated and moderately overconsolidated clays. (From Vucetic and Dobry 1991.)*

Influencing factor	$G_{max}$	$G/G_{max}$	Damping ratio, $\xi$
Effective mean confining pressure, $\sigma'_m$	Increases with $\sigma'_m$	Constant or increases with $\sigma'_m$	Constant or decreases with $\sigma'_m$
Void ratio, $e$	Decreases with $e$	Increases with $e$	Decreases with $e$
Geologic age $t_g$	Increases with $t_g$	May increase with $t_g$	Decreases with $t_g$
Cementation, $c$	Increases with $c$	May increase with $c$	May decrease with $c$
Overconsolidation ratio, $OCR$	Increases with $OCR$	Not affected	Not affected
Plasticity index, $I_p$	Increases if $OCR > 1$ , constant if $OCR = 1$	Increases with $I_p$	Decreases with $I_p$
Cyclic strain, $\gamma_c$	-	Decreases with $\gamma_c$	Increases with $\gamma_c$
Strain rate, $\dot{\gamma}$ (frequency of cyclic loading)	Increases with $\dot{\gamma}$	$G$ increases with $\dot{\gamma}$ , $G/G_{max}$ probably not affected if $G$ and $G_{max}$ are measured at same $\dot{\gamma}$	Constant, or may increase with $\dot{\gamma}$
Number of loading cycles, $N$	Decreases after $N$ cycles of large $\gamma_c$ , but recovers later with time	Decreases after $N$ cycles of large $\gamma_c$ ( $G_{max}$ measured before $N$ cycles)	Not significant for moderate $\gamma_c$ and $N$

#### 3.3.1 Overconsolidation Ratio

According to the expression proposed by Hardin (1978) given in equation (3.6),  $G_{max}$  is dependent on overconsolidation ratio,  $OCR$ . This is also stated in the summary of influencing factors presented by Vucetic and Dobry (1991), shown in Table 3.2.

Later research however, have shown the dependence of  $OCR$  being less significant (Kokusho et al., 1982; Shibuya et al., 1992). Laboratory tests performed by Shibuya et al. (1992) on various kinds of geomaterials with  $OCR$  varying from 1 to 4 showed little influence on  $G_{max}$ , when a correction concerning the void ratio,  $e$ , was taken into account. This indicates that with an appropriate choice of  $F(e)$ , the  $OCR$  term in equation (3.6) could be neglected, i.e.  $k = 0$ . Jamiolkowski et al. (1991) also stated the negligible effect of  $OCR$  on the shear modulus, as long as current stress level and changes in  $e$  are accounted for.

### 3.3.2 Stress State

Several studies have shown the effect of increasing  $G_{max}$  with increasing confining pressure (Hardin, 1978; Vucetic and Dobry, 1991; Jamiolkowski et al., 1991; Wang et al., 2007; Santagata et al., 2005).

After a review of previous research and performance of several resonant column tests on clean, dry sands, Yu and Richart (1984) concluded that " $G_{max}$  depends about equally on the principal stresses in the directions of wave propagation and particle motion", while effects of a third, intermediate principal stress normal to the plane through which the wave propagates is negligible. The same is stated by Jamiolkowski et al. (1991) and Santagata et al. (2005). This suggests the use of  $\sigma'_m = (\sigma'_1 + \sigma'_3)/2$  in stead of  $\sigma'_m = (\sigma'_1 + \sigma'_2 + \sigma'_3)/3$  in equation (3.6) for soils in an anisotropic stress state. For a s-wave with vertical direction of propagation and horizontal particle motion, with  $C_s$  being a material constant reflecting the soil structure,  $G_{max}$  could hence be expressed as (Jamiolkowski et al., 1991):

$$G_{max} = C_s F(e) \sigma_r^{(1-n_v-n_h)} \sigma'_v{}^{n_v} \sigma'_h{}^{n_h} \quad (3.8)$$

where  $\sigma'_v$  and  $\sigma'_h$  are the effective stresses in vertical and horizontal direction respectively, and  $n_v$  and  $n_h$  are exponents dependent on the soil conditions in the different directions. In equation (3.8), the  $OCR$  term is



### 3.3. SOIL PARAMETERS INFLUENCING $G_{MAX}$

neglected and an appropriate choice of  $F(e)$  to justify this is assumed, in accordance with the findings of Shibuya et al. (1992) and Kokusho et al. (1982), discussed in subsection 3.3.1. Yu and Richart (1984) found the effects of the two principal stresses on  $G_{max}$  to be about equal. Consequently,  $n_v = n_h$ , and equation (3.8) can be written as (Shibuya et al., 1997):

$$G_{max} = AF(e)\sigma_r^{(1-2n_v)}\sigma_v'^{2n_v} \quad (3.9)$$

where a new material constant is introduced,  $A = S_{vh}K_0^{n_v}$ .  $K_0$  is the coefficient of earth pressure at rest,  $\sigma'_h/\sigma'_v$ .

The influence of effective mean confining pressure,  $\sigma'_m$ , on the shear modulus is illustrated by the modulus reduction curves in Figure 3.15. The linear cyclic threshold shear strain is seen to increase with increasing confining pressure. The effect is evident for soil of low plasticity, while becoming far less substantial with increasing plasticity index. (Ishibashi, 1992). Due to the additional dependence on  $I_p$ , the effect of  $\sigma'_m$  on  $G_{max}$  is more evident for sands than for clays.

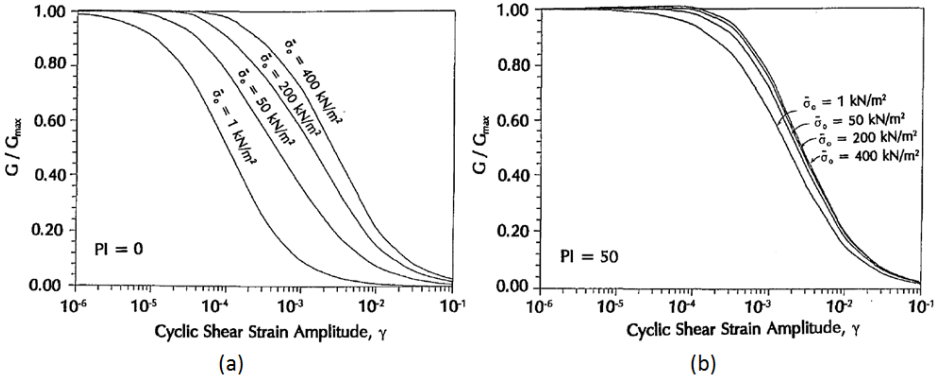


**Figure 3.15:** Influence of effective mean stress on modulus reduction curves for (a) non-plastic, and (b) plastic soil.  $\bar{\sigma}_0$  in the figure is the effective mean stress which has the notation  $\sigma'_m$  throughout this thesis. (From Ishibashi 1992.)

Kim and Novak (1981) performed laboratory testing on cohesive soils, using a resonant column apparatus, to investigate the influence of difference factors on  $v_s$  and  $G_{max}$ . Long-term consolidation under different confining pressure was performed. The results showed initial values of  $v_s$  being higher for higher initial confining pressure, and a further increase in  $v_s$  with increasing confining pressure was evident. An interesting observation was that  $v_s$  measured shortly after the application of a new confining pressure, was lower than that measured at the end of the previous stress level. However, after about 10 minutes of confinement, the velocity increase continued. This indicates a breakdown in the soil structure due to stress loading, but also, a recovering effect of the soil.

Investigations of Shibuya and Mitachi (1994) showed an exponential increase of  $G_{max}$  with increasing overburden pressure  $\sigma'_v$  on the form:

$$\frac{G_{max}}{G_{ref}} = \left( \frac{\sigma'_v}{\sigma'_{v,ref}} \right)^m \quad (3.10)$$

with the exponent  $m$  considered to be a function of shear strain level of value 1.2 on average.

### 3.3.3 Void Ratio

As Hardin (1978) presented the expression of  $G_{max}$  given in equation (3.6), he also suggested a void ratio function on the form:

$$F(e) = \frac{1}{0.3 + 0.7e^2} \quad (3.11)$$

Jamiolkowski et al. (1991) supported Hardin (1978) considering the statement of void ratio dependence, and presented another proposal of the void ratio function:

$$F(e) = \frac{1}{e^{1.3}} \quad (3.12)$$

The applicability of the void ratio function presented in equation (3.12) has been examined at a reference pressure of 98.1 kPa.

Several other investigations have also proven the effect of decreasing  $G_{max}$  with increasing void ratio,  $e$  (Kim and Novak, 1981; Vucetic and Dobry, 1991; Shibuya and Tanaka, 1996; Santagata et al., 2005).

From  $e$ - and  $\sigma'_v$ -profiles determined by seismic cone testing, Shibuya and Tanaka (1996) developed an empirical relationship, correlating the shear modulus of soft clays to  $e$  and  $\sigma'_v$  only, both parameters available from routine investigations. Multiple regression analysis were performed, seeking the best-fit relationship. This resulted in the expression:

$$G_{max} = 5.000e^{-1.5}\sigma'_v{}^{0.50} \quad (3.13)$$

where  $e$  is the void ratio, and  $\sigma'_v$  is the effective overburden pressure given in kPa. The expression in equation (3.13) seemed to be applicable to a wide range of  $e$ , between 0.5 and 5, and also to soils exhibiting a wide range of  $I_p$ .

#### 3.3.4 Anisotropy

Hardin (1978) presented results of a wave propagation test performed on sand under isotropic, and anisotropic stress conditions with a  $\sigma_1/\sigma_3$  ratio of 3. This showed that for both isotropic and anisotropic conditions,  $v_s$  was somewhat higher for propagation in the direction of  $\sigma_3$  than in the direction of  $\sigma_1$ . Lo Presti et al. (1993) presented the results of bender element testing in an oedometer, performed on horizontally and vertically cut specimens of Italian Fucino clay. Figure 3.16 illustrate the state and orientation of the specimens and wave propagation. For the vertically and horizontally cut specimens, the load applied in the oedometer is oriented in

the direction corresponding to in situ  $\sigma_1$  and  $\sigma_3$ , respectively. The wave propagates in the VH-plane of the vertically cut specimen, and in the HH-plane of the horizontally cut specimen.  $G_{max}(VH)$  and  $G_{max}(HH)$  corresponding to propagation in each plane was determined. The results showed that initial values of  $G_{max}(HH)$  were 20-30% higher than the values of  $G_{max}(VH)$ , with a decreasing difference with increasing confining pressure. This corresponds to the findings of Hardin (1978). However, due to the stress dependency of  $G_{max}$ , the assumption of larger  $v_s$  with wave propagation in the direction of in situ  $\sigma_1$  seems reasonable. Consequently, Lo Presti et al. (1993) refers to the findings as "contradictory results".

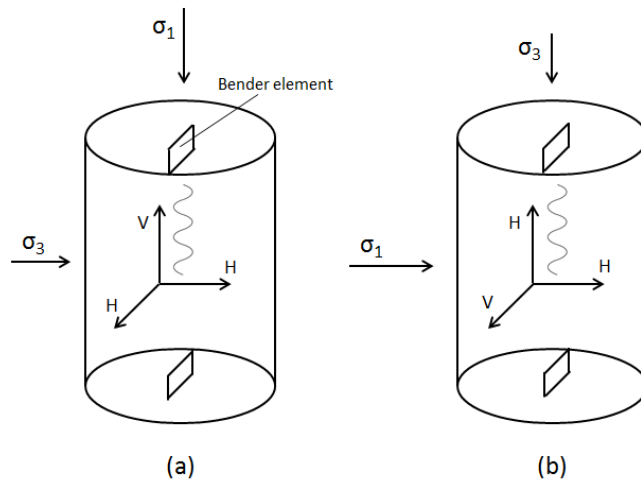


**Figure 3.16:** *Illustration of the conditions of sample during bender testing in oedometer, performed by Lo Presti et al. (1993). (a) Vertically cut specimen. (b) Horizontally cut specimen. (After Lo Presti et al. 1993.)*

### Structural and Stress Anisotropy

The shear wave velocity,  $v_s$ , depends on effective confining stress,  $\sigma'$ , and soil state or fabric, as long as only small strains are present.

$$v_s = C_s(\sigma')^n \quad (3.14)$$

where  $C_s$  is a shear wave velocity constant dependent on the soil structure and  $n$  is a stress-dependent exponent (Sully and Campanella, 1992, 1995).

Sully and Campanella (1995) performed field tests to evaluate in situ stress dependence of measured shear wave velocities. Variations in s-wave velocities with anisotropy was investigated. A s-wave can propagate in the same or a different direction than the direction of particle motion. With propagation and particle motion being in the same plane, the s-wave is considered isotropic, and the s-wave velocity denoted  $v_{sI}$ . Here, the same stress is acting in the direction of both propagation and particle motion. Conversely, with propagation and direction of particle motion being in different planes, the s-wave is considered anisotropic, and the s-wave velocity  $v_{sA}$ , since stresses are not equal in the two directions. With the right choice of source, appropriate s-waves for measurement of the velocities  $v_{sI}$  and  $v_{sA}$  can be generated in the down-hole and cross-hole test (Sully and Campanella, 1995). Sully and Campanella (1995) performed down-hole tests with transmitted VH-waves (vertical propagation, horizontal particle motion), and cross-hole tests with transmitted HV-waves (horizontal propagation, vertical particle motion), both giving anisotropic shear wave velocities,  $v_{sA}^{DH}$  and  $v_{sA}^{CH}$ . Results from these tests provided a basis for evaluation of the sensitivity of  $v_s$  (and  $G_{max}$ ) to anisotropy. If the s-wave velocities are equally sensitive to stresses in both the direction of propagation and the direction of particle motion ( $\sigma'_h$  and  $\sigma'_v$ ), measured  $v_{sA}^{DH}$  and  $v_{sA}^{CH}$  should be the same, provided equality in the shear wave velocity constants ( $C_s^{DH}=C_s^{CH}$ ). The results of Sully and Campanella (1995) showed that this was not the case. Measured  $v_{sA}^{DH}$  was not equal to  $v_{sA}^{CH}$ , hence indicating different stress dependence in the directions of propagation and particle motion. At two different sites, the  $v_{sA}^{DH}/v_{sA}^{CH}$  ratio varied with depth in ranges of about 0.7-1.8 and 1.7-2.1.

In a cross-hole test measuring both isotropic and anisotropic velocities

however,  $v_{sA}^{CH}$  was found equal to  $v_{sI}^{CH}$ , hence indicating insensitivity of the shear wave velocity to stress variations in the directions of propagation and particle motion (relative to variations in  $C_I/C_A$ ). Further, Sully and Campanella (1995) plotted variation in  $v_{sA}^{CH}/v_{sI}^{CH}$  with depth for a profile with values of  $K_0$  varying from 0.6 to more than 2. This showed negligible variation in the  $v_s$  ratio, supporting the independence of stress variation. These results indicates dependency of structural anisotropy rather than stress anisotropy. Sully and Campanella (1995) concluded that the s-wave velocity ratio  $v_{sA}/v_{sI}$  is much more sensitive to variations in the velocity constant ratio  $C_A/C_I$  than to variations in the in situ effective stress conditions.

Shibuya et al. (1997) and Yu and Richart (1984) also stated that the effect of principal stresses on  $G_{max}$  is about equal, hence substantiating the theory of  $v_s$  variation with orientation of propagation and particle motion being due to structural anisotropy.

### 3.3.5 Time of Consolidation

Systematic laboratory testing has showed that the shear modulus increases with consolidation time (Kokusho et al., 1982). After the end of primary consolidation, secondary consolidation follows. Here, Kokusho et al. (1982) showed a secondary modulus increase, and the rate of this increase is one significant parameter for cohesive soils. The ratio  $\Delta G/G_{1000}$  has been employed to quantify this rate (Kokusho et al., 1982). Kramer (1996) denotes this quantity as  $N_G$ , and states that the change of stiffness with the logarithmic time past the end of primary consolidation can be described by:

$$\Delta G_{max} = N_G(G_{max})_{1000} \quad (3.15)$$

where  $\Delta G_{max}$  is the increase in  $G_{max}$  over one log cycle of time, and  $(G_{max})_{1000}$  is the value of  $G_{max}$  at a time of 1000 minutes past the end of

primary consolidation.

The effect of structural changes due to aging on  $G_{max}$  has also shown by Jamiolkowski et al. (1991). For quantification of the rate  $N_G$ , he proposed (for  $t > t_p$ ):

$$N_G = \frac{G_{max}(t = 10t_p) - G_{max}(t = t_p)}{G_{max}(t = t_p)} \quad (3.16)$$

where  $t_p$  is the time at the end of primary consolidation.

In general:

$$N_G = \frac{\Delta G_{max}}{G_{max}(t = t_{ref}) \Delta \log(t)} \quad (3.17)$$

Kokusho et al. (1982) postulated that the most influential parameter for the rate quantity,  $N_G$ , is the plasticity index,  $I_p$ . By plotting all available research data, an evident influence of plasticity index on the rate of shear modulus increase was proven. Kokusho et al. (1982) presented an empirical relationship:

$$N_G \approx 0.027 \sqrt{I_p} \quad (3.18)$$

which is applicable for normally consolidated clay (Kramer, 1996, Chapter 6).

Santagata and Kang (2006) further substantiate these findings, stating that the increase in  $G_{max}$  observed during long-term consolidation is due to changes in the soil structure, and is more significant in clays than in sands, hence indicating the influence of plasticity. Typical values of  $N_G$  for clays, resulting from laboratory measurements, were collected from literature and presented by Santagata and Kang (2006). This shows an average  $N_G$  of 10-15 %, however, significant scatter is observed, which may be assumed to be due to the dependence of  $N_G$  to other soil parameters.

The influence of consolidation time on the shear modulus was studied by Westerlund (1978) for his PhD thesis. By laboratory testing he observed a distinct  $v_s$  with the time of consolidation, giving a corresponding increase in  $G_{max}$ . The rate of change in  $v_s$  is largest during the initial consolidation phase, and is further decreasing with time. This observation is consistent with the primary and secondary increase of  $G_{max}$  observed by Kokusho et al. (1982). Westerlund (1978) related the velocity gradient to axial deformation and pore volume. When axial deformations are constant, it is reasonable to consider also pore volume and pore pressure to be constant. At the point where this state is obtained, the velocity gradient decreases. Hence, it is reasonable to conclude that the increase in  $v_s$ , and  $G_{max}$ , before this point is influenced by the change in pore volume, while the further increase is due to secondary effects as aging (Westerlund, 1978).

The variation in  $v_s$  with time of consolidation observed by Westerlund (1978) is presented in Appendix G.

During laboratory testing on clays using a resonant column apparatus, Kim and Novak (1981) also observed the increase in  $v_s$  with time of consolidation. As for the studies of Kokusho et al. (1982) and Westerlund (1978), two phases of different rate of increasing  $v_s$  was evident, one during primary and the other during secondary consolidation. The authors explained the increase during primary consolidation as a result of change in void ratio, while the secondary increase was assumed to be a result of strengthening of particle bonding. This is consistent with the theory of Westerlund (1978).

### 3.3.6 Plasticity Index

The exponent  $k$  in equation (3.6) is dependent on the plasticity index,  $I_p$ , giving increasing values of  $k$  with increasing  $I_p$  (Table D.1). It is seen from equation (3.6) that  $G_{max}$  is independent of plasticity when  $OCR = 1$ , i.e. for normally consolidated soils. For overconsolidated soils,  $G_{max}$  increases with plasticity due to an increasing value of  $k$ .



### 3.3. SOIL PARAMETERS INFLUENCING $G_{MAX}$

As discussed in subsection 3.3.5, Kokusho et al. (1982) showed that  $I_p$  is the most influential parameter of the rate of increasing  $G_{max}$  with time of consolidation,  $N_G$ . According to equation (3.18),  $N_G$  is higher for high plasticity soils than for low plasticity soils. Also, this limits the effect to apply for clays.

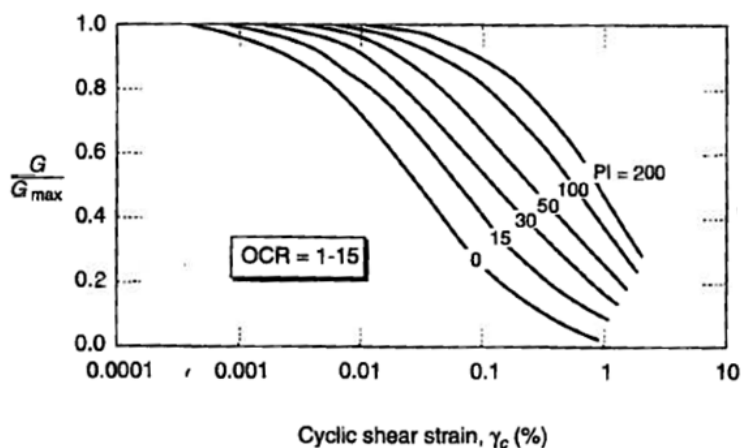


**Figure 3.17:** Modulus reduction curves for fine-grained soils of different plasticity. (From Vucetic and Dobry 1991).

Vucetic and Dobry (1991) collected results from several different studies performed on normally consolidated and slightly overconsolidated clays. Charts were presented, giving simple and practical correlations between  $I_p$  and  $e$ , and  $G/G_{max}$  (and damping ratio). Figure 3.17 shows how the modulus reduction curve is influenced by the plasticity index of the soil. The linear threshold strain,  $\gamma_{tl}$ , is defined where  $G/G_{max} = 0.99$ . This threshold can influence the manner in which a soil deposit will amplify or attenuate earthquake motions (Kramer, 1996). Therefore, it is worth noting that the linear threshold strain is higher for high-plasticity than for low-plasticity soils. Consequently, the material show linear behavior at a larger level of  $\gamma_c$ , which expands the strain range of where  $G_{max}$  is applicable (Vucetic and Dobry, 1991). This effect of  $I_p$  is also seen in Figure 3.18. Vucetic and Dobry (1991) explains the effect of linear

behavior to larger strains by differences in the microstructure of high- and low-plasticity soils.

For a given cyclic shear strain,  $G/G_{max}$  tends to increase both with increasing  $I_p$  and  $e$ . High-plasticity soils generally show higher values of  $e$  than low-plasticity soils, due to a more open soil structure, which could explain the similar effect of  $I_p$  and  $e$  on  $G/G_{max}$ . Even though the effect is similar, Vucetic and Dobry (1991) found the trend more evident for  $I_p$ . This observation may be due to the fact that  $I_p$  depends only on the composition of the soil, while  $e$  in addition depends on consolidation stresses and  $OCR$  (Vucetic and Dobry, 1991). With the procedures of index testing in mind, where  $I_p$  is determined on remoulded soil and  $e$  is determined on undisturbed soil (Statens Vegvesen, 2005), this explanation seems reasonable.

### 3.3.7 Stress and Strain History

According to Jamiolkowski et al. (1991), the effect of stress and strain history on  $G_{max}$  is negligible. This suggests the existence of a linear-elastic region encompassing the area of strains where  $G_{max}$  is valid, and consequently supports the use of linear models at small strain levels, as discussed in section 2.3.

For investigation of the effect of stress history, Shibuya et al. (1992) performed cyclic loading tests using the triaxial, plane strain compression (PSC) and torsional simple shear (TSS) apparatuses. Prestraining in these tests was limited to a number of cycles,  $N$ , of 10. The samples were consolidated to the same stress level, and for some of the samples, an initial shear stress of different magnitude was applied. Both the PSC and TSS tests showed  $G_{max}$  to be scarcely affected by the initial shear. Conclusively, Shibuya et al. (1992) stated the independence of  $G_{max}$  to consolidation stress history, cyclic pre-straining, rate of shearing and type of loading.

However, during undrained cyclic triaxial testing on saturated sand, Zhou and Chen (2005) measured lower values of  $G_{max}$  for samples subjected to high amplitude cyclic loading than for samples not holding the same stress history. The modulus reduction was observed to be higher for medium sand than for fine sand, indicating a dependence on soil type. The authors explained the decreasing effect of  $G_{max}$  by reduction of effective stress, and change in particle contact during cyclic loading. This indicates a dependence of  $G_{max}$  on stress history, and it is reasonable to assume that the effect is not necessarily equal for sands and clays.

After evaluation of previous results presented in literature, Vucetic and Dobry (1991) established a degrading effect of the shear modulus with cyclic loading. A chart representing this effect was given, and is here shown in Figure 3.18. Although the rate of cyclic stiffness degradation is increasing with an increasing number of cycles,  $N$ , the effect of  $I_p$  on  $G/G_{max}$  is much more significant. For a given cyclic shear strain,  $\gamma_c$ ,  $G$  is seen to degrade less for high-plasticity soils than for low-plasticity soils. For  $G_{max}$  however, these effects are irrelevant since they are not related to sufficiently low strains. The findings illustrated in Figure 3.18 indicate that  $G_{max}$  is not significantly influenced by strain history. Also the level of  $\gamma_c$  where the effect of cyclic loading becomes relevant is higher for high-plasticity than for low-plasticity soils. It is worth keeping in mind the difference between the general shear modulus,  $G$ , and  $G_{max}$  which is only applicable at small strains ( $<0.001\%$ ).

#### 3.3.8 Soil Structure

The increasing effect of  $G_{max}$  with time for soils subjected to constant effective stress is quite well established. It is also stated that this increase can not be an effect of change in void ratio alone. It is reasonable to believe that the soil structure, and modifications of it with time, is an important influencing factor on  $G_{max}$  (Santagata and Kang, 2006).

For both sands and clays, the soil structure formed by aging is different

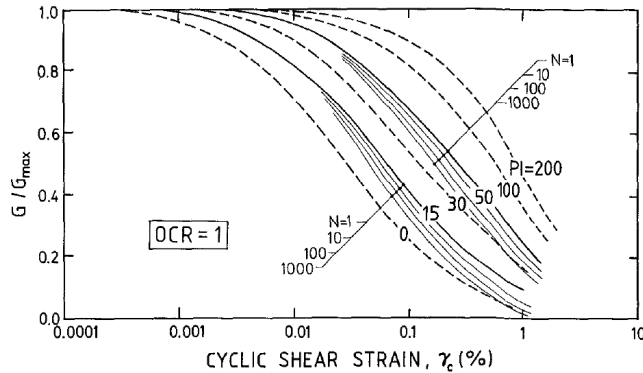


**Figure 3.18:** *Effect of degradation of shear stiffness ( $G/G_{max}$ ) due to cyclic loading for soils with  $I_p$  (in the figure denoted  $PI$ ) of 15 and 50. The broken lines illustrate the  $N = 1$  curves for  $I_p$  of 0, 30, 100 and 200. (Figure from Vucetic and Dobry 1991.)*

from that generated by an increase in stress. Sedimentary effects over a geologic period of time, bring natural deposits to a state which is difficult to replicate in the laboratory (Santagata and Kang, 2006).

All soils have some inherent properties which are independent of the natural state of the soil, with no effect of fabric and bonding. Burland (1990) referred to this as "intrinsic properties", and used it as a reference for assessment of the influence of structure on the properties of natural clays. He stated that natural clays show an enhanced resistance due to structure, compared to reconstituted clay with only intrinsic properties. However, natural clays are more sensitive, and show a brittle behavior. When the structure of a natural clay is broken, the strength drops rapidly towards the intrinsic values. Nevertheless, fabric and bonding of a soil has substantial effect on its strength. When taking a sample from field and into the laboratory, it is conceivable that some of its structure is lost. This may consequently lead to lower values of  $G_{max}$  measured in laboratory than in situ.

Wang et al. (2007) performed resonant column and triaxial compression

tests on reconstituted kaolinite soils for investigation of structural effects on mechanical response. An illustration of different structures, flocculated and face-to-face alignment is given in Figure 3.19. According to Wang et al. (2007), soils of low pH (pH=4) typically have a flocculated structure, while soils of high pH (pH=7.8) have a face-to-face alignment. Testing on both horizontally and vertically cut samples (Figure 3.16) showed about equal values of initial  $e$  for both cutting directions at pH=4. At pH=7.8 however, initial  $e$  was higher for the horizontally cut sample than for the vertically cut sample. Wang et al. (2007) explained this by higher compressibility of soils with a flocculated structure than face-to-face alignment. Higher confining pressure led to similar  $e$  in both cutting directions, also for the samples of pH=7.8. In general, low pH was seen to give larger values of  $e$ .

As part of the same study, Wang et al. (2007) reported interesting findings concerning the effects of pH on  $G_{max}$ . For confining pressures in the range 50-250 kPa,  $G_{max}$  was observed to increase with decreasing pH. Combined with the result of increasing  $e$  with decreasing pH, this consequently suggests an increasing effect of  $G_{max}$  with increasing void ratio. This behavior is inconsistent with the established effect of decreasing  $G_{max}$  with increasing  $e$  (subsection 3.3.3). According to Wang et al. (2007), "the contradiction is due to the structure effect". The attraction between grains is stronger for the flocculated structure which is representative at low pH, hence strengthening the small-strain stiffness. The face-to-face alignment, representative at high pH, consists of weak particle connections, resulting in a lower small-strain stiffness. This influence of structure on  $G_{max}$  is seen to be more evident at higher isotropic confining pressures.

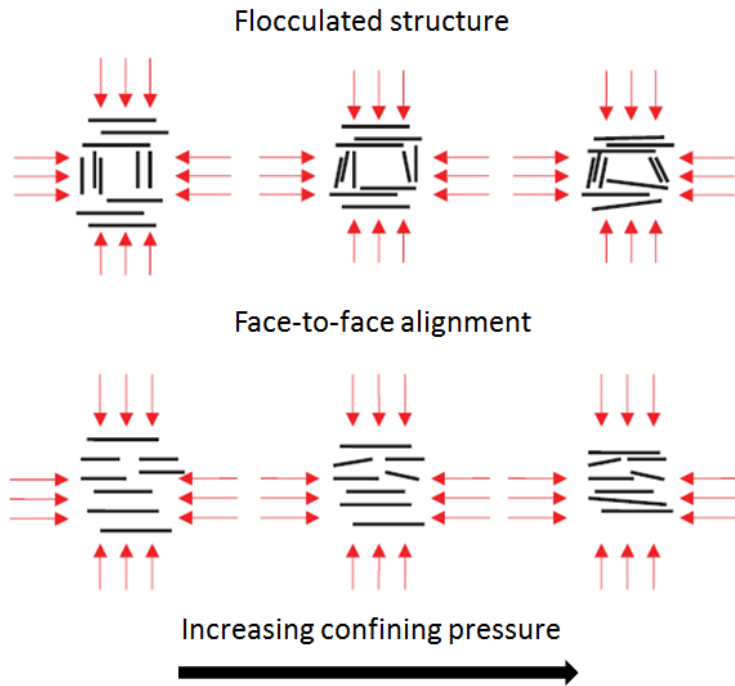


**Figure 3.19:** Illustration of volume-change mechanisms for soils of flocculated structure and face-to-face alignment. (After Wang et al. 2007.)

## Chapter 4

# $G_{max}$ as a Measure of Sample Disturbance

Disturbance of soil samples during sampling and preparation is inevitable. Consequently, samples are often expected to show soil behavior in laboratory being somewhat different from in situ behavior. Sample disturbance is a result of irrecoverable changes to the soil skeleton, (e.g. mechanical destructuration, void ratio), and a loss of effective stress (stress relief) (Tan et al., 2002; Landon et al., 2007). It is shown by laboratory testing that reconsolidation to in situ condition can largely compensate for the disturbance effect caused by stress release. However, some differences has previously been seen in the findings when it comes to the effect of sampling disturbance on the stress-strain behavior (Kirkpatrick and Khan, 1987; Graham et al., 1984).

The possibility of using  $G_{max}$  determined by bender elements during long term consolidation as a measure of sample disturbance has been discussed. Long term consolidation will give aging effects, "repairing" the sample to some extent, and in this way getting it closer to its in situ state. This is expected to be seen as an increase in  $G_{max}$  with time of consolidation. If field measurements of  $G_{max}$  are available, laboratory values can be com-

pared to this. If a large increase in laboratory values are observed, or if laboratory  $G_{max}$  do not come close to the field value at all, this may indicate significant sample disturbance (Nordal, 2013a).

## 4.1 Conventional Method for Sample Quality Assessment

Since 1995, the Norwegian Geotechnical Institute (NGI) has used the change in pore volume relative to the initial pore volume,  $\Delta e/e_0$ , to evaluate sample disturbance. Testing has shown that  $\Delta e/e_0$  is systematically influenced by sample disturbance, hence being suitable for quantification (Lunne et al., 2006). A proposed criteria for evaluation of sample disturbance as quantified by the value of  $\Delta e/e_0$  is shown in Table 4.1. The criteria proposed in Table 4.1 are mainly based on tests on marine clays with plasticity index 6%-43%, water content 20%-67%, OCR=1-4, and depth 0-25 m below ground level (Lunne et al., 2006).

**Table 4.1:** *Proposed criteria for evaluation of sample disturbance as quantified by the value of  $\Delta e/e_0$  (From Lunne et al. 2006.)*

OCR	Sample quality category			
	Very good to excellent (1)	Good to fair (2)	Poor (3)	Very poor (4)
1-2	<0.04	0.04-0.07	0.07-0.14	>0.14
2-4	<0.03	0.03-0.05	0.05-0.10	>0.10



## 4.2 Use of Shear Wave Velocity to Assess Sample Disturbance

Previous investigations using shear wave velocity,  $v_s$ , determined by both laboratory and in situ testing, for assessment of sample disturbance has been reported in literature. Tan et al. (2002) performed triaxial unconfined compression tests and undrained compression tests with bender elements on samples of a Singapore marine clay. Samples were retrieved using both Japanese thin-walled piston sampling tube and Shelby tube for assessment of the effects of sampling method and equipment on  $G_{max}$ . Seismic cone penetration (SCPTU) tests were also conducted to give independent measures of in situ shear strength and shear modulus at very low strains. Laboratory results were compared to SCPTU results, showing  $G_{max}$  measured in laboratory lower than that measured in field. This was the case for both sampling tubes, but the Shelby tube showed even lower  $G_{max}$  values than the Japanese tube, indicating that sample quality plays an important role in determination of  $G_{max}$ . The difference in laboratory  $G_{max}$  values for the Shelby and Japanese samples was shown to decrease with increasing reconsolidation stress. However, comparison of laboratory  $G_{max}$  to values measured in situ, indicated that  $G_{max}$  was still not fully recovered in the laboratory. After reconsolidation, Tan et al. (2002) observed a 10 % difference between the results from samples retrieved by different samplers, and the highest of laboratory measured values was still about 10 % lower than in situ  $G_{max}$ . As reported by Kirkpatrick and Khan (1987) and Graham et al. (1984), reconsolidation seems to recover the effect of stress relief to some extent. This recovering effect is also reported by other, as discussed in sections 3.3.2 and 3.3.5. However, due to destructuring, loss of bonding, and yielding that occurs at interparticle contacts,  $G_{max}$  cannot be fully restored (Tan et al., 2002).

### 4.2.1 Use of Portable Bender Elements for $v_s$ Measurements in Field

Conventional sample quality assessment methods, as quantification by the ratio  $\Delta e/e_0$  (section 4.1), often require destructive laboratory testing performed some time after sampling. Landon et al. (2007) proposed a nondestructive technique for sample quality assessment of soft clays, quantified by  $v_s$  measured by bender elements in field. This study included testing on Sherbrooke block samples, 76 mm diameter fixed piston tube samples with modified stainless steel Shelby tubes, 76 mm diameter free piston tube samples with standard galvanized steel Shelby tubes, and Standard Penetration Test (SPT) split spoon samples. This gave samples in a range of qualities, so that evaluation of sample disturbance could be related to specific sampling equipment and methods. By using portable bender element equipment installed in a jig as illustrated in Figure 4.1,  $v_s$  was measured immediately after sampling, without any reconsolidation. Seismic cone penetration (SCPTU) tests were also performed, measuring in situ  $v_s$  for comparison and assessment of values measured by bender elements. All bender element tests showed  $v_s$  values lower than those measured by SCPTU testing. Block sample  $v_s$  values were closest to the SCPTU values. Fixed piston tube  $v_s$  values were lower than block sample values, and free piston tube values even lower. Measurements on SPT samples showed the lowest values of  $v_s$ . The results of Landon et al. (2007) showed shear wave velocity ratios ( $v_s/v_{SCPTU}$ ) of block samples and fixed piston tube samples in the range of 0.7-0.8 and 0.65-0.7, respectively. Free piston tube and SPT samples showed  $v_s/v_{SCPTU}$  ratios of 0.3-0.5 and 0.3-0.4, respectively. The reduction in  $v_s$  for block samples was assumed to be a result of sampling stress relief, while the greater reduction in  $v_s$  for tube and SPT samples was taken as an indication of mechanical destructuration (Landon et al., 2007).

As a part of the investigations performed by Landon et al. (2007), laboratory testing was performed on each type of sample for determination of sample quality using the quantification shown in Table 4.1. The ratio

## 4.2. USE OF SHEAR WAVE VELOCITY TO ASSESS SAMPLE DISTURBANCE

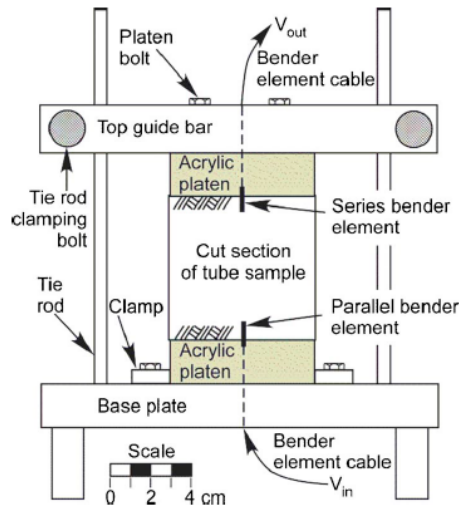


**Figure 4.1:** Schematic illustration of jig for bender element measurement of shear wave velocity in field. A similar jig, only of larger size, was used for block samples. (From Landon et al. (2007)).

$v_s/v_{SCPTU}$  was compared to the results from this conventional method for assessment of sample quality. A reduction in preconsolidation stress was observed for increasing  $\Delta e/e_0$  and decreasing  $v_s/v_{SCPTU}$ , showing a clear correlation between  $v_s/v_{SCPTU}$  and  $\Delta e/e_0$ . This observation supports the use of the ratio  $v_s/v_{SCPTU}$  for assessment of sample quality (Landon et al., 2007). Landon et al. (2007) presented a criteria for evaluation of sample quality using  $v_s/v_{SCPTU}$ , based on the same categories as those proposed by Lunne et al. (2006) (Table 4.1). This is presented in Table 4.2.

It is shown that the use of portable bender element equipment offers the potential of quality assessment in field, and thus allow for real time adjustments to sampling techniques and a more effective selection of samples for laboratory testing (Landon et al., 2007).

**Table 4.2:** Proposed criteria for evaluation of sample disturbance as quantified by the value of  $v_s/v_{SCPTU}$  (From Landon et al. 2007.)

	Sample quality category		
	Very good to excellent (1) and Good to fair (2)	Poor (3)	Very poor (4)
$v_s/v_{SCPTU}$	$\geq 0.60$	0.35-0.60	$< 0.35$

#### 4.2.2 Combination of Shear Wave Velocity and Suction Measurements for Sample Quality Classification

Donohue and Long (2010) also evaluated the use of unconfined shear wave velocity,  $v_s$ , together with suction,  $u_r$ , measurements, for assessment of sample quality in soft clay. Conventional methods, such as measurement of  $\Delta e/e_0$ , are time consuming, which is a particular problem for offshore sampling (Donohue and Long, 2010). As Landon et al. (2007), Donohue and Long (2010) sought a rapid assessment of sample disturbance to improve efficiency. Seismic cone penetration (SCPT) and multichannel analysis of surface waves (MASW) tests were performed for measurements of in situ  $v_s$ . Determination of  $v_s$  by bender elements was performed on unconfined samples. Measurement of  $u_r$  was made using several techniques, such as the filter paper method, the cell pressure loading technique, a small scale tensiometer and the "Japanese approach". Donohue and Long (2009) have previously assessed these techniques, concluding with best results for the Japanese approach and the small scale tensiometer, with the Japanese method having an advantage when it comes to speed.

The results of Donohue and Long (2010) showed highest  $v_s$  values measured on block samples immediately after sampling. After transportation to the laboratory, testing on the same blocks showed lower values of  $v_s$ . Evaluation of  $v_s/v_{insitu}$ , and comparison to  $\Delta e/e_0$ , showed best quality for block samples, followed by 76 mm tube samples. Samples from the 54 mm and the modified ELE 100 mm ( $5^\circ$  cutting edge) piston tubes

## 4.2. USE OF SHEAR WAVE VELOCITY TO ASSESS SAMPLE DISTURBANCE

---

showed poorer quality, but still better than the standard ELE 100 mm (30° cutting edge) tube and U4 samples. The superiority of block samples are consistent with the findings of Landon et al. (2007) and Lunne et al. (2006).

Suction,  $u_r$ , measurements were also compared to  $\Delta e/e_0$ , after normalization using the in situ vertical effective stress,  $\sigma'_v$ . This showed qualities of the different samples similar to that indicated by  $v_s/v_{insitu}$ . For  $\Delta e/e_0 = 0$ , the suction value tends to about  $0.2\sigma'_{v0}$  (Donohue and Long, 2010).

After observations of the relationships of  $v_s$  and  $u_r$  with  $\Delta e/e_0$ , normalized parameters used to evaluate sample disturbance was derived empirically. The result of this is given in equations (4.1) and (4.2) (Donohue and Long, 2010).

$$L_{vs} = \frac{v_{s,insitu} - v_{s0}}{v_{s,insitu} - v_{s,remoulded}} \quad (4.1)$$

$$L_u = \frac{0.2\sigma'_{v0} - u_r}{0.2\sigma'_{v0}} \quad (4.2)$$

The use of remoulded shear wave velocities in  $L_{vs}$  (Loss of velocity) takes into account the lowest possible  $v_s$  when the sample is completely destructured (Donohue and Long, 2010).  $V_{s0}$  is the unconfined shear wave velocity. Samples with  $v_{s0}$  equal to in situ  $v_s$  would be considered completely undisturbed, having a  $L_{vs}$  value of zero. The trend in suction measurements showing  $u_r$  values close to  $0.2\sigma'_{v0}$  at  $\Delta e/e_0 = 0$ , would consequently give  $L_u$  (Loss of suction)  $\approx 0$  for undisturbed samples.

From plots of  $L_{vs}$  against  $L_u$ , Donohue and Long (2010) proposed a criterion combining  $v_s$  and  $u_r$  for classification of sample quality. The classification is tabulated in Table 4.3. The classification was developed so that sample quality level determined by  $L_{vs}$  and  $L_u$  would match the  $\Delta e/e_0$  criteria presented in Table 4.1. The  $L_{vs} - L_u$  technique has an advantage

over the  $\Delta e/e_0$  criterion in terms of speed of measurement, particularly if a portable suction probe is used. However, in situ measurements of  $v_s$  that may be time consuming are required (Donohue and Long, 2010).

**Table 4.3:** *Proposed criteria for evaluation of sample disturbance, classified by the values of  $L_{vs}$  and  $L_u$  (Donohue and Long, 2010).*

Sample classification	$L_{vs}$	$L_u$
Very good to excellent	<0.65	<0.4
Good to fair	0.65-0.8	0.4-0.6
Poor	>0.8	>0.6

The sample classification system based on  $L_{vs}$  and  $L_u$  was published in 2010, however developed a few years earlier. Donohue and Long (2008) used the technique to assess the quality of both offshore and onshore samples. Classification was also done by the conventional  $\Delta e/e_0$  approach, for comparison. The results showed good correlation between the two classification systems, with only small differences in the deeper offshore samples. This investigation consequently substantiated the usefulness of the  $L_{vs}$ - $L_u$  technique.

## Chapter 5

# Installation of Bender Elements in a Triaxial Apparatus

As an initial part of the study, bender elements were installed in a triaxial apparatus in the geotechnical laboratory at NTNU. This chapter gives a brief description of the bender elements and the work performed regarding software programming and equipment setup.

### 5.1 Bender Element Specifications

The bender elements used during this study are purchased from GDS Instruments. One of the elements is specified as a s-wave transmitter, the other one as a s-wave receiver. These have different poling directions of the piezoelectric plates. The transmitter is a parallel type bender element, the receiver a series type.

The bender elements are encapsulated and mounted in inserts that can

easily be fitted into a modified pedestal and top-cap of a triaxial apparatus. Both inserts are manufactured from titanium due to its high axial rigidity and low weight, which minimize the imposed axial load when fitted into a top-cap. The protruding length of the material is about 3 mm. Optimized flexure at the element tip is achieved by fixing the element further into the insert and filling the remaining volume with flexible material. (GDS Instruments, n.d.).

## 5.2 Programming Signal and Interface

The input signal and interface for interpretation of results is built up using LabVIEW, a graphical programming software developed and provided by National Instruments. LabVIEW provides comprehensive tools to build any measurement or control application. It gives a single programming interface to multifunction data acquisition (DAQ) devices, resulting in simple hardware and software integration (National Instruments, n.d.). Any specifications governing the input signal and the display of results are built up in a block diagram. A figurative result of the programming is shown in a front panel, acting as a control window.

First, a simple sine pulse was built as input signal. Along a testing process, the block diagram was further developed to include facilities as choice of poling direction of input signal, graphing of output signal, filtering to avoid noise, and a power spectrum to identify peak frequencies.

Signals lower than half the amplitude of the programmed pulse was prevented from being plotted. This ensured that plotting of received signals started only when the applied pulse was registered, and not due to small disturbance signals. Both transmitted and received signal was plotted in the same graph. Digital cursors were made so that the time difference between the signal peaks could easily be read directly from the screen.

The resulting block diagram is presented in Appendix B.



For the first bender test element performed on Stjørdal clay, the pulse had to be applied to the bender element manually. Later, this was implemented in the program, so that a pulse was automatically applied, and a s-wave transmitted from the element every ten seconds. The bender element program was further adapted and, implemented in the conventional program used for triaxial testing. The travel time of the s-wave registered from each pulse was now given as an output together with the data registered from the triaxial test.

### 5.3 Prior Testing of Bender Elements

Initially, during the development of the input signal, only light diodes were used to ensure response from the programmed signal. The diodes were connected to a DAQ device, linking them to the LabVIEW software. After a well functioning code for signal input was established, the bender elements were connected to the DAQ, and the LabVIEW code were further developed along with testing of elements.

The transmitter and receiver element were held in contact with each other as a sine pulse was applied to the transmitter. The output signal showed response of the receiver element, with no noticeable delay. Then, the elements were inserted in a clay sample as shown in Figure 5.1. With this setup, testing confirmed that a pulse applied to the transmitter element gave a resulting wave traveling through the sample, reaching the receiver element. Different waveforms were tested as input signal; sine, cosine and square. A sine pulse turned out to be best suited, as it gave a clear output signal, similar to the input. During this testing, adjustments were done to the LabVIEW code with regards to input frequency, amplitude, receiver amplification and noise filtering.

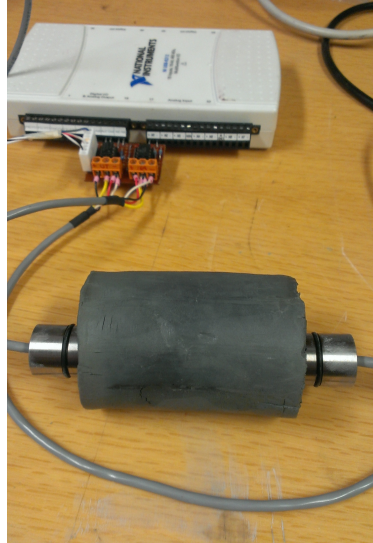


**Figure 5.1:** *Bender elements protruded into a clay sample, serving as a test setup.*

## 5.4 Equipment Setup

A DAQ device providing analog input and output for the bender elements is connected to a computer with the LabVIEW software. The transmitter element is connected to a power amplifier and the receiver element to a voltage amplifier, giving a more evident signal output. The DAQ with amplifiers and wires from bender elements connected to it is shown in Figure 5.2.

The bender elements are fixed in a pedestal and top-cap for triaxial apparatus, modified at NTNUs geotechnical workshop, as shown in Figure 5.3. Filters normally used at the top and bottom of the soil sample is replaced with thin filter paper with holes cut out for the elements. Another setup could be to fit regular filters in the modified pedestal and top cap. However, the use of filter paper is chosen due to its simplicity. Since the

## 5.4. EQUIPMENT SETUP

---

paper is very thin, it is reasonable to assume that it will not influence the soil-element interaction.

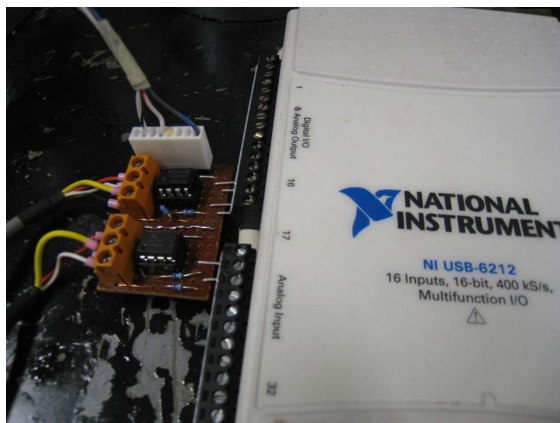


**Figure 5.2:** Multifunction data acquisition device with amplifiers connected to the bender elements.

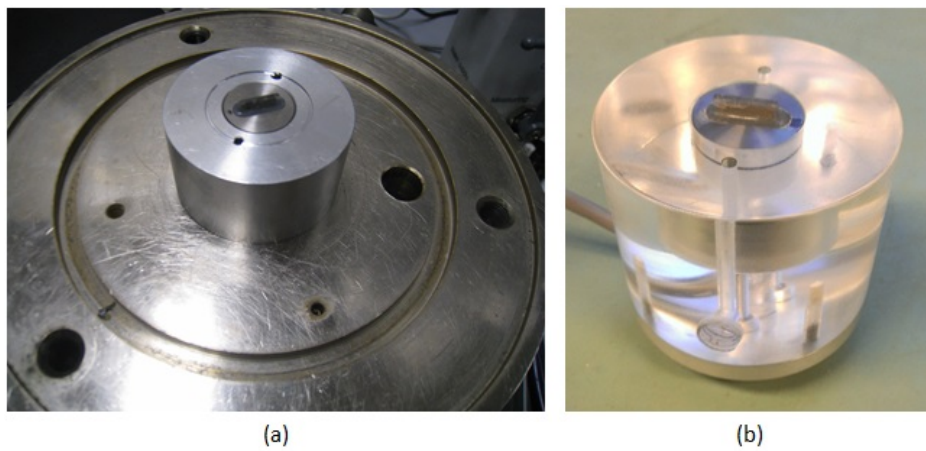


**Figure 5.3:** (a) Transmitter element fitted into modified pedestal. (b) Receiver element fitted in modified top-cap.

*CHAPTER 5. INSTALLATION OF BENDER ELEMENTS IN A  
TRIAXIAL APPARATUS*

---

## Chapter 6

# Material and Procedures of Seismic Cross-Hole Testing

As part of this study, cross-hole testing was performed at Esp, Byneset, for determination of  $G_{max}$ . The required equipment was developed at NTNU during the time of this study. Hence, performance of the test served as an experiment giving valuable experience for further improvement of the test configuration. Also, in situ measurements of shear wave velocities would hopefully give a good basis for assessment of  $G_{max}$  measured in laboratory on clay samples from the same site.

Participants in this field survey was Arnfinn Emdal, Steinar Nordal, Per Asbjørn Østensen and myself, Mirjam Knutsen.

A general description of the seismic cross-hole test is given in Section 3.2.6. This chapter describes the setup and procedures of this particular investigation. A presentation of the site and material is also given here.

## 6.1 The Esp Site

The Esp site is located within a rural zone, about 15 km west of Trondheim city, Mid-Norway. The location is shown in Figure 6.1 (a), together with a quaternary map of the area, Figure 6.1 (b).

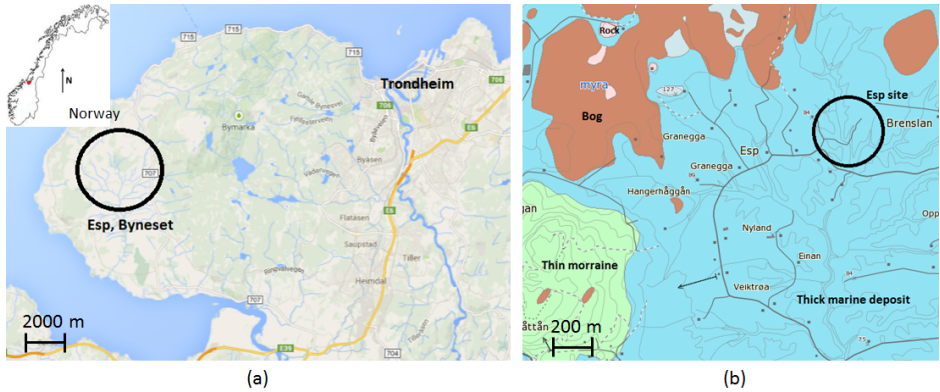


**Figure 6.1:** (a) Location of the Esp site. Map from *maps.google.com*. (b) Quaternary map of the area, from *ngu.no*.

After a landslide in January 2012, several investigations have been performed at the site, proving quick clay as a cause of the landslide, probably triggered by river erosion. Pictures of the area are shown in Figure 6.2.

## 6.2 The Esp Material

The site consists of marine clay deposit. On the basis of experience and knowledge of the area, the ground water table is assumed to be at 0.5 m depth, and  $K'_0$  is taken as 0.8.

As part of his master thesis at the Norwegian University of Science and Technology (NTNU), King (2013) performed investigations for evaluation of Esp, Byneset as a potential research site. He found that the area consists of relatively homogeneous silty clay of low plasticity and medium to high



**Figure 6.2:** (a) The landslide pit at Esp, Byneset, short time after the landslide. Picture from NIFS (2012). The red marking shows the location where cross-hole testing was performed during this study. (b) Landslide pit today, northerly direction. Picture taken at the time of cross-hole testing, May, 2014.

sensitivity. This classification is consistent with findings reported by NGU (2012), NIFS (2012) and Trondheim Municipality (2012). King (2013) identified quick clay at depths 7-7.8 m and 10-10.8 m.

For determination of soil parameters, index testing was performed on the block sample used for bender element testing. This was not an important part of the study, and interpretation is hence not emphasized. All results are given in Appendix C. Parameters relevant for determination of  $G_{max}$  are presented in Table 6.1.

One continuous loading oedometer test of constant rate of strain (CRS) was performed. Results are presented in Figure C.1. Undrained shear strength of undisturbed and remoulded samples,  $s_u$  and  $s_r$ , was determined by the falling cone test, and from this, sensitivity,  $S_r$ , was calculated. The liquid limit,  $w_l$ , was determined by the Casagrande method (Sandven, 2012a). These, and other parameters determined by index testing are presented in Table C.1 and Figure C.3. In addition, the results of a hydrometer analysis is presented in Figure C.2. All tests were performed according to Handbook 014 of the Norwegian Public Roads Administration (Statens Vegvesen, 2005).

Undrained shear strength of 24 kPa puts the sample at the upper end of the range for soft clays (Sandven, 2012a). A material is classified as "quick" when the sensitivity,  $S_t$ , is greater than 30 and the remoulded shear strength,  $s_r$ , is less than 0.5 kPa (NGF, 1982). Based on results of index testing (Appendix C, Table C), the Esp clay at 8.3 m depth used for bender element testing was classified as quick.

**Table 6.1:** *Material properties of Esp clay, used for determination of  $G_{max}$ .*

Depth, $z$ [m]	Density, $\rho$ [g/cm <sup>3</sup> ]	Unit weight, $\gamma$ [kN/m <sup>3</sup> ]	Plasticity index, $I_p$ [%]	Void ratio, $e$ [-]	$OCR$	$K'_0$ [-]
8.3	1.89	18.5	24	1.2	2.6	0.8

### 6.3 Cross-Hole Test Setup

Ahead of the field survey, Per Asbjørn Østensen prepared two accelerometers, serving as receivers during the cross-hole testing. These were placed in the ground by Anders Samstad Gylland and Gunnar Winther.

Each accelerometer was placed at 8 m depth inside a plastic tube, which was penetrated through holes prebored by 76 mm total sounding. A steel rod with screw threads at the bottom end would serve as source when given a hammer blow. This was penetrated through a prebored hole and screwed in place the last part, down to 8 m depth. The distance between the accelerometers (A1 and A2) was 5 m, and the distance from the steel rod to A1 was 2 m, all placed along one straight line. The test setup is illustrated in Figure 6.3 (a), and the picture in Figure 6.3 (b) shows the exact setup at the site.

The strike of a sledge hammer on the steel rod served as a mechanical source, inducing seismic waves into the ground. The arrival of the waves at A1 and A2 was registered by the accelerometers, and the received signal was sent to a computer giving a visual plot of amplitude fluctuation



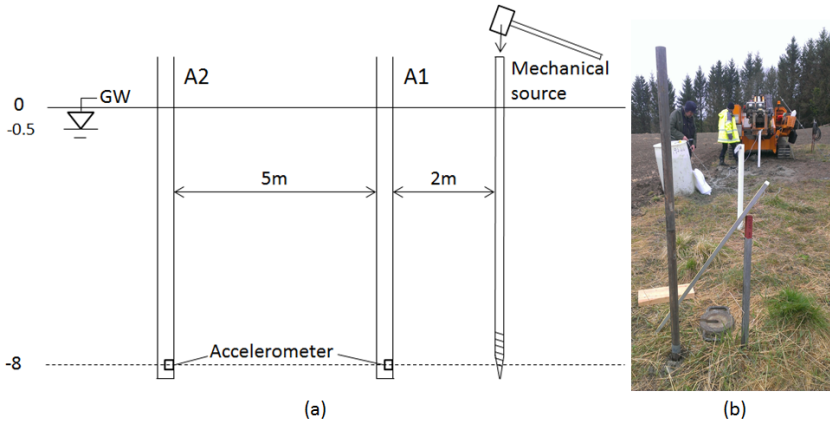


**Figure 6.3:** (a) Illustration of the setup of the seismic cross-hole test performed at the Esp site at Byneset. The stroke of a sledge hammer was used as a mechanical source, and two accelerometers served as receivers. (b) Picture showing the actual setup. The steel rod is seen in the front of the picture, and aligned with this follows the plastic tubes with A1 and A2, respectively.

in a program specifically developed by Per Asbjørn Østensen for this purpose, using the LabView software (National Instruments, n.d.). Each accelerometer detects signals in three directions, x- and y-direction being in the horizontal plane, and z-direction in the vertical plane. An example of the presentation of received signals given on the computer is shown in Figure 6.4. The s-wave travel time measured from A1 to A2 was used for determination of the shear wave velocity,  $v_s$ , and further of  $G_{max}$ .

## 6.4 Performance of the Cross-Hole Test

### 6.4.1 Verticality Check of Tubes with Accelerometers

Before starting the test, the verticality of the tubes with the accelerometers was checked. This was important to ensure alignment of the accelerometers at 8 m depth, and for determination of the exact distance between

## CHAPTER 6. MATERIAL AND PROCEDURES OF SEISMIC CROSS-HOLE TESTING

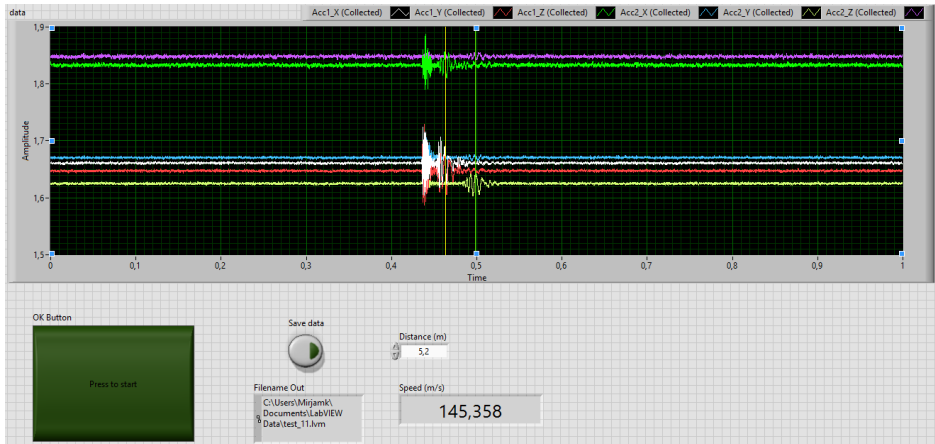


**Figure 6.4:** An example of the presentation of received signals from cross-hole testing. Both A1 and A2 detect signals in  $x$ -,  $y$ - and  $z$ -direction, hence giving a total of six plotted curves. The program is developed by Per Asbjørn Østensen, using the LabView software provided by National Instruments (National Instruments, n.d.).

A1 and A2. A rod with two circular blocks attached to it, special made to fit in the tube and ensure centering of the rod, was held down into the tube. A 1.2 m long level was held up to the part of the rod sticking out of the tube and corrected so that it was perfectly vertical. While the level was held right up to the rod in the lower end, the spacing between the rod and the top end of the level was measured. A picture of this is shown in Figure 6.5 (a). From the measured spacing, the inclination of the tube could be determined, and relating this to the geometry below the surface gave the displacement of the accelerometers at 8 m depth relative to a vertical centerline. For clarification of the procedure and the way of thinking, an illustration of the inclination and geometry calculations are given in Figure 6.5 (b).

Both accelerometers were found to slent outwardly relative to the vertical centerline, consequently, increasing the distance between A1 and A2. The distance between the plastic tubes at the ground surface was measured

## 6.4. PERFORMANCE OF THE CROSS-HOLE TEST

to be 5.02 m. With an additional total displacement of A1 and A2 at 8 m depth found to be 195 mm (Figure 6.5b), the total distance between the accelerometers was approximately 5.2 m. This was taken as the travel distance of the seismic waves during the cross-hole test.

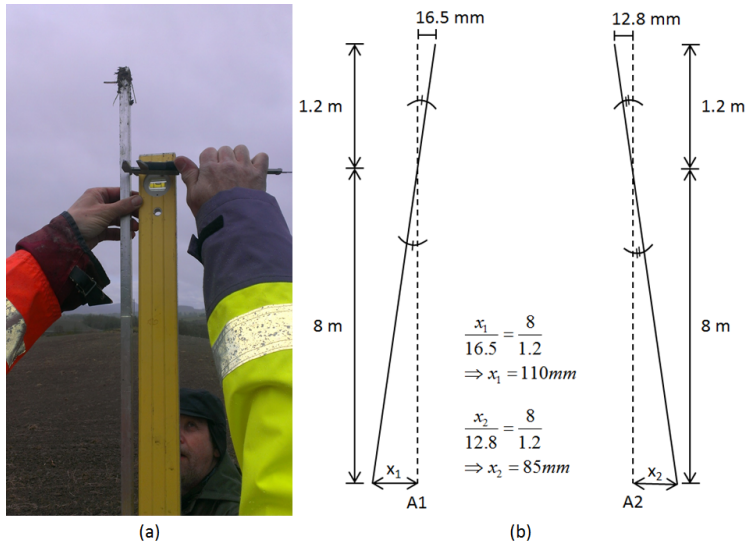


**Figure 6.5:** Determination of the inclination of the tubes with accelerometers using a straight rod and a level held perfectly vertical. (a) The displacement at the top relative to a vertical level was measured. Simple geometry calculations then gave the inclination of the tube, and further the displacement of the accelerometers at the bottom. (b) Illustration of inclination and geometry calculations for determination of displacement of accelerometer at 8 m depth. The figure is not made to scale.

### 6.4.2 Producing and Registration of Seismic Signal

The steel rod was given a hammer blow, producing vibrations and hence, inducing seismic waves in the ground. The arrival of the waves was registered at A1 and A2 and observed on a computer screen, using a program developed in LabView (Section 6.3, Figure 6.4).

The steel rod was struck from several directions to produce different wave propagations, giving a diverse range of signals for observation and assessment. A vertical strike on top of the rod was expected to give significant fluctuation effects in the z-direction. However, any signal in the z-direction proved to be difficult to identify directly from the raw data presented on the computer screen. Experimentation showed that horizontal strikes gave the most evident signal at A1 and A2. The rod was struck horizontally (strike at the side of the rod, i.e. impact direction parallel with the ground surface) in directions both parallel and normal to the wave propagation direction of interest. In each direction, the rod was struck at both sides for reversal of the particle motion. This was done in the hope that it would be seen in the plot of received signals, and be useful for identification of the s-wave, as discussed in section 3.2.9. An illustration of the directions of which the rod was struck is shown in Figure 6.6.

Subsequent to the field survey, results were plotted for further interpretation. The s-wave arrival at the two accelerometers were identified, consequently giving the s-wave travel time as the time difference.  $V_s$  was further calculated, based on a travel distance of 5.2 m.

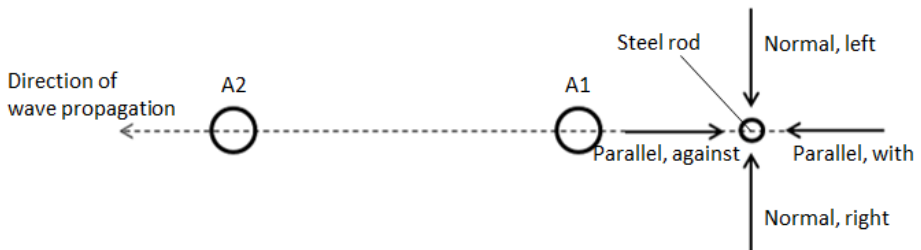


**Figure 6.6:** *Illustration of directions of horizontal strikes, seen from above. "Parallel, against" refers to a strike parallel to, but in direction against wave propagation. "Parallel, with" refers to a strike parallel to, and in direction with wave propagation. "Normal, right" and "normal, left" refers to strikes normal to the direction of wave propagation, and from the right to the left and from the left to the right, respectively. Left and right are defined as standing by the rod looking towards A1 and A2.*

## Chapter 7

# Material and Procedures of Bender Element Testing

Laboratory testing has been performed using bender elements in a triaxial apparatus for determination of  $G_{max}$ . Setup and procedure of the triaxial test is performed according to Handbook 014 given by the Norwegian Public Roads Administration (Statens Vegvesen, 2005).

According to Viggiani and Atkinson (1995) and Ibrahim et al. (2011), the s-wave travel time is most accurately determined from a sine pulse excitation. On the basis of this, a sine pulse is chosen as output signal. Testing is performed with frequencies of about 2.3-2.6 kHz.

Clay samples from sites at Stjørdal, Tiller and Esp have been used. Figure 7.1 shows one of the samples prepared in the triaxial apparatus.

This chapter describes the general performance of the bender element tests, with supplementary descriptions for each particular test. Presentations of sites and materials are also given here.

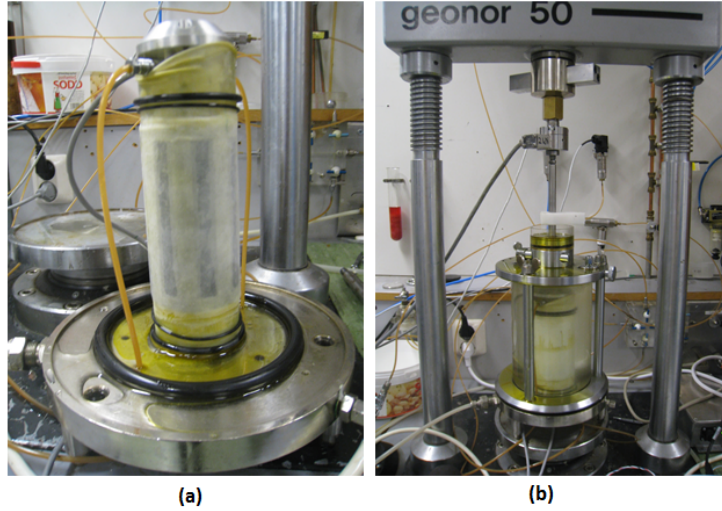


**Figure 7.1:** (a) Clay sample wrapped in filter paper and rubber skin. (b) Final setup of the triaxial apparatus.

## 7.1 Consolidation and Shear Test

All samples were left to consolidate for several hours. The objective of this long-term consolidation, was to assess the influence of secondary effects on  $v_s$ . The sample was given a chance to further "repair itself", getting closer to its in situ state. On the basis of findings of previous studies, discussed in subsection 3.3.5, it was expected to observe an increase in  $G_{max}$  with consolidation time, as a consequence of secondary effects.

A burette was connected to the triaxial apparatus, measuring the amount of water expelled from the sample during consolidation. The amount of expelled water gives an indication of sample disturbance (Statens Vegvesen, 2005).

Due to expelled water, consolidation leads to a small reduction of the sample volume. For all tests performed, a correction was done according

## 7.1. CONSOLIDATION AND SHEAR TEST

---

to equation (7.1), as described by Sandven (2012*b*), giving the sample area after consolidation. The axial stress was continuously related to the corrected area.

$$A_a = A_0 \frac{1 - (\Delta V/V_0)}{1 - (\Delta V/3V_0)} \quad (7.1)$$

$A_a$  is the sample area after consolidation,  $A_0$  is the build-in sample area,  $V_0$  is the build-in sample volume,  $h_0$  is the build-in sample height, and  $\Delta V$  is the change in sample volume during consolidation, which is equal to the amount of expelled pore water.

Further, during the shear tests, correction of cross-sectional area due to increasing shear strain was done as described by Sandven (2012*b*), using equation (7.2). Axial stress was calculated on the basis of the corrected area.

$$A_s = \frac{A_a}{1 - \varepsilon} \quad (7.2)$$

$A_s$  is the corrected area,  $A_a$  is the sample area after consolidation, and  $\varepsilon$  is strain,  $\frac{\Delta L}{L_0}$ .  $L_0$  was taken as the height of the sample after end of long-term consolidation.

Performance of the shear test was not an important part of the study, but was nevertheless performed for most of the samples since the setup was ready. A global  $G_{max}$  can be determined from the stress-strain curve resulting from the shear test, and this may be used for comparison and assessment of  $G_{max}$  obtained by bender element testing.

Since the interpretation of the shear tests is not emphasized, the results are not presented in the main part of the thesis, but given in Appendix F.

## 7.2 Interpretation of Tests

For interpretation of the tests, the s-wave travel distance was taken as the tip-to-tip distance between the bender elements. Further, the travel time was determined from the first evident peaks of the transmitted and received s-wave, as recommended by Viggiani and Atkinson (1995). An example of the output window showing the peak-to-peak difference is given in Figure 7.2. With bender elements of length 2-3 mm and soil samples of height 100 mm, the initial tip-to-tip distance was taken as 95 mm. This was adjusted with increasing strain. All strains were assumed to be axial, giving a decrease in travel distance equal to registered deformation. As the travel time and travel distance of the s-wave was known,  $v_s$  was calculated, and  $G_{max}$  determined using equation (3.1).

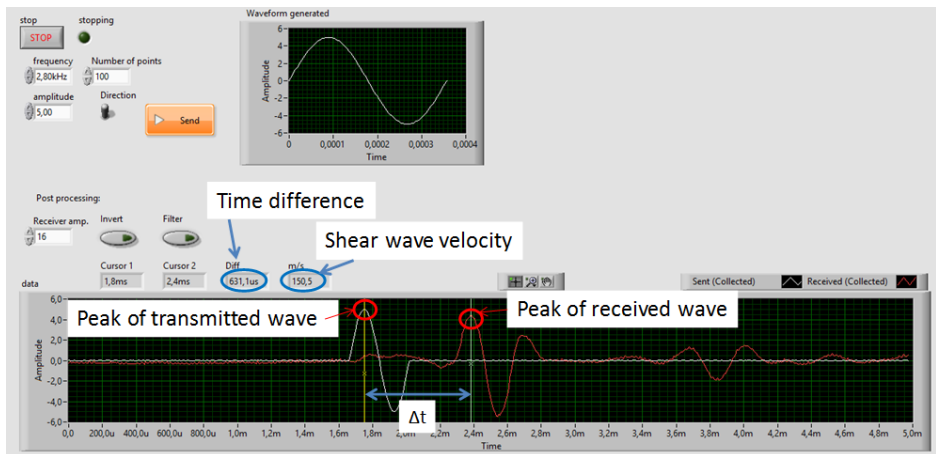


**Figure 7.2:** Example of the output shown when applying a pulse to the bender elements. White curve shows transmitted wave, red curve shows received wave.



## 7.3 Testing on Stjørdal clay

Bender element testing on Stjørdal clay was performed on two samples, both retrieved with a 54 mm steel tube sampler. The samples were from almost the same depth, 12.5 m and 12.2 m.

### 7.3.1 The Stjørdal Site

The Stjørdal site is located within an industrial area, about 30 km north-east of Trondheim, Mid-Norway. The location is shown in Figure 7.3(a), together with a quaternary map, Figure 7.3(b). The site is built up with masses pumped up from the sea floor. Field investigations indicate uniform layering over the area. The ground water table is at about 2 m depth. (Amdal et al., 2012).

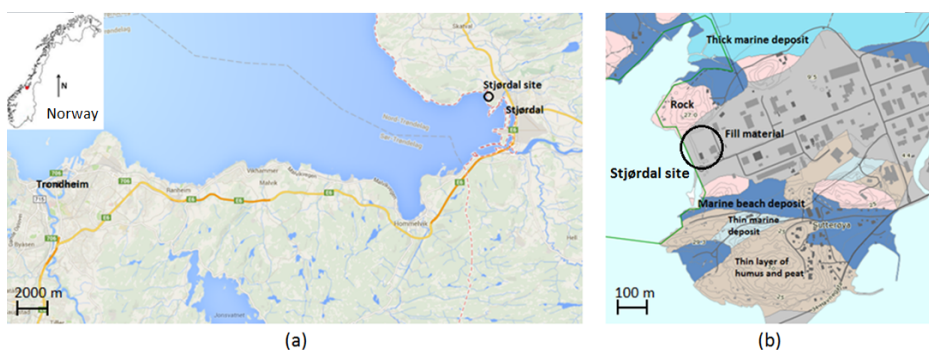


**Figure 7.3:** (a) Location of the Stjørdal site. Map from *maps.google.com*. (b) Quaternary map of the area, from *ngu.no*.

### 7.3.2 The Stjørdal Material

Field and laboratory testing has previously been performed by the author during the NTNU course "Geotechnics, Field and Laboratory Investigations", Autumn of 2012. Required soil parameters were collected from

these tests and are shown in Table 7.1.

The Stjørdal site consists of marine clay with a top layer of graded sand. The clay is classified as a medium stiff clay with low to medium sensitivity. At 12 m depth, previous field and laboratory testing indicate homogeneous clay, with some elements of silty clay (Amdal et al., 2012).

**Table 7.1:** *Material properties for Stjørdal clay.*

Depth, $z$ [m]	Density, $\rho$ [g/cm <sup>3</sup> ]	Unit weight, $\gamma$ [kN/m <sup>3</sup> ]	Plasticity index, $I_p$ [%]	Void ratio, $e$ [-]	$OCR$	$K'_0$ [-]
12-12.5	1.95	19	18	0,904	1,7	0,8

### 7.3.3 Consolidation

#### The First Stjørdal Test

The first Stjørdal sample was taken from depth 12.5 m, and the ground water table at the site is at depth 2 m (Amdal et al., 2012). From this, and properties presented in Table 7.1, in situ stresses were determined.

$$\begin{aligned}\sigma'_{y0} &= \gamma z - \gamma_w z_w \\ &= 19kN/m^3 \times 12.5m - 10kN/m^3 \times 10.5m = 132.5kPa\end{aligned}\tag{7.3}$$

$$\sigma'_{x0} = K'_0 \times \sigma'_{y0} = 0.8 \times 132.5kPa = 106kPa\tag{7.4}$$

The clay sample was consolidated to initial stresses as defined in equations (7.3) and (7.4) by setting the cell pressure to 106 kPa and applying an external axial load of 27 kPa, giving total axial load equal to 133 kPa.

It would be preferable to transmit s-waves to the sample during the initial part of consolidation to see whether variation in  $G_{max}$  was noticeable here. Due to computer problems, this was however, not done.

After consolidation to in situ stresses was completed, a pulse was applied to the bender element, transmitting a s-wave to the sample. Then, the sample was left to consolidate in drained state for 15 hours, before transmitting another s-wave.

#### The Second Stjørdal Test

The second Stjørdal sample was taken from depth 12.2 m. In situ stresses were determined as:

$$\begin{aligned}\sigma'_{y0} &= \gamma z - \gamma_w z_w \\ &= 19kN/m^3 \times 12.2m - 10kN/m^3 \times 10.2m = 129.8kPa\end{aligned}\quad (7.5)$$

$$\sigma'_{x0} = K'_0 \times \sigma'_{y0} = 0.8 \times 129.8kPa = 103.8kPa \quad (7.6)$$

The sample was consolidated anisotropic to in situ stresses as defined in equations (7.5) and (7.6). This was obtained by setting the cell pressure to 103 kPa and applying an external axial load of 26 kPa from the piston, giving a total axial load of 129 kPa.

The sample was left to consolidate in drained state for 24 hours for the purpose of observing the development of  $v_s$  with time of consolidation.

#### 7.3.4 Shear Test

##### The First Stjørdal Test

A shear test was run with 3,00 mm deformation per hour until 10 mm sample deformation. During the shear test, a s-wave was generated every 30 minutes.

## The Second Stjørdal Test

After 24 hours of consolidation, an undrained shear test was run with 3.00 mm deformation per hour until 20 mm sample deformation.

## 7.4 Testing on Tiller Clay

Bender element testing on Tiller clay was performed on a block sample taken from depth 9.1 m.

### 7.4.1 The Tiller Site

The Tiller site is located within a quick clay hazard zone ([www.skrednett.no](http://www.skrednett.no)), about 10 km south-east of the city of Trondheim, Mid-Norway. The location is shown in Figure 7.4, together with a quaternary map. It is one of several sites which has been established during research on engineering properties and behavior of marine clay with high sensitivity. The ground water table is at about 1.5 m depth (Gylland et al., 2013).

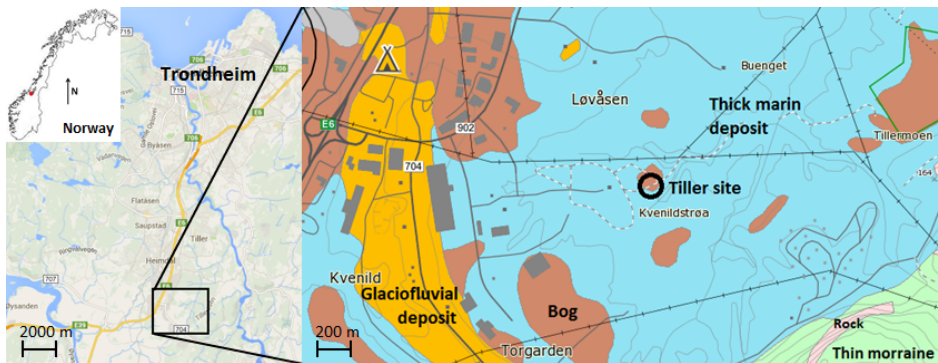


**Figure 7.4:** Location of the Tiller site shown together with a quaternary map of the area ([www.ngu.no](http://www.ngu.no)). Map from [www.google.com](http://www.google.com).

### 7.4.2 The Tiller Material

The site consists of uniform soft clay with high sensitivity.

Gylland et al. (2013) has presented results from laboratory and field investigations at the site. A brief summary is given here.

Between 2.5 m and 13.5 m, particle size distribution curves show an average clay content of about 38% and the remainder of the material being made up of approximately equal percentages of fine, medium and coarse silt (Gylland et al., 2013). Based on this particle size distribution, the material should be determined clay (NGF, 1982).

The water content is quite homogenous, with values in the range of 25% to 45% and an average value of 37.8%. At 9.1 m depth, the water content is about 40% (Gylland et al., 2013).

Previous investigations show good consistency of the plasticity index,  $I_p$ , with an average value of 6.3% (Gylland et al., 2013). Hence, the material can be classified as being of "low plasticity" (NGF, 1982). At 9.1 m depth, the plasticity index is about 5.5% (Gylland et al., 2013).

Bulk density values also show good consistency of the material with depth. Measured values range between  $1.8 \text{ Mg/m}^3$  and  $1.95 \text{ Mg/m}^3$ , with an average of about  $1.89 \text{ Mg/m}^3$ . At 9.1 m depth the bulk density,  $\rho$ , is about  $1.9 \text{ Mg/m}^3$  and  $e$  is about 1.07.

A material is classified as "quick" when the sensitivity,  $S_t$ , is greater than 30 and the remoulded shear strength,  $s_r$ , is less than 0.5 kPa (NGF, 1982). Measurements on samples from the Tiller site show that quick clay is present below 8 m depth (Gylland et al., 2013).

On the basis of experience and knowledge of the area,  $K'_0$  was taken as 0.7.

Parameters relevant for determination of  $G_{max}$  are presented in Table 7.2.

**Table 7.2:** *Material properties for Tiller clay.*

Depth, $z$ [m]	Density, $\rho$ [g/cm <sup>3</sup> ]	Unit weight, $\gamma$ [kN/m <sup>3</sup> ]	Plasticity index, $I_p$ [%]	Void ratio, $e$ [-]	$OCR$	$K'_0$ [-]
9.1	1.9	18.6	5.5	1.07	1.8	0.7

### 7.4.3 Consolidation

In situ stresses were determined as:

$$\begin{aligned}\sigma'_{y0} &= \gamma z - \gamma_w z_w \\ &= 18.6 \text{ kN/m}^3 \times 9.1 \text{ m} - 10 \text{ kN/m}^3 \times 7.6 \text{ m} = 93.3 \text{ kPa}\end{aligned}\tag{7.7}$$

$$\sigma'_{x0} = K'_0 \times \sigma'_{y0} = 0.7 \times 93.3 \text{ kPa} = 65.3 \text{ kPa}\tag{7.8}$$

The sample was consolidated anisotropic to in situ stresses as defined in equations (7.7) and (7.8). This was done by setting the cell pressure to 65 kPa and applying an external axial load of 28 kPa from the piston, giving a total axial load of 93 kPa. Because of the high sensitivity of the clay (Section 7.4.2), the external vertical load was not applied all in once, but stepwise over a period of about 10 minutes.

The sample was left to consolidate in drained state for 100 hours for the purpose of observing the development of  $v_s$  with time of consolidation.

Oedometer tests performed in the 1990's, and last time in 2012, indicates preconsolidation stress,  $p'_c$ , of approximately 170 kPa at depth 9.1 m (Gylland et al., 2013). After almost 42 hours of consolidation, the external axial load was increased to give total axial stress of 124 kPa. The cell pressure was also adjusted, using  $K'_0 = 0.7$  as before, giving total horizontal stress of 87 kPa. As an experiment, it was desirable to look at the response of  $v_s$  when the stress level was set higher than the overburden pressure, but still surely lower than the preconsolidation stress.

### 7.4.4 Shear Test

After 100 hours of consolidation, a shear test was run with 3 mm deformation per hour until 10 mm sample deformation.

## 7.5 Testing on Esp Clay

Description of the Esp site and material is previously given in sections 6.1 and 6.2. The samples used for laboratory testing with bender elements were block samples from depth 8.3 m. Both tests were performed on samples from the same block, hence consolidation was done to the same stress level.

The block sample was retrieved May 9th and opened May 12th, 2014. The bender element tests were initiated May 12th and May 22th, 2014.

### 7.5.1 Consolidation

In situ stresses were determined as:

$$\begin{aligned}\sigma'_{y0} &= \gamma z - \gamma_w z_w \\ &= 19kN/m^3 \times 8.3m - 10kN/m^3 \times 7.78m = 79.9kPa\end{aligned}\tag{7.9}$$

$$\sigma'_{x0} = K'_0 \times \sigma'_{y0} = 0.8 \times 79.9kPa = 63.9kPa\tag{7.10}$$

Both samples were consolidated anisotropic to in situ stresses as defined in equations (7.9) and (7.10). This was done by setting the cell pressure to 64 kPa and applying an external axial load of 16 kPa from the piston, giving a total axial load of 80 kPa. Because of the high sensitivity of the clay (Section 6.2), the external axial load was applied stepwise.

### **The First Esp Test**

The sample was left to consolidate in drained state for 39 hours for the purpose of observing the development of  $v_s$  with time of consolidation.

### **The Second Esp Test**

The sample was left to consolidate in drained state for 99 hours for the purpose of observing the development of  $v_S$  velocity with time of consolidation.

Due to a computer problem, measurements of  $v_s$  stopped after about 6 hours of consolidation. The sample was nevertheless left for further consolidation. After a total of 95 hours,  $v_s$  measurements were started again.

### **7.5.2 Shear Test**

A shear test was performed only on the second sample of Esp clay. The test was run with 3 mm deformation per hour until 10 mm sample deformation.

## **7.6 Testing on Short Sample of Esp Clay**

For assessment of disturbance and complex effects close to the bender element, a test was run on a sample of half height, i.e. 5 cm. The test was performed on a sample from the same block of Esp clay as that used for testing on full-height samples.

With no disturbing effects, the s-wave velocity should be equal in the same material, independent of travel distance.



### 7.6.1 Consolidation

The sample was consolidated anisotropic to the situ stresses as given in equations (7.10) and (7.9). Due to high sensitivity of the clay, the external axial load was applied stepwise over a period of about 10 minutes.

The sample was left to consolidate in drained state for 12.5 hours, for the purpose of observing the development in  $v_s$  with time of consolidation.

No shear test was run.

*CHAPTER 7. MATERIAL AND PROCEDURES OF BENDER  
ELEMENT TESTING*

---

## Chapter 8

# Summary of Results

A summary of results regarding determination of  $G_{max}$  by bender element and cross-hole testing is presented here. Further results are presented in chapters 9 and 10, with continuous discussion.

### 8.1 Results of Bender Element Testing

Results of laboratory testing performed using bender elements are presented in tables. Values of  $G_{max}$  measured during all tests are collected in table 8.1. A more thorough presentations of the results are given in Tables 8.2-8.7. Presented values are selected to show points were a measurable change in  $G_{max}$  is observed.

**Table 8.1:**  $G_{max}$  values after consolidation and shear test, given in MPa.

	End of consolidation to in situ stresses	End of long term consolidation	End of shear test	Empirical value
First test Stjørdal clay	37	40	37	77
Second test Stjørdal clay	29	47	26	84
Tiller clay	20	30	13	50
First test Esp clay	24	27	-	48
Second test Esp clay	12	30	15	48
Short sample of Esp clay	15	21	-	48

Table 8.2: Numerical results of the first bender element test performed on Stjørdal clay.

CONSOLIDATION									
Time past consolidation to in situ stresses [h]	Vertical stress, $\sigma_v$ [kPa]	Horizontal stress, $\sigma_x$ [kPa]	Pore sure, $u$ [kPa]	Deformation, $\Delta L$ [mm]	Shear wave travel distance, $l_s$ [m]	Shear wave travel time, $t_s$ [ $\mu$ s]	Shear wave velocity, $v_s$ [m/s]	Shear wave modulus, $G_{max}$ [MPa]	
0	132	105	22	0	0.095	693	137.1	36.7	
15	132	105	22	0	0.095	662	143.5	40.2	
SHEAR TEST									
Time past start of shear test [min]	Vertical stress, $\sigma_v$ [kPa]	Horizontal stress, $\sigma_x$ [kPa]	Pore sure, $u$ [kPa]	Deformation, $\Delta L$ [mm]	Shear wave travel distance, $l_s$ [m]	Shear wave travel time, $t_s$ [ $\mu$ s]	Shear wave velocity, $v_s$ [m/s]	Shear wave modulus, $G_{max}$ [MPa]	
0	132	105	22	0	0.095	662	143.5	40.2	
30	218	105	32	1.5	0.093	653	145.5	39.9	
60	230	105	34	3.1	0.092	644	147.4	39.7	
90	243	105	28	4.6	0.090	631	150.5	40.0	
120	264	105	34	6.1	0.089	627	151.6	39.2	
150	263	105	39	7.7	0.087	631	150.5	37.4	
180	267	105	43	9.2	0.086	627	151.6	36.6	
200	249	105	35	10.0	0.085	618	153.8	36.9	

**Table 8.3:** Numerical results of the second bender element test performed on Stjørdal clay.

<b>CONSOLIDATION</b>										
Time past start of consolidation [min]	Vertical stress, $\sigma_y$ [kPa]	Horizontal stress, $\sigma_x$ [kPa]	Pore sure, $u$ [kPa]	Deformation, $\Delta L$ [mm]	Shear wave travel distance, $l_s$ [m]	Shear wave travel time, $t_s$ [ $\mu$ s]	Shear wave velocity, $v_s$ [m/s]	Small strain shear modulus, $G_{max}$ [MPa]		
0	104.8	103.6	0	0.03	0.0950	900	105.5	21.7		
10	129.4	103.6	0	3.7	0.0913	740	123.4	29.7		
20	129.4	103.5	0	3.98	0.0910	690	131.9	33.9		
40	129.5	103.5	0	4.22	0.0908	660	137.5	36.9		
60	129.4	103.4	0	4.32	0.0907	640	141.7	39.1		
120	129.4	103.4	0	4.44	0.0906	620	146.1	41.6		
780	129.2	103.2	0	4.58	0.0904	590	153.3	45.8		
1440	128.8	102.8	0	4.59	0.0904	580	155.9	47.4		
<b>SHEAR TEST</b>										
Time past start of shear test [min]	Vertical stress, $\sigma_y$ [kPa]	Horizontal stress, $\sigma_x$ [kPa]	Pore sure, $u$ [kPa]	Deformation, $\Delta L$ [mm]	Shear wave travel distance, $l_s$ [m]	Shear wave travel time, $t_s$ [ $\mu$ s]	Shear wave velocity, $v_s$ [m/s]	Small strain shear modulus, $G_{max}$ [MPa]		
0	128.8	102.8	0	4.59	0.0904	580	155.9	47.4		
30	191.5	102.7	32.5	6.09	0.0889	640	138.9	37.6		
60	197.3	102.7	51.7	7.59	0.0874	680	128.5	32.2		
90	201.0	102.7	59.4	9.09	0.0859	700	122.7	29.4		
120	208.9	102.6	62.1	10.59	0.0844	700	120.6	28.4		
150	217.1	102.6	62.4	12.09	0.0829	700	118.4	27.4		
180	225.2	102.6	61.3	13.59	0.0814	690	118.0	27.1		
240	233.8	102.5	59.6	15.09	0.0799	680	117.5	26.9		
300	242.1	102.5	57.5	16.60	0.0784	670	117.0	26.7		
360	245.1	102.5	55.4	18.10	0.0769	660	116.5	26.5		
420	251.8	102.5	53.2	19.60	0.0754	650	116.0	26.2		

## 8.1. RESULTS OF BENDER ELEMENT TESTING

**Table 8.4:** Numerical results of the bender element test performed on Tiller clay.

CONSOLIDATION											
Time past start of consolidation [min]	Time past start of consolidation [h]	Vertical stress, $\sigma_y$ [kPa]	Horizontal stress, $\sigma_x$ [kPa]	Pore pressure, $u$ [kPa]	Deformation, $\Delta L$ [mm]	Shear wave travel distance, $L_s$ [m]	Shear wave travel time, $t_s$ [ $\mu$ s]	Shear wave velocity, $v_s$ [m/s]	Small strain shear modulus, $G_{max}$ [MPa]		
1		63	63	1	0.3	0.0947	2370	40.0	3.0		
3		63	63	1	1.0	0.0940	1090	86.2	14.1		
5		62	62	1	1.7	0.0933	1040	89.7	15.3		
8		67	65	1	2.7	0.0923	990	93.3	16.5		
11		70	65	1	3.3	0.0917	940	97.6	18.1		
14		74	65	1	4.0	0.0910	920	98.9	18.6		
17		80	64	1	5.0	0.900	900	100.0	19.0		
20		94	64	1	5.1	0.0899	870	103.3	20.3		
60	1	94	64	1	5.2	0.0898	820	109.5	22.8		
120	2	94	64	1	5.2	0.0898	800	112.2	23.9		
480	8	95	65	1	5.2	0.0898	780	115.1	25.2		
780	13	95	65	1	5.2	0.0898	770	116.6	25.8		
2400	40	95	65	1	5.3	0.0897	760	118.1	26.5		
2514	41.9	124	87	1	5.3	0.0897	760	118.0	26.5		
2517	41.95	124	87	1	5.3	0.0897	750	119.6	27.2		
2541	42.35	124	87	1	5.3	0.0897	740	121.2	27.9		
2655	44.25	124	87	1	5.4	0.0896	730	122.8	28.7		
3300	55	124	87	1	5.4	0.0896	720	124.5	29.4		
3900	65	125	87	1	5.4	0.0896	710	126.2	30.3		
6000	100	124	87	1	5.4	0.0896	710	126.2	30.2		

SHEAR TEST											
Time past start of shear test [min]	Time past start of shear test [h]	Vertical stress, $\sigma_y$ [kPa]	Horizontal stress, $\sigma_x$ [kPa]	Pore pressure, $u$ [kPa]	Deformation, $\Delta L$ [mm]	Shear wave travel distance, $L_s$ [m]	Shear wave travel time, $t_s$ [ $\mu$ s]	Shear wave velocity, $v_s$ [m/s]	Small strain shear modulus, $G_{max}$ [MPa]		
0.2		127	86	1	0.0	0.0896	700	128.0	31.1		
30	0.5	201	86	16	1.5	0.0881	750	117.5	26.2		
60	1	189	86	33	3.0	0.0866	790	109.6	22.8		
90	1.5	178	86	46	4.5	0.0851	830	102.5	20.0		
120	2	170	86	54	6.0	0.0836	880	95.0	17.1		
150	2.5	162	86	58	7.5	0.0821	920	89.2	15.1		
180	3	157	86	61	9.0	0.0806	960	83.9	13.4		
200	3.33	153	86	62	10.0	0.0796	970	82.0	12.8		

**Table 8.5:** Numerical results of the first Bender element test performed on Esp clay. No shear test was performed.

CONSOLIDATION										
Time past start of consolidation [min]	Time past start of consolidation [h]	Vertical stress, $\sigma_v$ [kPa]	Horizontal stress, $\sigma_x$ [kPa]	Pore pressure, $u$ [kPa]	Deformation, $\Delta L$ [mm]	Shear wave travel distance, $l_s$ [m]	Shear wave travel time, $t_s$ [ $\mu$ s]	Shear wave velocity, $v_s$ [m/s]	Small strain shear modulus, $G_{max}$ [MPa]	
3		63	63	0	0.01	0.0950	1295	73.3	10.2	
5		63	63	0	0.02	0.0950	1155	82.2	12.8	
7		63	63	0	0.03	0.0950	1070	88.8	15.0	
10		63	63	0	0.1	0.0949	990	95.8	17.5	
13		63	63	0	0.2	0.0948	945	100.3	19.1	
15		63	63	0	0.3	0.0947	930	101.8	19.7	
18		65	63	0	0.4	0.0946	905	104.5	20.7	
30		72	64	0	1.7	0.0933	865	107.9	22.1	
40		76	64	0	2.4	0.0926	840	110.3	23.1	
50		79	64	0	2.8	0.0922	830	111.1	23.5	
60	1	80	64	0	2.8	0.0922	815	113.1	24.3	
120	2	80	63	0	2.8	0.0922	800	115.2	25.2	
240	4	79	63	0	2.8	0.0922	790	116.7	25.9	
480	8	79	63	0	2.8	0.0922	780	118.1	26.5	
660	11	79	63	0	2.9	0.0921	775	118.9	26.9	
1200	20	80	63	0	2.9	0.0921	770	119.7	27.2	
2340	39	80	63	1	2.9	0.0921	760	121.2	27.9	



Table 8.6: Numerical results of the second bender element test performed on Esp clay.

CONSOLIDATION										
Time past start of consolidation [min]	Time past start of consolidation [h]	Vertical stress, $\sigma_y$ [kPa]	Horizontal stress, $\sigma_x$ [kPa]	Pore pressure, $u$ [kPa]	Deformation, $\Delta L$ [mm]	Shear wave travel distance, $L_s$ [m]	Shear wave travel time, $t_s$ [ $\mu$ s]	Shear wave velocity, $v_s$ [m/s]	Small strain shear modulus, $G_{max}$ [MPa]	
1		64	64	0	0.4	0.0946	2100	45.1	3.9	
2		73	64	0	0.7	0.0943	1480	63.7	7.7	
4		77	64	0	0.9	0.0941	1330	70.7	9.5	
6		80	64	0	1.0	0.0940	1215	77.3	11.4	
8		80	64	0	1.1	0.0939	1135	82.7	13.7	
10		80	64	0	1.1	0.0939	1075	87.3	14.5	
12		80	64	0	1.1	0.0939	1025	91.6	15.9	
14		80	64	0	1.2	0.0938	1000	93.4	16.7	
16		80	64	0	1.2	0.0939	965	97.2	18.0	
18		80	64	0	1.2	0.0938	940	99.8	18.9	
20		80	64	0	1.2	0.0938	915	102.5	20.0	
30		80	64	0	1.3	0.0937	855	109.6	22.8	
40		80	64	0	1.3	0.0937	825	113.6	24.5	
60	1	80	64	0	1.3	0.0937	805	116.4	25.7	
120	2	80	64	1	1.3	0.0937	785	119.3	27.0	
240	4	80	64	1	1.3	0.0937	775	120.8	27.7	
360	6	80	64	1	1.4	0.0936	770	121.6	28.1	
5700	95	78	64	1	1.4	0.0936	745	125.6	30.0	

SHEAR TEST										
Time past start of shear test [min]	Time past start of shear test [h]	Vertical stress, $\sigma_y$ [kPa]	Horizontal stress, $\sigma_x$ [kPa]	Pore pressure, $u$ [kPa]	Deformation, $\Delta L$ [mm]	Shear wave travel distance, $L_s$ [m]	Shear wave travel time, $t_s$ [ $\mu$ s]	Shear wave velocity, $v_s$ [m/s]	Small strain shear modulus, $G_{max}$ [MPa]	
0		79	64	1	0.0	0.0936	745	125.6	30.0	
30	0.5	140	64	11	1.5	0.0921	785	117.3	26.2	
60	1	129	64	22	3.0	0.0906	840	107.9	22.1	
90	1.5	122	64	31	4.5	0.0891	895	99.6	18.8	
120	2	118	64	38	6.0	0.0876	945	92.7	16.3	
150	2.5	113	64	43	7.5	0.0861	1000	86.1	14.1	
180	3.0	108	64	46	9.0	0.0846	1035	81.7	12.7	
200	3.33	107	64	47	10.0	0.0836	1055	79.2	11.9	

**Table 8.7:** Numerical results of bender element test performed on an Esp sample with height 5 cm.

CONSOLIDATION									
Time past start of consolidation [min]	Time past start of consolidation [h]	Vertical stress, $\sigma_v$ [kPa]	Horizontal stress, $\sigma_x$ [kPa]	Pore pressure, $u$ [kPa]	Deformation, $\Delta L$ [mm]	Shear wave travel distance, $l_s$ [m]	Shear wave travel time, $t_s$ [ $\mu$ s]	Shear wave velocity, $v_s$ [m/s]	Small strain shear modulus, $G_{max}$ [MPa]
1		64	64	0	0.3	0.0447	1255	35.6	2.4
3		66	64	0	0.4	0.0445	710	62.7	7.5
5		70	64	0	0.6	0.0444	610	72.8	10.1
7		75	64	0	0.7	0.0443	530	83.5	13.3
9		79	64	0	0.8	0.0442	500	88.5	14.9
20		80	64	0	0.9	0.0441	465	94.8	17.1
60	1	80	64	0	1.0	0.0440	440	100.1	19.0
120	2	80	64	0	1.0	0.0440	435	101.2	19.5
540	9	79	63	0	1.0	0.0440	420	104.7	20.8
750	12.5	79	63	0	1.02	0.0440	420	104.7	20.8

## 8.2 Empirical determination of $G_{max}$

For comparison to laboratory results, hand calculations of  $G_{max}$  are performed using the relation given in equation (3.6) (discussed in section 3.3).

Parameters used for empirical determination of  $G_{max}$  are presented in Table 8.8.

A thorough description of choice of parameters and performance of calculations is presented in Appendix D.

$G_{max}$  is calculated on the basis of two different functions of the void ratio, given in equations (3.11) and (3.12). An estimated  $G_{max}$  is taken as the average value of these. Empirical results are presented together with laboratory results in Table 8.1.

**Table 8.8:** *Parameters used for empirical determination of  $G_{max}$ .*

Test	OCR	$k$	$P_a$ [kPa]	$n$	$\sigma'_m$ [kPa]	$I_p$ [%]	$e$	$F_1(e)$	$F_2(e)$
Stjørdal 1	2	0.16	100	0.5	92	18	0.904	1.147	1.034
Stjørdal 2	1.7	0.16	100	0.5	112.5	18	0.904	1.147	1.140
Tiller	1.8	0.05	100	0.5	74.6	5.5	1.07	0.908	0.916
Esp	2.6	0.2	100	0.5	68.7	24	1.20	0.765	0.789

### 8.3 Results of Cross-Hole Testing

Results of cross-hole testing at Esp, Byneset, are given in Tabel 8.9. Values of  $v_s$  are determined by assessment of shear wave arrivals at accelerometers A1 and A2. Further,  $G_{max}$  is calculated from equation (3.1). The results seem quite consistent, giving average values of  $v_s = 157$  m/s and  $G_{max} = 47$  MPa.

**Table 8.9:** Numerical values of  $v_s$  and  $G_{max}$  resulting from cross-hole testing. Values of  $v_s$  are determined by assessment of shear wave arrivals at accelerometers A1 and A2. An illustration explaining the strike directions is presented in Figure 6.6.

Test number	Strike direction	$v_s$ [m/s]	$G_{max}$ [MPa]
1	Vertical	158	47
2	Normal, right	161	49
3	Normal, left	159	50
4	Parallel, with	158	47
5	Parallel, against	154	45
6	Parallel, against	154	45
7	Parallel, with	154	45
8	Normal, left	157	47

Figure 8.1 shows received signals from test number 4. Response in the y-direction gave the clearest plot, hence only this is presented. Also, only the time range relevant for determination of  $v_s$  is included. The total range of received signals of this particular test is given in Figure E.8, Appendix E. Due to the amount and similarities of results, plots of received signals of all tests are given in Appendix E. This is nevertheless, an equally important part of the thesis.

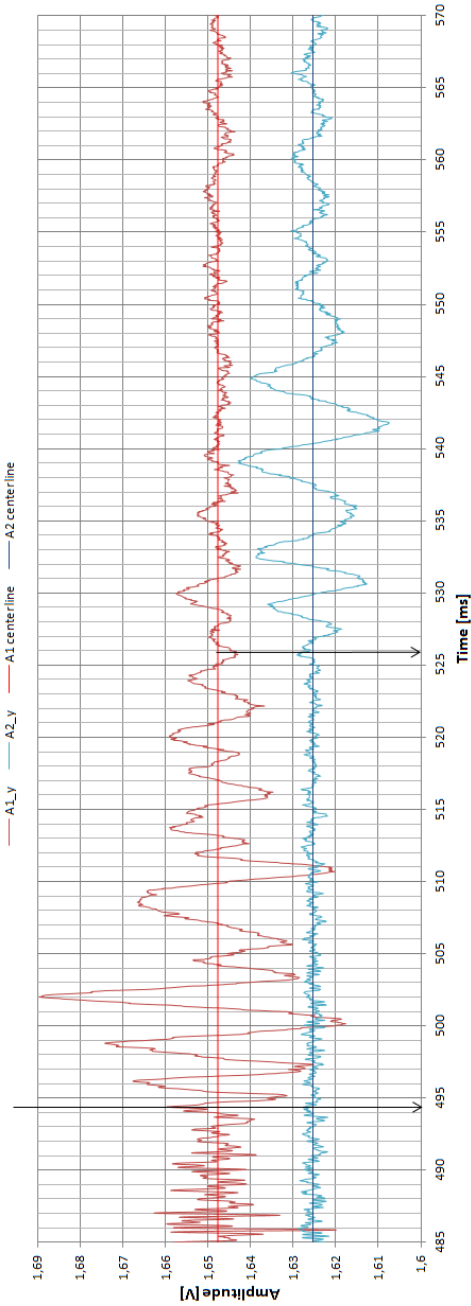


**Figure 8.1:** Close-up of received signals from cross-hole test number 4, showing the range relevant for determination of  $v_s$ . The software used for registration of the signals do not register the time of load application. Hence, the time axis does not start at zero, but is a random time interval where signals were registered. Since only the difference in s-wave arrival times at A1 and A2 is of interest for determination of  $v_s$ , an adjustment putting  $t=0$  at the time of loading is not important.



## Chapter 9

# Discussion of Cross-Hole Test Results

This chapter includes a discussion of the cross-hole test performed at the Esp site. Difficulties regarding the performance and interpretation of the test which may have resulted in erroneous measurements are presented. Approaches for identification of the s-wave and determination of  $v_s$  are discussed. For assessment, results are compared to characteristic values presented in literature.

### 9.1 Sources of Error

#### 9.1.1 Response of Accelerometers

Before starting the test, the plastic tubes with A1 and A2 were given a hammer blow to check the response of the accelerometers. A1 showed good response, giving a plot with evident amplitude fluctuation. A2 however, barely registered any received signal. Applying vibrations at the ground surface next to the tube also showed a much weaker signal at A2

than expected. The strike of a sledge hammer on the steel rod gave better response of A2 than a strike directly on the tube in which A2 was placed. None of the participants in this field investigation could come up with a good explanation for this. Nevertheless, both accelerometers showed response considered to be sufficient, thus the test was continued as planned.

The first impact used as energy source was a vertical hammer blow on top of the steel rod, which was expected to give evident amplitude fluctuations in the z-direction (vertical). However, this turned out not to be the case. An explanation for this unexpected response could be a high attenuation effect of the plastic tubes. It seems reasonable that an attenuation effect of the tube would be greater in the z-direction than in the x- and y-direction. As stated in section 3.2.6, the accelerometers should preferably be in direct contact with the soil for good representation of the actual soil behavior. This would require some work in adjusting the equipment.

After some experimentation, horizontal strikes turned out to give the best response for interpretation, with plots showing an evident fluctuation in the received signals.

### **9.1.2 Determination of S-Wave Travel Time and Distance**

The only input values for determination of shear wave velocity is the distance and travel time from A1 to A2. The distance between the accelerometers was measured with measuring tape, hence millimeter-level accuracy can not be expected. Also, the distance at 8 m depth must be assumed to differ from the distance measured at the ground surface, due to inclination of the plastic tubes. This was taken into account by measuring the inclination of the tubes for determination of the position of the accelerometers at the bottom. (Explained in detail in section 6.4). However, the accuracy is still at centimeter-level, at best.

The shear wave arrival time is determined by subjective interpretation. The precise arrival of the shear wave may be difficult to identify, hence



assessments regarding this may be inconsistent among test operators. Due to this, one should be careful when comparing results, and several tests should be performed to substantiate measured values.

### 9.1.3 Wave Propagation

The impact of a hammer blow on the steel rod will cause deformation of the rod which leads to particle motion in the soil. When determining  $v_s$  from the cross-hole tests performed, a perfectly horizontal travel path at 8 m depth is assumed. In reality, a much more complex environment of wave propagation is present. Both p- and s-waves are induced in the soil with a hemispherical wavefront. The wave propagation velocity of steel is about 5000  $m/s$  (Eiksund, 1994), hence waves traveling down through the rod and then horizontally at 8 m depth will probably be the first to reach A1 and A2. Still, these waves may not produce a clean signal, but be disturbed by irregular particle motion present in the soil. For example, horizontally traveling s-waves may be disturbed by p-waves traveling in different directions, crossing the path of the s-wave. An illustration of the situation with body waves traveling in different directions, and reaching the accelerometers from different paths is shown in Figure 9.1. It is impossible to know for certain the exact travel path of the waves registered, and to what degree the signal represents a clean s-wave. Consequently, it may be difficult to interpret the received signals, and the velocity determined by assumed s-wave arrivals may not be representative for a perfectly clean s-wave with horizontal travel path.

## 9.2 Determination of S-Wave Travel Time

Different approaches for determination of the shear wave travel time,  $t_s$ , has been tried and evaluated. The  $v_s$  values presented as final results in Table 8.9 are calculated from the travel times determined as the time difference between the first peaks of the assumed s-waves at A1 and A2.

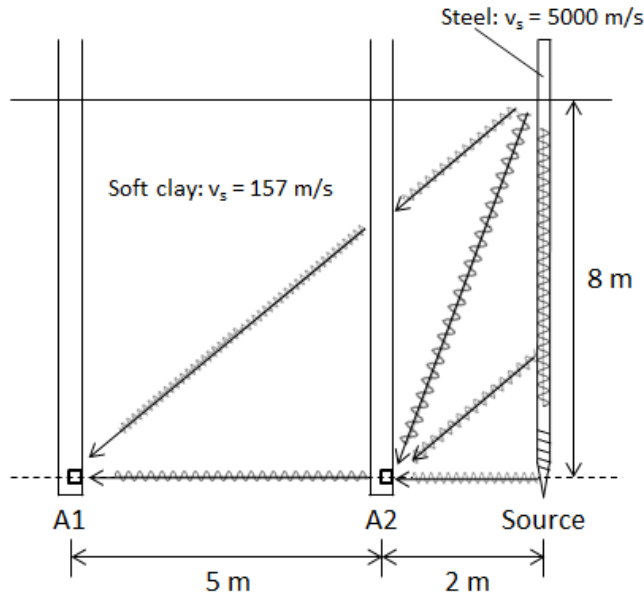


**Figure 9.1:** Illustration of the situation in the ground during cross-hole testing. Body waves propagate with a hemispherical wavefront, reaching the accelerometers with different travel paths, hence causing disturbance of the signals registered during testing.

The results are quite consistent, which may suggest that this is an efficient method of interpretation. However, sometimes it proved difficult to identify the s-wave arrival due to disturbance of the signal. A different way of interpretation and determination of  $t_s$  was then sought.

### 9.2.1 Corresponding Points

It is reasonable to assume that one signal measured at two points A1 and A2 should result in a wave group consisting of the same number of inflection points at both A1 and A2. Consequently, any corresponding points at A1 and A2 should be suitable for determination of time difference. A good assumption would conceivably be that the maximum peak at both

## 9.2. DETERMINATION OF S-WAVE TRAVEL TIME

---

A1 and A2 represents the same point of the wave group. This point is easy to identify and less vulnerable to signal disturbance than the points of first deflection or first peak, and would hence give efficient determination of  $t_s$ .

For illustration, a close-up of signals registered during test 2 is presented in Figure 9.2, showing the similarity of wave forms received by both accelerometers. However, it is observed that from A1 to A2, the period of the wave has increased. Consequently, use of different wave peaks for determination of  $t_s$  would result in different values of  $v_s$ . This observation suggests that the use of freely chosen points for determination of  $t_s$  may not be a good approach. When comparing results from different tests, it must, at least for this particular investigation, be required that  $v_s$  is calculated from travel times determined by the same method of interpretation. With this requirement, the first deflection or first peak seems to be a good choice of corresponding points since it is independent of the appearance of the wave group. It is also assumed that a point related to the first arrival gives the best estimate of the correct shear wave velocity.

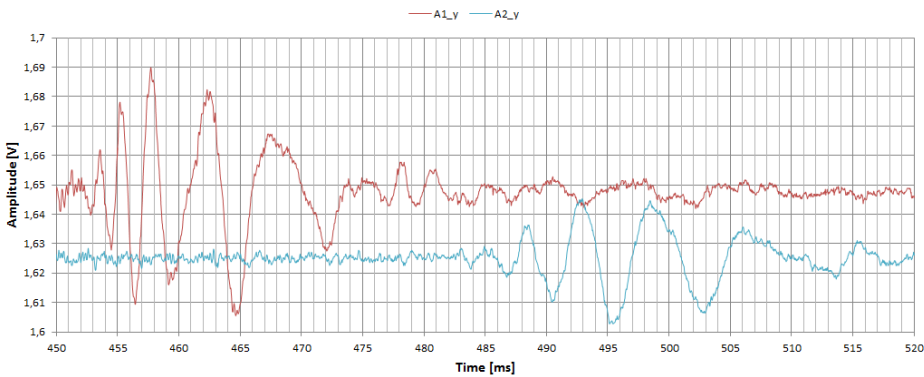


**Figure 9.2:** Close-up of received signals from test 2, showing the similarity in waveform at A1 and A2. Of special interest is the change in frequency observed.

### 9.2.2 Change in Polarity of the S-Wave

As stated in section 3.2.9, hammer blows from opposite directions will produce waves of opposite initial particle motion, hence change the polarity of registered signals. Cross-hole test number 2 and 8 were compared to see whether this phenomenon could be observed. For both tests, the strike of a sledge hammer at the side of the rod, normal to the direction of wave propagation, served as source, but the hammer blow was inflicted at different sides of the rod. The resulting s-waves registered at A1 is shown in Figure 9.3. In this plot,  $v_s = 155$  m/s and the distance between the rod and A1 (2 m) is used for extrapolation of the signals, giving a corresponding starting point in  $t = 0$ , assumed to be at the time of the hammer blow. A clear shift in polarity is observed, indicating that the arrival of the actual s-wave is identified.

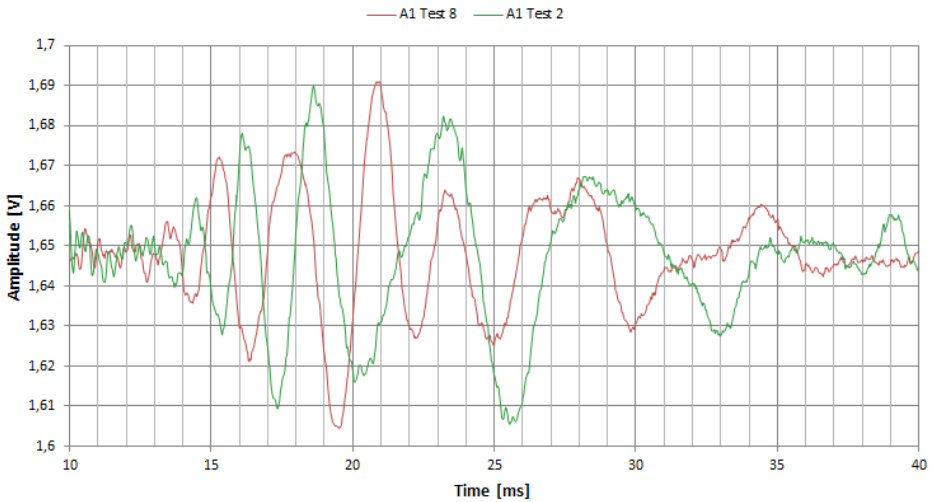


**Figure 9.3:** *Change in polarity of s-waves registered at A1. For test 2 and test 8, the rod was inflicted with horizontal hammer blows of opposite direction.*

The curves in Figure 9.3 correspond well with the example of s-wave traces shown in Figure 3.14 (section 3.2.9). However, the opposite polarity is most evident for the first peaks. After short time, the peaks from the two

## 9.2. DETERMINATION OF S-WAVE TRAVEL TIME

tests do not match equally well. This is likely to be due to differences in the hammer blow, which is inflicted manually by one of the test operators, hence can not be assumed to give perfectly identical signals. The change in frequency which is observed, shown in Figure 9.2, may also partly explain this. Differences in frequency will change the appearance of the wave group, and the change in frequency may not be equal for both tests. The longer the time of propagation, the less evident is the change in polarity. For the signals registered at A2, shown in Figure 9.4, the effect is still present, although the match of peaks is not that obvious.

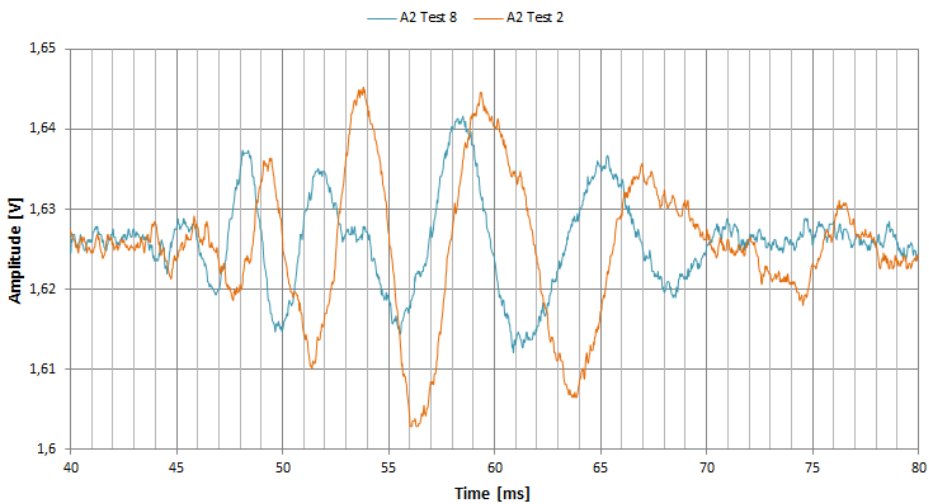


**Figure 9.4:** *Change in polarity of s-waves registered at A2. For test 2 and test 8, the rod was inflicted with horizontal hammer blows of opposite direction.*

Butcher et al. (2005) suggests that the crossover of the wave traces of opposite polarity could be used for determination of arrival times (section 3.2.9). Due to the varying correspondence in signals of test 2 and test 8, this may not be a good method of interpretation of this particular investigation. From Figure 9.4 it is seen that the correct crossover point is difficult to identify from signals registered at A2.

Appendix H presents registered signals for a wider time range than that

shown in Figures 9.3 and 9.4, including s-wave signals registered at both A1 and A2 in the same plot. Also, figures showing the s-wave peaks used for determination of the s-wave travel time, selected on the basis of opposite polarity, are presented.

## 9.3 Assessment of Shear Wave Velocities

### 9.3.1 Consistency of Measured $v_s$ Values

Cross-hole testing was performed with ten different hammer blows serving as source. Received signals of two of the tests showed much disturbance and/or small deflections, with no evident s-wave. For these tests, it was difficult to determine the s-wave arrival, and consequently  $v_s$ . Attempts resulted in values of large divergence compared to the other tests. Due to the difficulty regarding s-wave identification, these results were evaluated as not to be trusted. Hence, they were neglected during further interpretation.

Calculated  $v_s$  of the remaining eight tests are presented in Table 8.9. These results show good consistency, with  $v_s$  values varying from 154 m/s to 161 m/s, giving  $G_{max}$  values varying from 45 MPa to 50 MPa. Such small deviations in the results substantiate the correctness of the measured values.

### 9.3.2 Comparison to Previous Results

The Tiller and Esp sites both consist of soft, sensitive clay. Values of  $G_{max}$  determined by SASW investigations at the Tiller site are presented by Gylland et al. (2013), showing  $G_{max}$  of about 80 MPa at 8 m depth. The plasticity index,  $I_p$ , at the Esp site is found to be significantly larger than at the Tiller site, which would be expected to give higher  $G_{max}$  at the Esp site, according to section 3.3.6. This indicates that cross-hole  $v_s$

values may be somewhat too low. However, it is possible that results from the Esp and Tiller sites are not comparable due to differences in the soil which are not thoroughly examined.

Results from investigations previously performed by Long and Donohue (2007) suggests that  $v_s$  values in the range of 70-300 m/s are characteristic for Norwegian soft marine clay. Also, Subramanian (2008) suggests  $v_s$  values of soft soils in the range 100-200 m/s, with an average value of 150 m/s. According to this, an average value of  $v_s = 157$  m/s resulting from cross-hole testing seems very likely.

Cross-hole investigations performed by Robertson et al. (1986) on soft Drammen clay showed  $v_s \sim 130$  m/s at about 8 m depth. SCPT results from the same site showed  $v_s \sim 165$  m/s. The results of Long and Donohue (2007) from MASW investigations performed on soft Drammen clay, show  $v_s \sim 125$ -130 m/s at about 8 m depth. MASW investigations on soft Onsøy clay, also performed by Long and Donohue (2007), show  $v_s \sim 105$  m/s at about 8 m depth. Measurements from the Esp site give somewhat higher values, but they are still of the same magnitude.

The results of the cross-hole testing performed at the Esp site show significant discrepancy to  $G_{max}$  values measured at the Tiller cite. However, it compares well to characteristic  $v_s$  values of soft marine clay.

#### 9.3.3 Response shown in a Distance-Time Diagram

An alternative approach for assessment of results is used for cross-hole test number 2. Figure 9.5 shows the signals registered at each accelerometer plotted at their respective locations relative to the source. This representation of results allows for determination of wave velocity from the inclination of a straight line through corresponding points of the registered signals. Calculations based on any corresponding points of the wave groups should give the same  $v_s$ . Consequently, lines drawn through any corresponding points should be parallel. This seems to fit well for test

2, although small deviations are difficult to detect with the naked eye. However, the change in period from A1 to A2 observed from close-ups of signals, as discussed in section 9.2.1, suggests that this assessment should be used with care, at least for the results of this particular investigation.

The time of the hammer blow is not registered, hence the location of  $t = 0$  is unknown. However, the line going through the points of first peaks, indicates that  $t \approx 440$  ms represents zero in this test. Due to different amplitudes of the signals, the lines are drawn through points at the centerline representing the peak points of interest, rather than the actual peak. Also, an individual amplification factor is assigned each of the signals, making the wave peaks unsuitable as points of reference for the line.



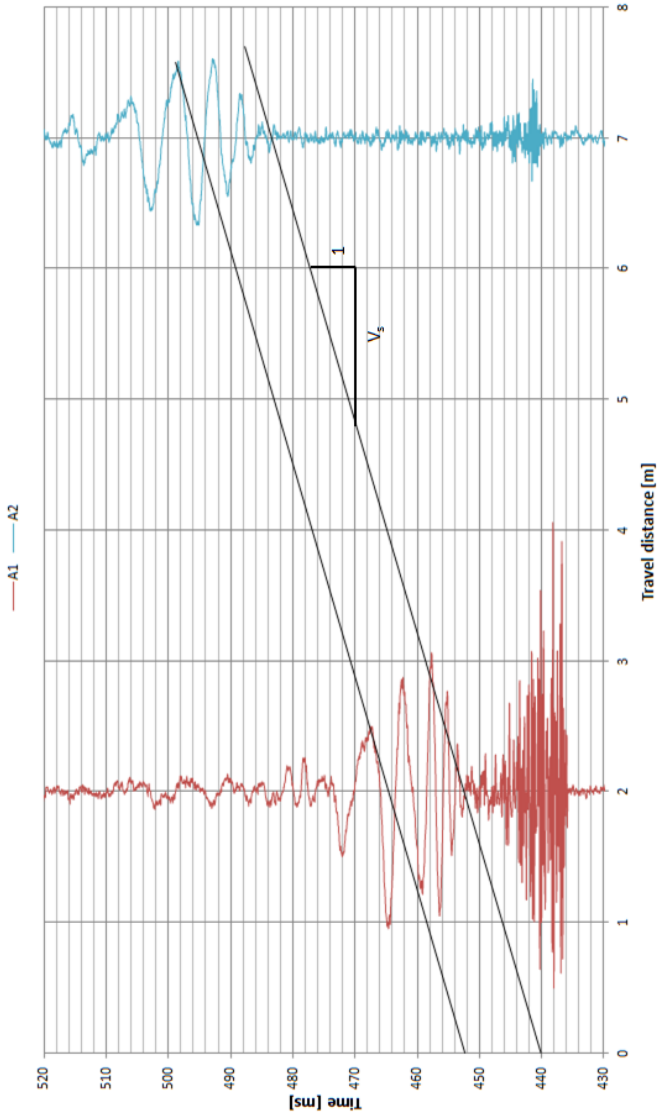


**Figure 9.5:** Results from cross-hole test number 2 presented so that the response registered by the two accelerometers is plotted at their respective locations relative to the source. In a distance-time diagram, velocity can be determined from the inclination of a straight line through corresponding points of the plotted signals.



## Chapter 10

# Discussion of Laboratory Test Results

This chapter includes a discussion of the bender element tests performed. Difficulties regarding the performance and interpretation of the tests which may have resulted in erroneous measurements are presented. For assessment, results are compared to characteristic values presented in literature. Also,  $G_{max}$  is determined from an empirical relationship and from a global stress-strain state of the shear test, and these values are compared to bender element values. The development of  $G_{max}$  with time of consolidation is presented and discussed in context of sample disturbance. Lastly, the results of the test performed on a half-height sample is discussed, with evaluation of near-field effects.

## 10.1 Sources of Error

### 10.1.1 Expelled Pore Water

According to Handbook 014 given by The Norwegian Public Roads Administration (Statens Vegvesen), expelled pore water of 0-5 ml roughly indicates a good experiment. Expelled pore water between 5 ml and 10 ml indicates an acceptable experiment, while a greater amount indicates a poor attempt. During consolidation, the amount of pore water expelled from the samples was registered for evaluation of the quality of the test.

#### The First Stjørdal Test

The total amount of water expelled from the sample during consolidation was 9.5 ml. Consequently, this test can barely be classified as an acceptable experiment. Amount of water being right below the limit of what is classified as a poor attempt, indicates significant disturbance. Hence, the sample quality should not be assumed as optimal.

#### The Second Stjørdal Test

The amount of water expelled from the sample during consolidation to in situ stresses was about 10 ml. Consequently, the quality of the sample used for this test was not very good, and interpretation must be done with this in mind.

#### The Tiller Test

The amount of water expelled from the sample during consolidation to in situ stresses was about 4 ml. This was during a time period of 20 minutes. According to this, the experiment was denoted as good. However, at the end of long-term consolidation (100 h), the amount of expelled water

was about 8 ml. This increase could indicate leakage somewhere in the equipment setup, or the sample could be somewhat more disturbed than what was first assumed.

### **The First Esp Test**

In situ stresses were obtained after about 50 minutes, and expelled pore water at this point was 4.3 ml. After 90 minutes, about 5 ml was expelled, and the total amount of water expelled from the sample after long-term consolidation was 7.2 ml. This indicates a good/acceptable experiment.

### **The Second Esp Test**

About 4 ml of water was expelled quite rapidly during the first 25 minutes of consolidation. Further expulsion was observed at a smaller rate, with 5.7 ml after 6 hours, 8.5 ml after 65 hours and a total of about 10 ml after complete long-term consolidation. This indicates an acceptable experiment.

## **10.1.2 Performance of the Test**

### **The First Stjørdal Test**

When studying the results from the laboratory test, some unexpected behavior was noticed. The consolidation phase had not been fully drained, allowing pore pressure to build up. Control of the triax setup revealed that a clamping screw connecting the drainage tube to the burette had been too tight, giving only a small drainage opening. Very small particles in the water could have been sufficient to clog the drainage tube. It is assumed that this is what happened when pore pressure built up. Since 9.5 ml water expelled from the sample, the tube could not have been completely

clogged during the whole consolidation. Due to the expelled water, no error was suspected during the testing.

Review of the results also revealed adverse behavior during the shear test. The shear test was meant to be undrained, but it appears that the drainage had not been properly closed. Consequently, the problem regarding the drainage tube during consolidation was present also during the shear test. This put the clay sample in a drainage state being something in between of fully drained and undrained. Measured values of  $G_{max}$  will however not be affected in the sense that they are wrong, but they are related to a different drainage state than what was intended. Due to the drainage state, it is difficult to predict how the effective stress state is inside the sample. It could be that the pore pressure in the middle of the sample is greater than the measured values. This would affect the effective mean stress, and hence the shear modulus, which makes it difficult to interpret the results. In situ stresses from equations (7.3) and (7.4) can not be taken as representative for the state of the sample.

More attention should be paid to measurements during testing. This could have revealed errors earlier, making it possible to perform corrections during testing. Especially during the shear test, it is clear that sufficient attention was not given to the test procedure. This would however, probably be different if it was the main part of the study.

## General

There will always be some sources of error related to the test performance. This can be due to disturbance of the sample during preparation, errors in the equipment, such as calibration errors, clogging or leakage, and human errors during the operation of the test. Care has been taken to avoid such errors, however, the possibility of their existence must not be forgotten.

### 10.1.3 Disturbance from Bender Elements

It is conceivable that the installation of bender elements in the samples may cause disturbance to the soil. Chan et al. (2010) investigated the effects of bender element installation in clay samples. The effects of penetration rate, sample height and consolidation pressure were accounted for, showing maximum variation in measured  $v_s$  of 2.5 %, which was taken as negligible. Consequently, it was stated that the installation of bender elements do not cause disturbance to clay samples.

The bender elements could possibly cause some local disturbance when they bend, stirring the clay surrounding the elements. Measured value of  $G_{max}$  will then not be representative for the actual global state of the sample. Further experimentation regarding this may be preferable, for example by adding some salt around the bender elements to maintain the strength of the material. This is however not done during this study.

### 10.1.4 Wave Propagation in the Triaxial Apparatus

The surroundings of the bender element is assumed to consist of somewhat disorderly particle motion when a pulse is applied. A p-wave is generated at each side of the element, one in compression, and the other in rarefaction (section 3.1.2). In front of the bender element, particle movement in opposite directions causes shear, and hence the transmission of a s-wave. It is however, possibly not a perfectly clean s-wave, at least not initially. It is conceivable that effects close to the bender element causes a local area where the s-wave velocity is different from that representative for the global situation.

In a triaxial cell, some of the wave energy will be transferred from the sample to the water surrounding the cell, while some will be reflected at the cell wall. The reflection of waves is assumed to cause a complex environment in the sample, with waves of different particle motion crossing each others paths, possibly causing disturbance of the s-wave. It may also

be that some waves travel along the cell wall.

It is difficult to know the exact behavior of the s-wave, and how it is affected by p-waves. This alone is an issue which requires greater attention, and it has not been emphasized during this study. Hence, interpretation of results are done without this particular knowledge.

### 10.1.5 Near-Field Component

Sanchez-Salinerio et al. (1986) reported the existence of a near-field component, caused by "coupling between waves which exhibit the same particle motion, but propagate at different velocities and attenuate at different rates". This body wave may look like a s-wave, and travel with the velocity of a p-wave, hence it could mask the arrival of the actual s-wave. Also, reversing of the input signal will reverse the polarity of both the s-wave and the near-field body wave component. Consequently, this method should not be used uncritically for determination of the first arrival of the s-wave (Viggiani and Atkinson, 1995).

## 10.2 Assessment of Measured $G_{max}$

$G_{max}$  values measured by bender elements are assessed on the basis of results presented in literature. For the Esp clay, both laboratory and field investigations have been performed during this study, which provides a particularly good basis for assessment. Measured values are also compared to  $G_{max}$  determined from a global stress-strain state of the shear test, and  $G_{max}$  calculated from an empirical relationship.



### 10.2.1 Comparison to Results of Previous Studies

#### Stiff Clays

According to Subramanian (2008), medium stiff to hard clays typically have  $v_s$  values in the range 200-375 m/s, with an average  $v_s = 290$  m/s.

Results of MASW investigations performed by Long and Donohue (2007) gave  $v_s$  in the range 100-350 m/s for firm, Norwegian clays.

Westerlund (1978) performed resonant column testing, and measured  $v_s$  of about 130 m/s after long-term consolidation.

#### The Stjørdal Clay

For firm clays from the Glava and Eberg sites, Long and Donohue (2007) measured  $v_s \sim 320$  m/s at about 12 m depth. After long-term consolidation,  $v_s$  measured by bender elements on the Stjørdal clay show values of about 150 m/s (Table 8.1). This is about 50 % lower than the average value given by Subramanian (2008), and values measured by Long and Donohue (2007) at depth equal to that of the Stjørdal samples.

Measured values are within the range of typical values measured by Long and Donohue (2007), but at the lower limit. Subramanian (2008) ranges typical values somewhat higher than what is measured by Long and Donohue (2007), and bender measurements of the Stjørdal clay lie below this range.

For both the first and second test performed on Stjørdal clay, it is seen that  $v_s$  measured by bender elements are somewhat higher than the values measured by Westerlund (1978).

### Soft Clays

According to investigations previously performed by Long and Donohue (2007), characteristic  $v_s$  values of Norwegian soft marine clays are in the range of about 70-300 m/s. This is quite consistent with Heymann (2003), who states that  $v_s$  values in soft, saturated soils are typically between 100 m/s and 300 m/s. Several results presented by Burns and Mayne (1996) also show typical in situ values of  $v_s$  of clays in the range 50-300 m/s, with predominance in the range 100-200 m/s.

Subramanian (2008) suggests  $v_s$  values of soft soils in the range 100-200 m/s, with an average value of 150 m/s. This upper limit is somewhat lower than that given by Long and Donohue (2007) and Heymann (2003), but is said to apply for "very soft clays".

SCPT and cross-hole testing on soft clay from the Drammen site, Norway, performed by Robertson et al. (1986), gave consistent values of  $v_s$  of about 120 m/s.

Long and Donohue (2007) performed testing on soft marine clay from the Onsøy site, Norway. SASW and MASW investigations gave  $v_s$  of about 100-110 m/s at 8-12 m depth. Bender element testing on unconfined samples from about 10 m depth gave  $v_s \sim 70$  m/s for block samples, while 54 mm tube samples gave  $v_s \sim 50$  m/s.

Investigations performed on a Singapore soft marine clay of medium to low sensitivity has been performed by Tan et al. (2002). Tube samples of 73-75 mm diameter were used for bender element testing in triaxial apparatus. Unconfined compression tests from 16 m depth gave  $G_{max}$  of about 8 MPa, while undrained compression tests on anisotropic consolidated samples from 20 m depth gave  $G_{max}$  of about 25 MPa. SCPT testing gave in situ  $G_{max} \sim 37$  MPa at 16 m depth and  $\sim 30$  MPa at 20 m depth.

### The Tiller and Esp Clays

Both the Tiller clay and the Esp clays are soft, marine clays which are classified as quick (sections 6.2 and 7.4.2). Laboratory testing show similar results, with  $v_s$  of 121-126 m/s, and consequently  $G_{max}$  of 27-30 MPa.

Measured values are well within the range of typical values (Long and Donohue, 2007; Heymann, 2003; Burns and Mayne, 1996), and somewhat lower than the average value given for soft clays by Subramanian (2008).

Gylland et al. (2013) presents results of a SASW survey previously performed at the Tiller site. This shows  $G_{max}$  values increasing from about 25 MPa at 0.5 m to slightly above 100 MPa at about 9 m depth (average  $\rho = 1890 \text{ kg/m}^3$  assumed). These values are in the order of three times as high as those measured by the bender element testing performed on the Tiller clay from 9.1 m depth.

Experience suggests that laboratory measured values should be expected to be somewhat lower than in situ values (section 3.3). The study of Tan et al. (2002) showed  $G_{max}$  measured in laboratory 10-20 % lower than SCPT values, even for samples reconsolidated to in situ stresses. However,  $G_{max}$  of the Tiller clay measured in laboratory is as much as 70 % lower than previously measured in situ values. This large discrepancy give doubt to the accuracy of the results. The block sample used for bender element testing was retrieved in the early autumn, 2013, and was hence stored at the laboratory for about 7 months. This may have caused adverse effects related to sample disturbance. Data from the SASW survey show some scatter due to the use of approximate inversion procedure (Gylland et al., 2013). This is a complicated procedure, giving room for some uncertainties of the in situ values. Nevertheless, the discrepancy in laboratory and field results are larger than expected, hence care should be taken in stating the actual value of  $G_{max}$ .

For the Esp clay,  $G_{max}$  measured on the second sample at the end of consolidation to in situ stresses, is only half the value measured at the same

time during the first test. This may indicate that the second sample was somewhat more disturbed, possibly due to storage for one week longer than the first sample. However, both bender element tests performed show  $v_s$  values somewhat over 120 m/s at the end of long-term consolidation. The consistency in results substantiates their accuracy, and suggests successful experiments.

The results are similar to values measured in situ on Norwegian soft marine clays during previous studies (Robertson et al., 1986; Long and Donohue, 2007). It is however, not expected to obtain in situ values by laboratory testing, thus the actual  $G_{max}$  is assumed to be somewhat higher. Donohue and Long (2010) performed bender element testing on block samples, giving  $v_s \sim 70$  m/s. However, measurements were done on unconfined samples, and is hence not a good basis for comparison. Discussion and literature presented in section 3.3, suggests that reconsolidation will increase the value of  $G_{max}$  to some extent, bringing it closer to its in situ state. It may seem that  $v_s$  measured on both the Esp and Tiller clay lie somewhat in between values representative for unconfined samples and in situ state, which is in accordance with expectations.

### 10.2.2 Comparison to Field Measured $G_{max}$ of the Esp Clay

Results of cross-hole testing on Esp clay showed in situ  $v_s$  in the range of 154-161 m/s, with an average value of 157 m/s. Corresponding values of  $G_{max}$  vary from 45 MPa to 50 MPa, with an average value of 47 MPa.  $V_s$  measured by bender elements on anisotropic consolidated block samples is about 22 % lower than values measured in the field. A discrepancy of this magnitude is quite consistent with the results of Tan et al. (2002).

Bender element testing on unconfined block samples performed in the field by Landon et al. (2007), showed  $v_s$  values being 20-30 % lower than those measured by SCPTU testing at the same site (section 4.2.1). Transportation of the Esp sample to the laboratory may have caused additional disturbance which was not an issue for the investigation of Landon et al.

(2007). Nevertheless, due to the stress dependence of  $G_{max}$ , it would be reasonable to expect values of consolidated samples being somewhat closer to the in situ value than that of unconfined samples. It is conceivable that the clays are unsuitable for direct comparison due to differences in parameters and structure. However, the results of the Esp clay indicate that reconsolidation to in situ stresses does not fully recover the sample.

Even though the Esp samples were consolidated anisotropic to in situ stresses, laboratory measured values are significantly lower than those measured in field. This suggests the influence of other important factors, in addition to stress state, on  $G_{max}$ . Literature presented in section 3.3 indicates that one important factor is the soil structure. Even after long-term consolidation, it seems that when taken from the ground, a sample can not be put in a state representative for the accurate in situ conditions. According to Lunne et al. (2006), the samples of highest quality are block samples, giving laboratory results as close to the actual field values as possible. Still, exact values can not be expected, and some degree of sample disturbance should be accounted for when evaluating laboratory test results.

### **Evaluation of Anisotropy in relation to Wave Propagation**

The cross-hole test measures s-waves with horizontal propagation and vertical particle motion. The bender element test however, measures s-waves with vertical propagation and horizontal particle movement. It is conceivable that a direct comparison of the results of the two tests is somewhat incorrect due to different conditions of wave propagation, and possible influence of anisotropy. At least, the issue deserves some attention, and statements should be made with care.

For both the cross-hole and bender element test, the s-wave is considered anisotropic, traveling in a VH-plane, as defined by Sully and Campanella (1995), presented in section 3.3.4. Due to the stress dependency of  $G_{max}$ , it would be reasonable to assume  $v_s$  larger for propagation in the verti-

cal direction, i.e. in the direction of  $\sigma_1$ , than in the horizontal direction ( $\sigma_3$ ). However, Hardin (1978) and Lo Presti et al. (1993) presented contradictory results, showing  $v_s$  larger for propagation in the direction of  $\sigma_3$  (section 3.3.4). It is also stated that  $G_{max}$  depends about equally on principal stresses in the direction of propagation and particle motion (Yu and Richart, 1984; Jamiolkowski et al., 1991; Santagata et al., 2005)(section 3.3.2).

For bender element and cross-hole testing on Esp clay, the issue regarding direction of wave propagation is comparable to that of the investigation performed by Sully and Campanella (1995). The investigation of Sully and Campanella (1995) regarded down-hole testing with vertical wave propagation, and cross-hole testing with horizontal wave propagation, both in a VH-plane. The results showed  $v_{sA}^{DH} > v_{sA}^{CH}$ . Further testing indicated that differences in  $v_s$  was a consequence of structural anisotropy rather than stress anisotropy.

According to these findings, the results of the bender element tests may not be directly compared to the results of the cross-hole testing performed at Esp. If possible differences in  $v_s$  is assumed to be due to structural effects, it can not be stated in which direction of propagation  $v_s$  should be expected to be the highest. A more thorough investigation on the soil structure of the Esp clay would then be required.

### 10.2.3 Comparison to $G_{sec}$ from Shear Test

For all shear tests performed, the initial part of the stress-strain curve is evaluated for comparison of  $G_{max}$  measured by bender elements to  $G_{sec}$ . At shear strains  $< 10^{-5}$ , this value could be taken as  $G_{max}$ . The shear test is thought to cause a global stress-strain state, while the bender elements generate only local, small strains. In Figures 10.1-10.4,  $G_{max}$  determined from the initial part of the stress-strain curve is called  $G_{max,global}$ , and is calculated using the relationship given in equation (2.28).  $G_{max,bender}$  is the value determined by bender element testing on the respective samples,

at the end of long-term consolidation.

### The First Stjørdal Test

The drainage conditions previously discussed in section 10.1.1 is not a problem when comparing  $G_{max,bender}$  to  $G_{max,global}$ . This can be stated because the values are determined from the same sample, consequently all conditions are equal.

The initial part of the stress-strain curve from the first shear test performed on Stjørdal clay is shown in Figure 10.1.  $G_{max,global}$  is found to be 25 MPa, which is somewhat lower than  $G_{max,bender} = 40$  MPa (Table 8.1).

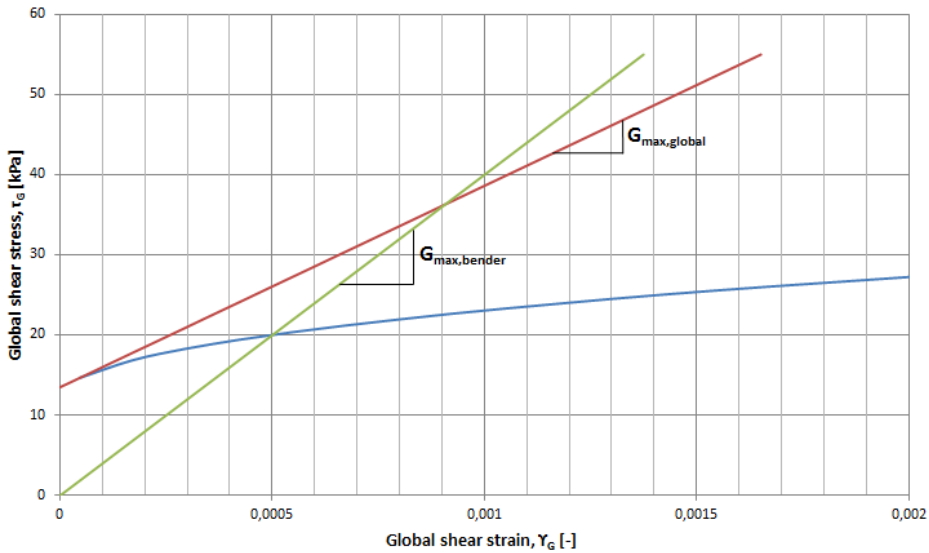


**Figure 10.1:** Initial part of the stress-strain curve from the first shear test performed on Stjørdal clay.  $G_{max,global}$  is  $G_{sec}$  at strains  $< 10^{-5}$ , and  $G_{max,bender}$  is the shear modulus determined by bender elements after long-term consolidation.

### The Second Stjørdal Test

The initial part of the stress-strain curve of the second shear test performed on Stjørdal clay is shown in Figure 10.2.  $G_{max,global}$  is found to be 24 MPa, while  $G_{max,bender} = 47$  MPa (Table 8.1).

It is clear that  $G_{max,global}$  is lower than  $G_{max,bender}$  to about the same extent for both the first and second test performed on Stjørdal clay.

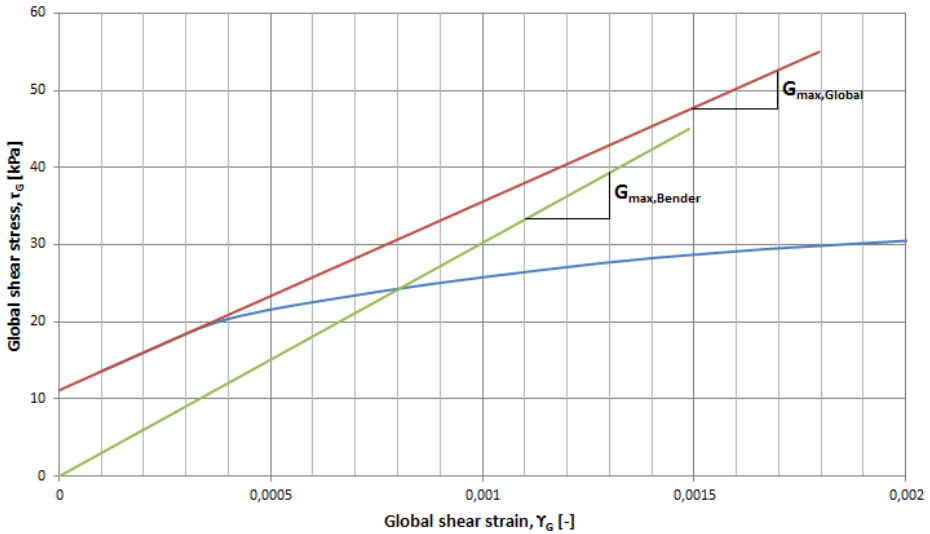


**Figure 10.2:** Initial part of the stress-strain curve from the second shear test performed on Stjørdal clay.  $G_{max,global}$  is  $G_{sec}$  at strains  $< 10^{-5}$ , and  $G_{max,bender}$  is the shear modulus determined by bender elements after long-term consolidation.

### The Tiller Test

The initial part of the stress-strain curve of the shear test performed on Tiller clay is shown in Figure 10.3.  $G_{max,global}$  is found to be 27 MPa, while  $G_{max,bender} = 30$  MPa. Even though  $G_{max,global}$  is still found to be somewhat lower than  $G_{max,bender}$ , the fit is much better for the Tiller clay



than for the Stjørdal clay. This can easily be seen in Figure 10.3 by the red and green lines being almost parallel.

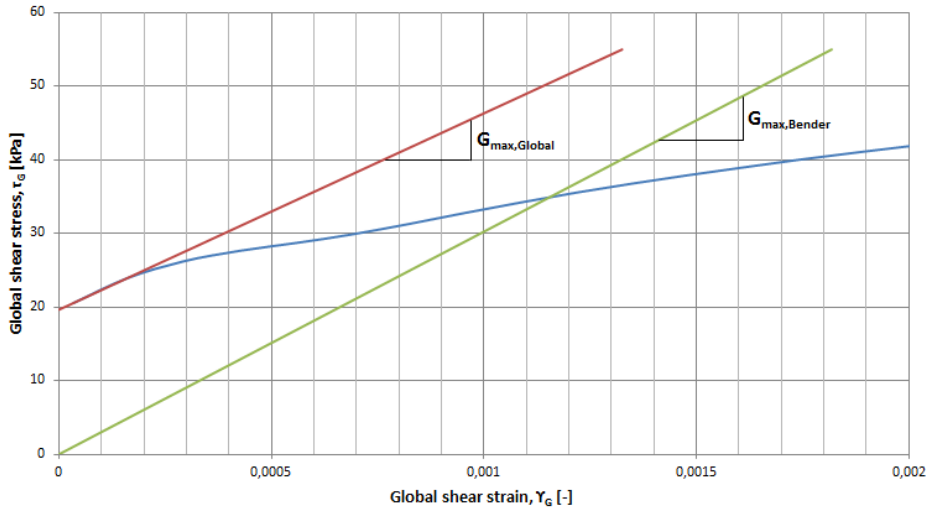


**Figure 10.3:** Initial part of the stress-strain curve from the shear test performed on Tiller clay.  $G_{max,global}$  is  $G_{sec}$  at strains  $< 10^{-5}$ , and  $G_{max,bender}$  is the shear modulus determined by bender elements after long-term consolidation.

### The Second Esp Test

The initial part of the stress-strain curve of the shear test performed on Esp clay is shown in Figure 10.4.  $G_{max,global}$  is found to be 19 MPa, while  $G_{max,bender} = 30$ MPa. As for the Stjørdal clay,  $G_{max}$  determined from the initial part of the shear test is significantly lower than  $G_{max}$  measured by bender elements.

### General Assessment

In general,  $G_{max}$  determined as  $d\tau/d\gamma$  of the initial part of the stress-strain curve of the shear test is seen to be lower than  $G_{max}$  determined by

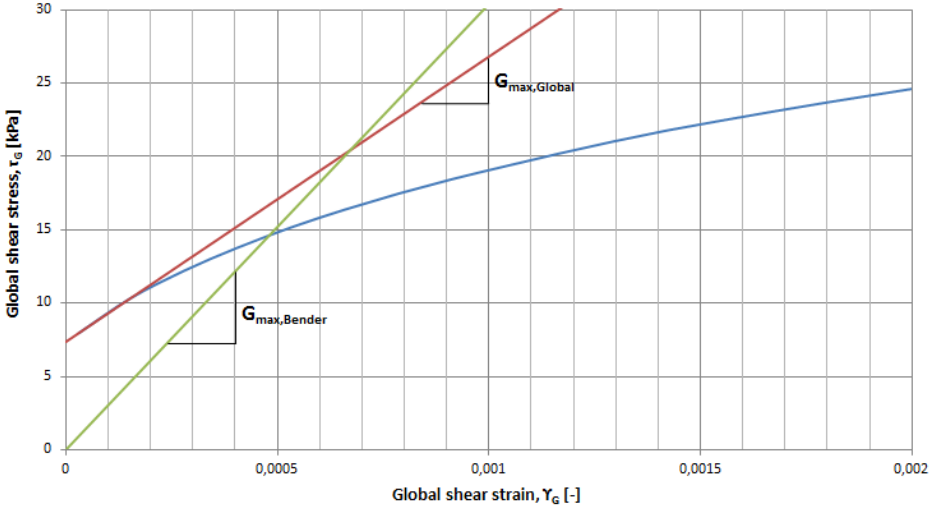


**Figure 10.4:** Initial part of the stress-strain curve from the shear test performed on the second sample of Esp clay.  $G_{max,global}$  is  $G_{sec}$  at strains  $< 10^{-5}$ , and  $G_{max,bender}$  is the shear modulus determined by bender elements at the end of long-term consolidation.

bender element testing. Both for the first Stjørdal test and the Esp test,  $G_{max,global}$  is 37 % lower than  $G_{max,bender}$ . For the second Stjørdal test,  $G_{max,global}$  is as much as 49 % lower, while for the Esp test, it is only 10 % lower than  $G_{max,bender}$ . These results show no consistent trend.

When starting the shear test, complete contact between the sample and the loading system may not be present. This has to be obtained before a consistent relationship between shear stress and shear strain is established. Consequently, initial values of  $\tau$  and  $\gamma$  may not give a good representation of the loading situation. If complete contact is not obtained, it is reasonable to expect a behavior being somewhat softer. This could possibly explain the inconsistency in  $G_{max,global}/G_{max,bender}$ . These results indicate that assessment of  $G_{max}$  from bender element testing by comparison to the value of a global stress-strain relationship is probably not a good approach.

#### 10.2.4 Comparison to Empirical $G_{max}$

The results of all samples show an empirical value of  $G_{max}$  higher than that determined by bender elements (Table 8.1).

It may be that the bender elements cause some local disturbance, stirring the surrounding clay when bending. Measured values of  $G_{max}$  would then not be representative for the global state of the sample, and a softer response would be expected. This possible disturbance is not taken into account in the empirical relationship, hence it could be a cause of discrepancy.

The basis of  $G_{max}$  determination is somewhat different for the bender element test and the empirical relationship. Possible inaccuracies related to the equipment setup is not accounted for in the hand calculations performed. The empirical relationship is only based on soil parameters. This, together with the trend of lower measurements in the laboratory than in the field, suggests that the empirical values give a better estimate of in situ  $G_{max}$ . For the Esp clay, the empirical relationship give  $G_{max}$  about equal to the values measured in the field. This also indicates that the empirical relationship show good agreement with in situ conditions, and that acceptable estimates of  $G_{max}$  may be obtained by simple hand calculations.

However, it may be that the empirical relationship does not fit the conditions of all samples, and assessments regarding this has not been emphasized during this study. It is observed that the empirical values of the Stjørdal clay are almost twice as large as  $G_{max}$  measured by bender elements. For the Tiller and Esp clay, the values are somewhat more similar. This may indicate a trend, suggesting that the empirical relationship which is used has a better fit to soft clays than firm clays. However, the difference between empirical and bender element values is not more than 10 % lower for the soft clays than the firm clays. Also, the test basis provided by this study is considered insufficient for any certain conclusions regarding this.

### 10.3 Effect of Consolidation Time on $G_{max}$

All Bender element tests performed during this study showed an increase in  $G_{max}$  with time of consolidation (Tables 8.1-8.6). To present this observation, plots of measured  $v_s$  with time of consolidation is given. Variation in axial strain,  $\varepsilon_a$ , is included in the same plots for assessment of the correlation between  $v_s$  and  $\varepsilon_a$ .

Variations in  $v_s$  and  $\varepsilon_a$  during the complete long-term consolidation of the Tiller clay sample is shown in Figure 10.5. Figure 10.6 shows a close-up of Figure 10.5, with refined values at the vertical axes for a more detailed view. Similar plots are presented in Figures 10.7 and 10.8, showing the effect of consolidation time on the Esp and Stjørdal clay samples, respectively. The plots in Figures 10.6-10.8 start at the time of consolidation when in situ stresses are obtained.

All graphs shown in Figures 10.5-10.8 are plotted from values selected on the basis of interpretation of results. A more frequent selection of points is made where a relatively high rate of change is observed.

Due to the amount and similarities, plots showing the entire development throughout the long-term consolidation is given in Appendix G. Observations of the second test performed on Esp clay, and a test performed on a sample of half height is also presented here.

A detailed description of the development in  $G_{max}$  is here given for the test performed on Tiller clay (Figures 10.5 and 10.6). During consolidation to in situ stresses,  $G_{max}$  increased to about 20 MPa. A further increase to 25.8 MPa was observed during the next 760 minutes (12 h. 40 min.). Measured  $G_{max}$  then remained approximately constant at 26 MPa for almost 29 hours. At this point, the external vertical load was increased, giving total vertical stress  $\sigma_y = 124$  kPa and total horizontal stress  $\sigma_x = 87$  kPa. This was 2514 minutes (41 h. 54 min.) past start of consolidation. 3 minutes after the extra load was applied, measured  $G_{max}$  was 27.2 MPa. A small increase was observed after another 24 minutes, giving  $G_{max} =$

10.3. EFFECT OF CONSOLIDATION TIME ON  $G_{MAX}$

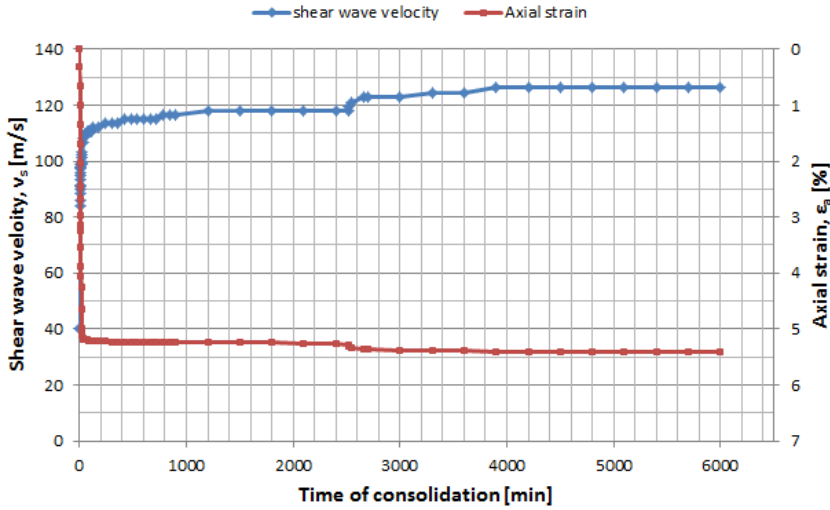


**Figure 10.5:** Variation in shear wave velocity and vertical strain with time of consolidation. The plot presents the results of the bender element test performed on Tiller clay.

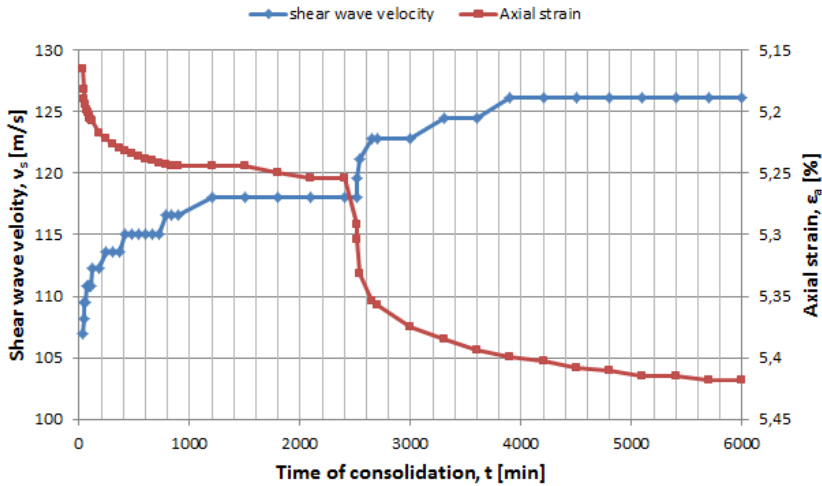


**Figure 10.6:** Close-up of Figure 10.5, for a more detailed view of variations in  $v_s$  and  $\epsilon_a$  of Tiller clay. Initial points are at the time where in situ stresses are obtained.

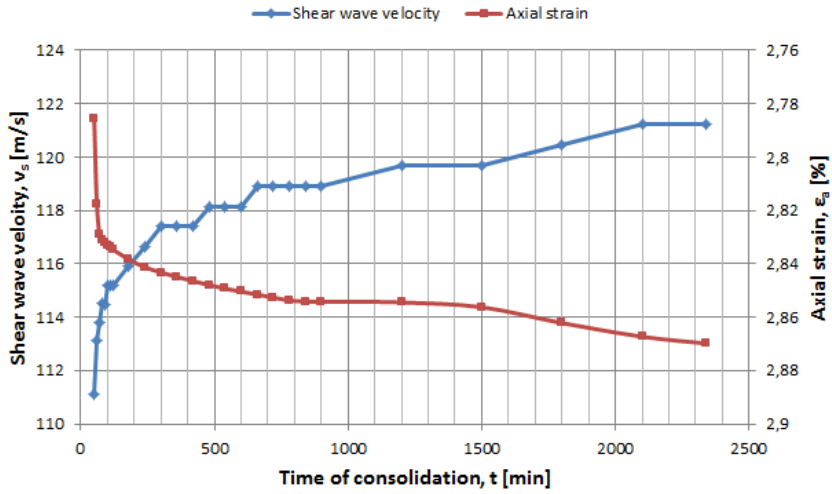


Figure 10.7: Variations in  $v_s$  and  $\epsilon_a$  of Esp clay with time of consolidation, presented with refined values at the vertical axes for a more detailed view. Initial points are at the time where in situ stresses are obtained.

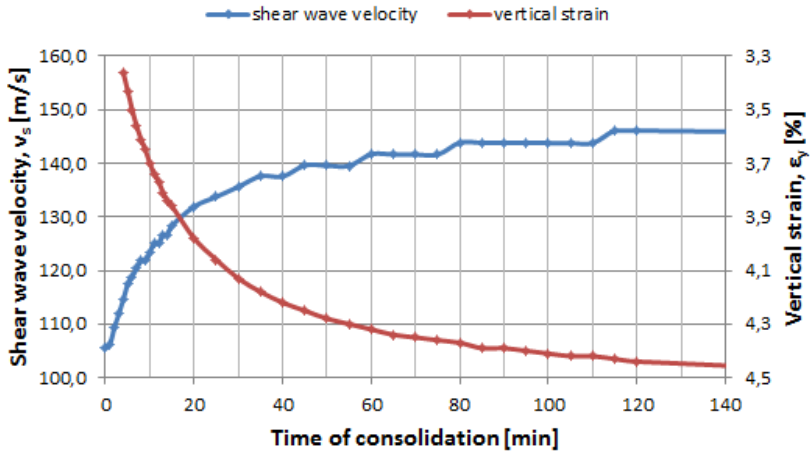


Figure 10.8: Variations in  $v_s$  and  $\epsilon_a$  of Stjørdal clay during the first 140 minutes of consolidation, with refined values at the vertical axes for a more detailed view. Initial points are at the time where in situ stresses are obtained.

27.9 MPa. This value remained constant for almost 2 hours (114 min.) before another small increase was observed,  $G_{max} = 28.7$  MPa. This was 2655 minutes (44 h. 15 min.) past start of consolidation. From this point to about 65 hours (3900 min.) past start of consolidation,  $G_{max}$  increased to about 30 MPa, where it appeared to stabilize. These observations are also presented numerically in Table 8.4.

The increase in  $v_s$ , and consequently  $G_{max}$ , with time of consolidation is evident for all bender element tests performed during this study. This is consistent with the theory discussed in section 3.3. All tests show a relatively large and rapid increase in measured  $v_s$  during the initial consolidation phase, until in situ stresses are obtained. A further increase is then observed, but of a smaller rate. According to section 3.3.5, the secondary increase in  $G_{max}$  is probably related to aging effects.

A clear correlation between increasing  $G_{max}$  and increasing axial strain,  $\varepsilon_a$ , is also shown. This is particularly evident from Figure 10.6.  $\varepsilon_a$  increases due to additional load, and a subsequent increase in  $v_s$  is observed almost immediately. Small strain rate leads to a diminishing increase in  $v_s$ . These observations matches the findings of Westerlund (1978), presented in Appendix G, Figure G.7. Better contact between soil grains due to increasing axial strain followed by a reduction in pore water, may explain the corresponding increase in  $v_s$ .

The development of  $G_{max}$  is very similar for all samples, however measured  $v_s$  values of the Stjørdal clay show a larger increase than the Tiller and Esp clays. After consolidation to in situ stresses, the Tiller and Esp clays both show an increase in  $v_s$  of about 10 m/s after further consolidation for 20 hours. At the same time of consolidation, the increase in measured  $v_s$  of the Stjørdal clay is about four times as large. This may be due to differences in sample quality. Testing on Stjørdal clay was performed on 54 mm tube samples, while for the Tiller and Esp clays, block samples were used. According to literature discussed in section 4.2, block samples are of higher quality than 54 mm tube samples, and is hence expected to give laboratory  $v_s$  values closer to in situ values. Assuming that long-term

consolidation brings  $v_s$  closer to in situ value, high quality samples would consequently be seen to give less increase of  $v_s$ , since the initial value is more correct.

To some extent, it seems that proper reconsolidation has the effect of "fixing" the sample, putting it closer to its in situ state. Consequently,  $v_s$  measured after long-term consolidation can be expected to be the most representative for the actual conditions in field. This also suggests that observations of increasing  $v_s$  may indicate the degree of sample disturbance. High quality samples seem to show less increase in measured  $v_s$  values with time of consolidation than low quality samples. For assessment of sample disturbance,  $v_s$  measured in laboratory should be compared to values measured in situ, for example by MASW, SCPT or cross-hole investigations (section 3.2).

### 10.3.1 Representation of In Situ State

It can quite confidently be stated that the soil is affected by secondary effects as aging, which gives an increase in  $v_s$ , and  $G_{max}$ , with time. This is substantiated by the literature presented in section 3.3.5 and observations of test results. Consequently, if  $G_{max}$  determined from laboratory measurements of  $v_s$  should be representative for in situ values, an increase in  $v_s$  due to secondary effects must be accounted for.

According to Santagata and Kang (2006), secondary effects over a geologic period of time may differ from those observed over an engineering time scale, consequently having different influence on soil structure and properties. A soil element in its natural state has often been exposed to sedimentation for several decades. This gives resulting aging effects which are difficult to recreate in the laboratory. It is conceivable that observation of the increase in  $v_s$  over a given time period, could provide the possibility of extrapolation forward in time. Extrapolating laboratory values to the age of the natural deposit would then give a good approximation of the in situ  $G_{max}$ . It is however, unreasonable to assume that an increase in  $v_s$  is



present throughout an infinite period of time. The use of an extrapolation procedure would hence require the assumption of a maximum value of the rate parameter  $N_G$  (section 3.3.5), limiting the increase.

## 10.4 Test on Sample of Half Height

### 10.4.1 Determination of S-Wave Arrival

The results of the bender element test performed on a sample of half height, i.e. 5 cm, show initially very low values of  $v_s$  and a rapid increase during consolidation to in situ stresses (Table 8.7 and Figure 10.10). During the test, received signal looking somewhat different from those of the full-height samples were observed. For the 10 cm samples, received signals showed one evident sine pulse, similar to that transmitted. Only small deflections, were noticeable in front of the pulse, showing no sine waveform. This was hence quite surely assumed not to be the s-wave arrival. For the short sample however, some deflections showing a sine waveform was registered before a waveform of even larger deflection and similarity to the transmitted wave. This is illustrated by a principle drawing given in Figure 10.9. The time difference is determined by a fitting curve using the method of least squares for identification of the received signal which has a waveform approximately equal to that of the transmitted wave. This fitting curve identified the first peak as the s-wave arrival, although the subsequent peak showed even greater similarity to the transmitted signal. Since the fitting curve was seen to give an even better fit if shifted one half wavelength, it was polarized to measure the time difference for this situation. The time difference corresponding to the shifted fitting curve is denoted  $\Delta t_{polarized}$  in Figure 10.9. Longer travel time consequently gave lower values of  $v_s$ . Measured  $v_s$  with time of consolidation is shown in Figure 10.10, where values measured for the polarized fitting curve is marked with red dots. These  $v_s$  values are so low (40-50 m/s) that it was considered very unlikely that they represent the actual shear wave velocity. The

fitting curve was thus switched back, measuring  $v_s$  corresponding to the time difference denoted as  $\Delta t$  in Figure 10.9. It is conceivable that this nevertheless was the correct identification of the s-wave arrival.

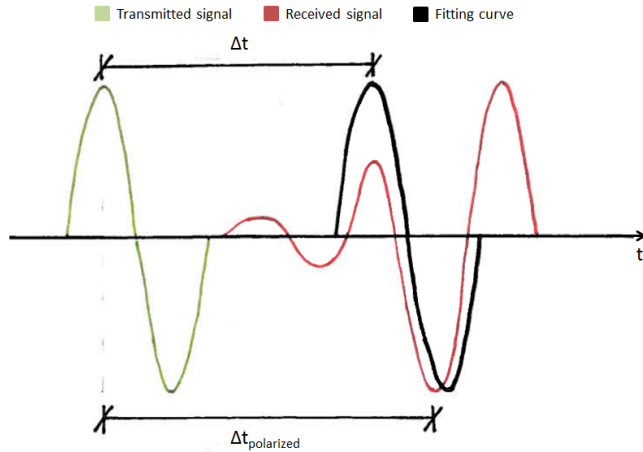


**Figure 10.9:** Principle drawing of signal for the bender element test performed on a short sample of Esp clay. The sketch is not made in scale.

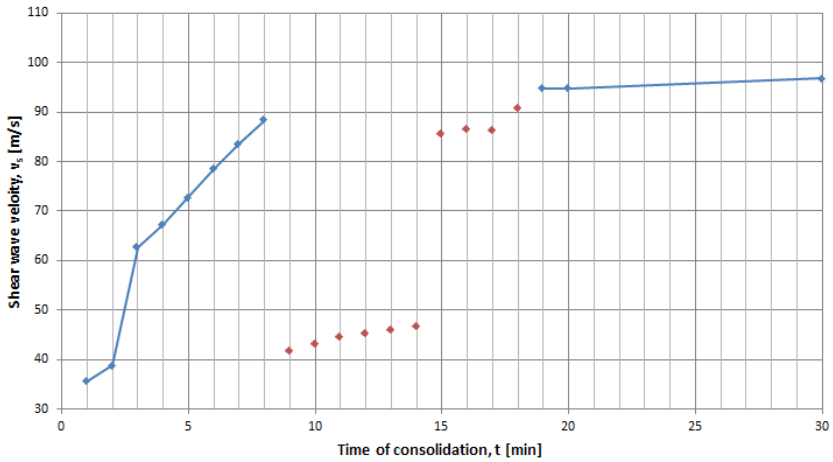


**Figure 10.10:** Variation in shear wave velocity and vertical strain with time of consolidation for a sample of Esp clay with height 5 cm.

### 10.4.2 Near-Field Component

Sanchez-Salineró et al. (1986) stated that the first arrival of body waves may not represent the shear wave arrival, but the arrival of a near-field component. It was suggested that this near-field component is a result of coupling between waves of equal particle motion but different propagation velocities. This wave would have a waveform similar to the s-wave, and travel with the velocity of a p-wave. This phenomenon is also discussed by Viggiani and Atkinson (1995), who states that this is particularly relevant when "the distance between the source and receiver is in the range  $\frac{1}{4} - 4$  wavelengths". These findings give reason to wonder if the peak initially identified as the s-wave arrival is the response of a near-field component rather than the actual s-wave. If this was the case, it would be reasonable to believe that the actual s-wave was that corresponding to a fitting curve switched one half, or one whole wavelength, giving larger  $\Delta t$ . However, compared to  $v_s$  measured on full-height samples ( $\sim 120$  m/s),  $v_s$  corresponding to  $\Delta t_{polarized}$  are far too low, hence not trusted. Values corresponding to  $\Delta t$  seem much more reasonable, and are consequently assumed to be the most reliable. If a near-field component as that described by Sanchez-Salineró et al. (1986) was present, this could possibly explain the deflections observed in front of the first peak of the assumed s-wave.

A question of interest is why the received signal shows a first peak before a subsequent peak of greater similarity to the transmitted signal, while for a full-height sample, only one evident peak is registered.

### 10.4.3 Comparison of $v_s$ of Half- and Full-Height Samples

The two bender element tests of Esp clay performed on full-height samples gave  $v_s$  of 121-125 m/s after long-term consolidation. The same test performed on a half-height sample gave  $v_s = 105$  m/s after long-term consolidation, which is almost 20 % lower. This may suggest the existence

of some local effects close to the bender elements giving a lower velocity in this area. For a shorter sample, the local environment would account for a larger part of the total travel distance, consequently giving lower  $v_s$  values than a sample of double height. The pulse applied to the bender element causes a complex mix of particle motion. Bending of the element generates p-waves at the sides. It is difficult to tell the exact situation of particle movement in front of the element, but it is reasonable to assume that it is not the transmission of a perfectly "clean" s-wave. A s-wave not subjected to any disturbance due to bender elements or reflections of other waves, might show a velocity different from that measured during this test.

#### 10.4.4 Development in $v_s$ with Time of Consolidation

Although  $v_s$  measured at the end of long-term consolidation is lower for the shorter sample, the development in  $v_s$  with is about the same as for the full-height samples. This illustrates the same repairing effect as that observed from the other tests, as well as from previous studies. Due to similarity to the results of the full-height samples presented in section 10.3, a plot showing  $v_s$  variation with time of consolidation for the short sample is presented in Appendix G, Figure G.6.

# Chapter 11

## Observations and Further Work

### 11.1 Summary of Test Observations

Both bender element and cross-hole testing performed during this study have shown to give reasonable results.

Cross-hole testing performed at Esp, Byneset, gave consistent measurements with an average  $v_s$  of 157 m/s, and average  $G_{max}$  of 47 MPa. These results show quite good correspondence to values reported in literature, being well within the range of characteristic values for Norwegian clays. One significant discrepancy is observed when comparing  $v_s$  measured at the Esp site to values previously measured at the Tiller site.

It is stated that  $G_{max}$  measured by bender elements is lower than in situ  $G_{max}$ . Even for high quality block samples consolidated to in situ stress state, field values are not obtained in the laboratory. The soil structure is assumed to be one important factor which can not easily be controlled.

Bender element testing on a clay sample of half height (5 cm) showed  $v_s$

values somewhat lower than those measured on the full-height samples. This suggests the existence of some near-field effects influencing  $v_s$  close to the elements.

Measurements during long-term consolidation showed an evident increase in  $v_s$  with time. Observations also showed a larger increase for 54 mm tube samples than for block samples, indicating some correlation between sample disturbance and  $G_{max}$ .

Interpretation of cross-hole results revealed some difficulties regarding determination of  $v_s$ . Some uncertainties regarding the laboratory equipment may also be present.

## 11.2 Further Work

One of the difficulties experienced during this study, was uncertainties regarding the behavior of the body waves in the triaxial apparatus. It is assumed that the propagation of both p- and s-waves within the boundaries of the triaxial cell causes a complex environment. Lack of knowledge regarding this may have caused some gaps in the interpretation of results. Development of a model of the bender element test in a finite element method program, such as Plaxis, could possibly illuminate this issue, and provide results valuable for comparison and assessment of reliability.

A further study on the effect of anisotropy on  $v_s$  may also be of interest. Here, previous literature have shown contradictory results. Greater knowledge regarding this would give a better basis for comparison of field and laboratory tests where waves propagate in different directions. A thorough study on the effect of soil structure could preferably be related to this issue, since literature suggests that the influence of structural anisotropy on  $G_{max}$  may be equally important as stress anisotropy.

The equipment used for cross-hole testing during this study should be further developed so that the accelerometers are in direct contact with

the soil. This would probably result in a more evident response, giving a basis for simpler and more accurate interpretation. Registration of the hammer blow, giving an accurate time of zero, would also improve the setup.

Some uncertainties has been pointed out during this study regarding the propagation of waves generated when using a hammer blow on a steel rod as source for cross-hole testing. A thorough study on this, with emphasis on the travel path of the waves registered by the receivers could further ensure the reliability of results. An optimization of distance between receivers and source may be of interest.

A more thorough investigation regarding the development of  $G_{max}$  with time of consolidation, may give answers to the applicability of  $G_{max}$  as a measure of sample disturbance. A categorization of sample quality based on  $v_s$  measurements is already proposed in literature. Further testing could possibly substantiate this categorization, establishing the method as a conventional approach.





# Bibliography

- Amdal, Å. M. W., Dons, M. and Knutsen, M. (2012), Prosjekt Stjørdal. Project thesis in the course TBA 4110 Geoteknikk felt/lab, NTNU. (In Norwegian).
- Burland, J. B. (1990), ‘On the compressibility and shear strength of natural clays’, *Géotechnique* **40**(3).
- Burns, S. E. and Mayne, P. W. (1996), ‘Small- and high-strain measurements of in situ soil properties using the seismic cone penetrometer’, *Transportation Research Record: Journal of the Transportation Research Board* **1548**(1).
- Butcher, A. P., Campanella, R. G., Kaynia, A. M. and Massarsch, K. R. (2005), Seismic cone downhole procedure to measure shear wave velocity - a guideline, Technical report, The International Society for Soil Mechanics and Geotechnical Engineering. Report of Technical Committee No 10: Geophysical Testing in Geotechnical Engineering.
- Chan, K. H., Boonyatee, T. and Mitachi, T. (2010), ‘Effect of bender element installation in clay samples’, *Géotechnique* **60**(4).
- Chopra, A. K. (1995), *Dynamics of Structures*, Prentice-Hall, Englewood Cliffs, New Jersey.
- Corps of Engineers (1995), *Geophysical exploration for engineering and environmental investigations*, U.S. Department of the Army, Corps of Engineers, Washington, DC. Engineer Manual 1110-1-1802.

- Donohue, S. and Long, M. (2008), Rapid assessment of offshore and on-shore sample quality, *in* ‘15th Nordic Geotechnical Meeting’, University of Bath.
- Donohue, S. and Long, M. (2009), ‘Suction measurements as indicators of sample quality in soft clay’, *Geotechnical Testing Journal* **32**(3).
- Donohue, S. and Long, M. (2010), ‘Assessment of sample quality in soft clays using shear wave velocity and suction measurements’, *Géotechnique* **60**(11), 883–889.
- Eiksund, G. (2013), ‘Dynamic soil properties’. Lecture in PhD course BA8305 Geodynamics, NTNU.
- Eiksund, G. R. (1994), *Dynamic testing of piles*, NTNU, Norwegian University of Science and Technology.
- EPRI (1993), *Guidelines for determining design basis ground motions*, Vol. 1, Electric Power Research Institute, Palo Alto, California.
- Frost, D. J. and Burns, S. E. (2003), *The Civil Engineering Handbook, Second Edition*, CRC Press, LLC, Boca Raton, Florida. Ch. 27, In Situ Subsurface Characterization.
- GDS Instruments (n.d.), ‘Bender element system’, <http://gdsinstruments.com/gds-products/gds-bender-element-system>.
- Graham, J., Kwok, C. K. and Ambrose, R. W. (1984), ‘Stress release, undrained storage, and reconsolidation in simulated underwater clay’, *Géotechnique* **27**, 279–288.
- Gylland, A., Long, M., Emdal, A. and Sandven, R. (2013), ‘Characterization and engineering properties of tiller clay’, *Engineering Geology* **164**.
- Hardin, B. O. (1978), The nature of stress-strain behavior for soils, *in* ‘Proceedings of the ASCE speciality conference on earthquake engineering and soil dynamics’, pp. 3–90.

- Heymann, G. (2003), 'The seismic cone test', *Journal of the South African Institution of Civil Engineering* **45**(2).
- Hu, L., Ding, J. and Liu, H. (2010), 'Mechanical behavior of marine clay under wave loading', *International Journal of Offshore and Polar Engineering* **20**(1).
- Ibrahim, A., Orense, R. and Pender, M. (2011), 'Determination of very small strain shear modulus of auckland residual soils using bender elements'.
- Ishibashi, I. (1992), 'Discussion to "Effect of soil plasticity on cyclic response", by M. Vucetic and R. Dobry', *Journal of Geotechnical Engineering* **118**(5).
- Jamiolkowski, M., Leroueil, S. and Lo Presti, D. C. F. (1991), Theme lecture: Design parameters from theory to practice, in 'Proceedings of the international conference on geotechnical engineering for coastal development, Geo-Coast 1991', Yokohama, Japan, pp. 877–917.
- Jones, R. (1958), 'In-situ measurement of the dynamic properties of soil by vibration methods', *Géotechnique* **8**(1).
- Kim, T. and Novak, M. (1981), 'Dynamic properties of some cohesive soils of ontario', *Canadian Geotechnical Journal* **18**(3), 371–389.
- King, J. R. (2013), Udrenert skjærkryp i kvikkleire. utvikling av treak-sialrigg og vurdering av esp, byneset, som forsøksfelt, Master's thesis, NTNU, Norwegian University of Science and Technology. (In Norwegian).
- Kirkpatrick, W. M. and Khan, A. J. (1987), 'The reaction of clays to sampling stress relief', *Canadian Geotechnical Journal* **34**(1).
- Kokusho, T., Yoshida, Y. and Esashi, Y. (1982), 'Dynamic properties of soft clay for wide strain rate', *Soils and Foundations* **22**(4).
- Kramer, S. L. (1996), *Geotechnical Earthquake Engineering*.

- Landon, M. M., DeGroot, D. J. and Sheahan, T. C. (2007), 'Nondestructive sample quality assessment of a soft clay using shear wave velocity', *Journal of Geotechnical and Geoenvironmental Engineering* **133**, 424–432.
- Lee, J.-S. and Santamarina, C. (2005), 'Bender elements: Performance and signal interpretation', *Journal of Geotechnical and Geoenvironmental Engineering* **131**(9).
- Lo Presti, D. C. F., Jamiolkowski, M., Lancellotta, R. and Vercelli, L. (1993), 'Maximum shear modulus measurement using bender elements in oedometer tests', *Rivista Italiana di Geotecnica* .
- Long, M. and Donohue, S. (2007), 'In situ shear wave velocity from multichannel analysis of surface waves (masw) tests at eight norwegian research sites', *Canadian Geotechnical Journal* **44**.
- Long, M., Donohue, S. and O'Connor, P. (2008), 'Rapid, cost effective and accurate determination of in situ stiffness using masw at bothkennar', *Ground Engineering* .
- Luna, R. and Jadi, H. (2000), Determination of dynamic soil properties using geophysical methods, *in* 'Proceedings of the First International Conference on the Application of Geophysical and NDT Methodologies to Transportation Facilities and Infrastructure', St. Louis, MO.
- Lunne, T., Berre, T., Andersen, K. H., Strandvik, S. and Sjursen, M. (2006), 'Effects of sample disturbance and consolidation procedures on measured shear strength of soft marine norwegian clays', *Canadian Geotechnical Journal* **43**, 726–750.
- National Instruments (n.d.), 'Labview system design software', <http://sine.ni.com/np/app/main/p/docid/nav-104/lang/no/>.
- NGF (1982), Veiledning for symboler og definisjoner i geoteknikk - presentasjon av geotekniske undersøkelser, Technical report, Norwegian Geotechnical Society (Norsk Geoteknisk Forening). (In Norwegian).

- NGU (2012), Resistivitetsmålinger for løsmassekartlegging ved skredgrop på byneset, sør-trøndelag, Technical Report 2012.004, NGU, Geological Survey of Norway. (In Norwegian).
- NIFS (2012), Datarapport for kvikkleireskredet ved esp i byneset i januar 2012, Technical Report 34/2012, NIFS, Norwegian Water Resources and Energy Directorate in collaboration with the Norwegian Public Roads Administration and the Norwegian National Rail Administration. (In Norwegian).
- Nordal, S. (2013a), Personal conversation.
- Nordal, S. (2013b), ‘Geodynamics’, Norwegian University of Science and Technology (NTNU), Geotechnical Division, Trondheim. Lecture notes: PhD Course BA8305.
- Park, C. B., Miller, R. D. and Xia, J. (1999), ‘Multichannel analysis of surface waves’, *Geophysics* **64**(3).
- Pradhan, T., Tatsuoka, F. and Horii, N. (1988), ‘Simple shear testing on sand in a torsional shear apparatus’, *Soils and Foundations* **28**(2), 95–112.
- Redpath, B. B. (1973), Seismic refraction exploration for engineering site investigations, Technical Report TR E-73-4, U. S. Army Engineer Waterways Experiment Station, Explosive Excavation Research Laboratory.
- Robertson, P. K., Campanella, R. G., Gillespie, D. and Rice, A. (1986), ‘Seismic cpt to measure in situ shear wave velocity’, *Journal of Geotechnical Engineering, ASCE* **112**(8).
- Sanchez-Salinero, I., Roesset, J. M. and Stokoe, K. H. (1986), Analytical studies of body wave propagation and attenuation, Technical report, University of Texas, Austin. Technical report.
- Sandven, R. (2012a), ‘Geotechnics, field and laboratory investigations’,

- Norwegian University of Science and Technology (NTNU), Geotechnical Division, Trondheim. Lecture notes: Part 1, MSc course TBA4110.
- Sandven, R. (2012*b*), ‘Geotechnics, field and laboratory investigations’, Norwegian University of Science and Technology (NTNU), Geotechnical Division, Trondheim. Lecture notes: Part 2, MSc course TBA4110.
- Santagata, M., Germaine, J. T. and Ladd, C. C. (2005), ‘Factors affecting the initial stiffness of cohesive soils’, *Journal of Geotechnical and Geoenvironmental Engineering* **131**(4), 430–441.
- Santagata, M. and Kang, Y. I. (2006), ‘Effects of geologic time on the initial stiffness of clays’, *Engineering geology* **89**(1), 98–111.
- Shibuya, S., Hwang, S. C. and Mitachi, T. (1997), ‘Elastic shear modulus of soft clays from shear wave velocity measurements’, *Géotechnique* **47**(3).
- Shibuya, S. and Mitachi, T. (1994), ‘Small strain shear modulus of clay sedimentation in a state of normal consolidation’, *Soils and foundations* **34**(4), 67–77.
- Shibuya, S. and Tanaka, H. (1996), ‘Estimate of elastic shear modulus in holocene soil deposits’, *Soils and foundations* **36**(4), 45–55.
- Shibuya, S., Tatsuoka, F., Teachavorasinskun, S., Kong, X. J., Abe, F., Kim, Y.-S. and Park, C.-S. (1992), ‘Elastic deformation properties of geomaterials’, *Soils and Foundations* **32**(3).
- Statens Vegvesen (2005), *Laboratorieundersøkelser*, Statens Vegvesen. Håndbok 014 (In Norwegian).
- Subramanian, N. (2008), *Design of Steel Structures*, OUP India. Appendix C, Properties of Soils.
- Sully, J. P. (1991), Measurement of in situ lateral stress during full-displacement penetration tests, PhD thesis, University of British Columbia, Vancouver, B.C., Canada.

- Sully, J. P. and Campanella, R. G. (1992), In situ shear wave velocity determination using seismic cone penetrometer for evaluating soil anisotropy, *in* 'Earthquake Engineering, Proceedings of the Tenth World Conference', Balkema, Rotterdam.
- Sully, J. P. and Campanella, R. G. (1995), 'Evaluation of in situ anisotropy from crosshole and downhole shear wave velocity measurements', *Géotechnique* **45**(2).
- Tan, T.-S., Lee, F.-H., Chong, P.-T. and Tanaka, H. (2002), 'Effect of sampling disturbance on properties of singapore clay', *Journal of Geotechnical and Geoenvironmental Engineering* **128**(11).
- Trondheim Municipality (2012), Esp-byneset, kvikkleireskred, Technical Report R.1527, Trondheim Municipality. (In Norwegian).
- Viggiani, G. and Atkinson, J. H. (1995), 'Interpretation of bender elements', *Géotechnique* **45**(1).
- Vucetic, M. and Dobry, R. (1991), 'Effect of soil plasticity on cyclic response', *Journal of Geotechnical Engineering* **117**.
- Wang, Y. H., Lo, K. F., Yan, W. M. and Dong, X. B. (2007), 'Measurement biases in the bender element test', *Journal of Geotechnical and Geoenvironmental Engineering*.
- Westerlund, G. J. (1978), Undersøkelser av dynamisk skjærmodul i leire, PhD thesis, NTH. (In Norwegian).
- Xia, J., Miller, R. D. and Park, C. B. (1999), 'Estimation of near-surface shear-wave velocity by inversion of rayleigh waves', *Geophysics* **64**(3).
- Youn, J.-U., Choo, Y.-W. and Kim, D.-S. (2008), 'Measurement of small-strain shear modulus  $G_{max}$  of dry and saturated sands by bender element, resonant column, and torsional shear tests', *Canadian Geotechnical Journal*.
- Yu, P. and Richart, F. E. J. (1984), 'Stress ratio effects on shear modulus of dry sands', *Journal of Geotechnical Engineering* **110**.

- Zhou, Y.-g. and Chen, Y.-m. (2005), 'Influence of seismic cyclic loading history on small strain shear modulus of saturated sands', *Soil Dynamics and Earthquake Engineering* **25**(5), 341-353.



## List of Symbols

$\epsilon_a$	Axial strain
$\eta$	Viscosity
$\gamma$	Shear strain
$\gamma_c$	Cyclic shear strain
$\lambda$	Wavelength
$\nu$	Poisson's ratio
$\omega$	Angular frequency
$\phi$	Friction angle
$\rho$	Density
$\rho_s$	Density of soil grains
$\sigma_h$	Total horizontal stress
$\sigma'_h$	Effective horizontal stress
$\sigma'_m$	Mean effective stress
$\sigma_r$	Reference stress
$\sigma_v$	Total vertical stress
$\sigma'_v$	Effective vertical stress
$\tau$	Shear stress
$\tau_c$	Cyclic shear stress
$\xi$	Damping ratio
$A$	Area
$a$	Attraction
$c_v$	Consolidation coefficient
$e$	Void ratio
$E_{oed}$	Oedometer modulus
$f$	Frequency

$F$	Force
$G$	Shear modulus
$G^*$	Frequency independent shear modulus
$G_{max}$	Small strain shear modulus
$G_{sec}$	Secant shear modulus
$G_{tan}$	Tangential shear modulus
$I$	Polar moment of inertia
$I_p$	Plasticity index
$K'_0$	Stress ratio, $\sigma'_3/\sigma'_1$
$L_{tt}$	Tip-to-tip travel distance of s-wave
$m$	Modulus number
$M$	Deformation modulus
$n$	Porosity
$OCR$	Overconsolidation ratio
$p'$	Mean effective stress
$P(t)$	Force
$p_a$	Atmospheric pressure
$p'_c$	Preconsolidation stress
$q$	Deviator stress
$s_r$	Remoulded shear strength
$S_t$	Sensitivity
$s_u$	Undrained shear strength
$t_s$	Shear wave travel time
$u$	Displacement
$u_r$	Suction
$V$	Volume

## BIBLIOGRAPHY

---

$v_p$	Compressional (primary) wave velocity
$v_R$	Rayleigh wave velocity
$v_s$	Shear wave velocity
$w$	Water content
$W_D$	Dissipated energy during one cycle
$w_l$	Liquid limit
$w_p$	Plastic limit
$W_S$	Maximum energy dissipated during one cycle (Maximum elastic work)



# List of Figures

2.1	Energy dissipation. . . . .	6
2.2	Variation in shear modulus and damping ratio with shear strain. . . . .	7
2.3	Kelvin-Voigt element subjected to shearing. . . . .	7
2.4	Hysteresis loop for viscous damper. . . . .	8
2.5	Propagating wave divided into infinitesimal elements. . . . .	11
2.6	P-wave illustration. . . . .	13
2.7	S-wave illustration. . . . .	15
2.8	Rayleigh-wave illustration. . . . .	16
2.9	Variation of wave propagation velocities. . . . .	17
2.10	Hysteresis loop showing secant and tangent shear modulus .	19
2.11	Backbone curve and modulus reduction curve . . . . .	20
3.1	Resonant column test apparatus. . . . .	23
3.2	Schematic illustration of bender elements. . . . .	24
3.3	Piezoelectric bender element. . . . .	25
3.4	Waves generated by bender elements. . . . .	25
3.5	Torsional simple shear test . . . . .	27
3.6	Seismic reflection test . . . . .	30
3.7	Seismic refraction test test . . . . .	31
3.8	Velocity reversal, a limitation of the seismic refraction test .	33
3.9	Steady-state vibration (Rayleigh wave) test . . . . .	34
3.10	Spectral Analysis of Surface Waves Test . . . . .	36

3.11 Seismic cross-hole test . . . . .	38
3.12 Seismic down-hole (up-hole) test . . . . .	40
3.13 Seismic cone penetration test (up-hole) test . . . . .	42
3.14 Example of opposite polarized shear wave traces. . . . .	45
3.15 Influence of effective mean stress on shear modulus . . . . .	49
3.16 Location of the Stjørdal site. . . . .	52
3.17 Modulus reduction curves for fine grained soils of different placticity. . . . .	57
3.18 Degradation of shear modulus with cyclic loading. . . . .	60
3.19 Volume-change mechanisms of different structures. . . . .	62
4.1 Illustration of jig for bender element testing in field . . . . .	67
5.1 Test setup with bender elements protruded into clay sample. . . . .	74
5.2 DAQ with amplifiers connected to bender elements . . . . .	75
5.3 Pedestal and top-cap with fitted bender elements. . . . .	75
6.1 Location of the Esp site. . . . .	78
6.2 Landslide pit at Esp, Byneset. . . . .	79
6.3 Illustration of the setup of the cross-hole test performed at Esp, Byneset. . . . .	81
6.4 LabView software showing output from cross-hole testing. . . . .	82
6.5 Determination of inclination of tubes with accelerometers used for cross-hole test. . . . .	83
6.6 Directions of horizontal strikes during cross-hole testing. . . . .	84
7.1 Setup of clay sample in triaxial apparatus . . . . .	86
7.2 Example of output window showing transmitted and re- ceived wave. . . . .	88
7.3 Location of the Stjørdal site. . . . .	89
7.4 Location of the Tiller site. . . . .	92
8.1 Close-up of received signal from cross-hole testing at Esp, Byneset. Test 4. . . . .	109

LIST OF FIGURES

---

9.1 Wave propagation situation during cross-hole testing. . . . . 114

9.2 Similarity of waveform at A1 and A2. . . . . 115

9.3 Change in polarity of s-waves at A1 . . . . . 116

9.4 Change in polarity of s-waves at A2 . . . . . 117

9.5 Response from cross-hole test in distance-time diagram . . . 121

10.1 Stress-strain curve with  $G_{max}$  comparison for the first shear test performed on Stjørdal clay. . . . . 135

10.2 Stress-strain curve with  $G_{max}$  comparison for the second shear test performed on Stjørdal clay. . . . . 136

10.3 Stress-strain curve with  $G_{max}$  comparison for shear test performed on Tiller clay. . . . . 137

10.4 Stress-strain curve with  $G_{max}$  comparison for Esp clay. . . . 138

10.5 Variation in  $v_s$  with time of consolidation, Tiller clay. . . . 141

10.6 Close-up of  $v_s$  variation of Tiller clay with time of consolidation. . . . . 141

10.7  $V_s$  variation of Esp clay with time of consolidation. . . . . 142

10.8  $V_s$  variation of Stjørdal clay with time of consolidation. . . 142

10.9 Principle drawing of signal for bender element test on short sample. . . . . 146

10.10 Variation in  $v_s$  with time of consolidation, short sample. . . 146

B.1 LabView Block Diagram. . . . . 174

C.1 Results of CRS oedometer, Esp clay . . . . . 177

C.2 Grain size distribution of Esp clay . . . . . 178

C.3 Results of index testing, Esp clay . . . . . 179

E.1 Total received signal of cross-hole test 1. . . . . 189

E.2 Close-up of received signal of cross-hole test 1. Y-directional response. . . . . 190

E.3 Close-up of received signal of cross-hole test 1. Z-directional response. . . . . 191

E.4 Total received signal of cross-hole test 2. . . . . 193

E.5	Close-up of received signal of cross-hole test 2. . . . .	194
E.6	Total received signal of cross-hole test 3. . . . .	196
E.7	Close-up of received signal of cross-hole test 3. . . . .	197
E.8	Total received signal of cross-hole test 4. . . . .	199
E.9	Close-up of received signal of cross-hole test 4. . . . .	200
E.10	Total received signal of cross-hole test 5. . . . .	202
E.11	Close-up of received signal of cross-hole test 5. . . . .	203
E.12	Total received signal of cross-hole test 6. . . . .	205
E.13	Close-up of received signal of cross-hole test 6. . . . .	206
E.14	Total received signal of cross-hole test 7. . . . .	208
E.15	Close-up of received signal of cross-hole test 7. . . . .	209
E.16	Total received signal of cross-hole test 8. . . . .	211
E.17	Close-up of received signal of cross-hole test 8. . . . .	212
F.1	Stress path, Stjørdal clay. . . . .	215
F.2	Stress-strain plot, Stjørdal clay. . . . .	215
F.3	Stress path, Tiller clay . . . . .	217
F.4	Stress-strain plot, Tiller clay. . . . .	217
F.5	Stress path, Esp clay. . . . .	218
F.6	Stress-strain plot, Esp clay. . . . .	218
G.1	Variation in $v_s$ with time of consolidation, Stjørdal clay. . .	220
G.2	$V_s$ variation with time of consolidation, first test on Esp clay.	221
G.3	$V_s$ variation of Esp clay for the first 90 min of consolidation.	222
G.4	$v_s$ variation with time of consolidation, second test on Esp clay. . . . .	222
G.5	$V_s$ variation during first 60 min of consolidation, second test on Esp clay . . . . .	223
G.6	$V_s$ variation with time of consolidation, half-height sample.	223
G.7	Variation in $v_s$ with time of consolidation . . . . .	225
H.1	Change in polarity of s-waves during cross-hole testing. . .	228
H.2	S-wave identification . . . . .	229



# List of Tables

3.1	Assessment of field tests. . . . .	29
3.2	Influencing factors on $G_{max}$ and damping. . . . .	47
4.1	Evaluation of sample disturbance as quantified by $\Delta e/e_0$ . .	64
4.2	Evaluation of sample disturbance as quantified by $v_s/v_{SCPTU}$	68
4.3	Evaluation of sample disturbance as quantified by $L_{vs}$ and $L_u$ . . . . .	70
6.1	Material properties of Esp clay. . . . .	80
7.1	Material properties for Stjørdal clay. . . . .	90
7.2	Material properties of Tiller clay. . . . .	94
8.1	$G_{max}$ values after consolidation and shear test . . . . .	100
8.2	Results of the first bender element test performed on Stjørdal clay. . . . .	101
8.3	Results of the second bender element test performed on Stjørdal clay. . . . .	102
8.4	Results of bender element test performed on Tiller clay. . .	103
8.5	Results of the first bender element test performed on Esp clay. . . . .	104
8.6	Results of the second bender element test performed on Esp clay. . . . .	105
8.7	Results of bender element test on short sample. . . . .	106

8.8 Parameters used for empirical determination of  $G_{max}$ . . . . . 107

8.9 Results from cross-hole testing at Esp, Byneset. . . . . 108

C.1 Parameters of Esp clay from index and oedometer testing . 176

D.1 Overconsolidtion Ratio Exponent, k. . . . . 182

F.1 Parameters resulting from shear testing. . . . . 214

# Appendix A

## Task Description

**MASTER DEGREE THESIS**

Spring 2014

Student: Mirjam Knutsen

**On determination of  $G_{\max}$  by bender element and cross-hole testing****BACKGROUND**

The small strain shear modulus,  $G_{\max}$ , is an important parameter in geodynamic problems and for advanced soil modelling.  $G_{\max}$  is influenced by several factors, which complicates the assessment and interpretation of test results. Due to sample disturbance, values measured in the laboratory may be lower than in the field. The use of  $G_{\max}$  as a measure of sample disturbance has previously been investigated.

This thesis is a continuation of the candidate's project thesis regarding implementation of bender elements in a triaxial apparatus at the NTNU geotechnical laboratory. The project was limited to some pilot tests and more testing in the laboratory is wanted. In addition, measurements of  $G_{\max}$  in the field is desirable.

**TASK****Task description**

$G_{\max}$  shall be determined using bender elements in the triaxial apparatus. Testing shall be performed on different clays, mainly from block samples. For evaluation of development of  $G_{\max}$  with time, long-term consolidation is wanted.

As a supplement to the laboratory testing a limited field testing program is suggested for comparison to laboratory values. A cross - hole shear wave testing method, performed at one of the sites where laboratory samples are taken, would be an advantage. The consequence on  $G_{\max}$  ( $v_s$ ) of sample disturbance / sample quality is of interest.

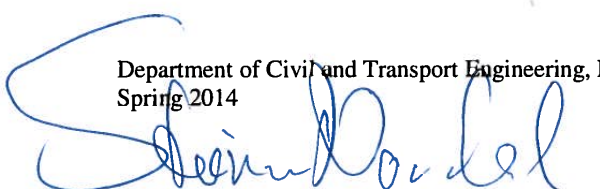
Difficulties regarding assessment and interpretation of test results shall be pointed out.

The task requires a literature study regarding parameters influencing  $G_{\max}$  and assessment of test results and sample disturbance.

**Objective and purpose**

- Evaluation of bender element testing.
- Investigation of development of  $G_{\max}$  with time
- Presentation of literature regarding determination of  $G_{\max}$  and interpretation of results, with an emphasis on bender elements.

Department of Civil and Transport Engineering, NTNU  
Spring 2014

  
Steinar Nordal, Professor in charge (signature)

Other supervisors: Prof. Gudmund Eiksund

## Appendix B

# LabView Block Diagram

Figure B.1 presents the block diagram from LabView used for the first bender element test performed on Stjørdal clay. This shows how the sine pulse applied to the bender element is built up, and how the output is presented during testing. The program was further developed throughout the time of study.

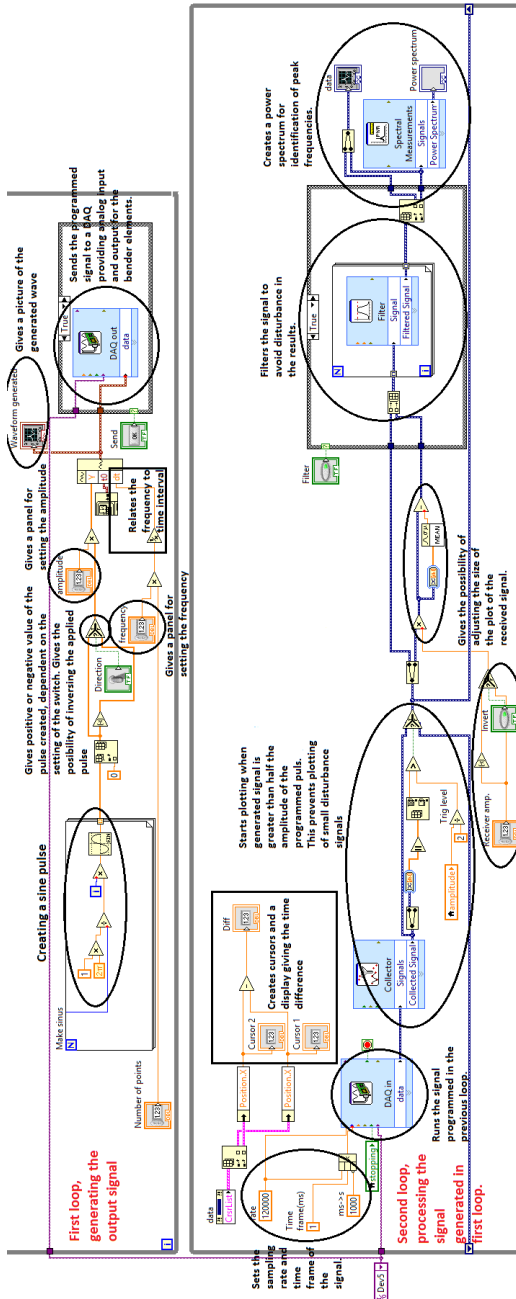


Figure B.1: LabView Block Diagram showing graphical programming of input signal.

## Appendix C

# Index Testing on the Esp Clay

Index testing and a continuous loading oedometer test of constant rate of strain (CRS) is performed on an Esp clay sample from 8.27 m depth. Date of sampling was 09.05.14, and the tests were run 12.05.14, the same day as the sample was opened. This was the same block sample as that used for bender element testing.

Results of the index testing is shown in Figure C.3, and a summary of the parameters is given in Table C.1.

Results of the oedometer test is presented in Figure C.1. From these plots, oedometer modulus,  $E_{oed}$ , modulus number,  $m$ , coefficient of consolidation,  $c_v$ , and preconsolidation stress,  $p'_c$ , was determined.  $OCR$  at the current depth was also calculated. Resulting values of these parameters are given in Table C.1.

The overconsolidation ratio at 8.3 m depth is found as the  $p'_c/\sigma'_v$  ratio, where  $\sigma'_v$  is the effective overburden pressure at the current depth (equation (7.9)). This is used for empirical determination of  $G_{max}$ .

The grain size distribution curve of Esp clay from 8.3 m depth, resulting from hydrometer analysis is presented in Figure C.2. This show a clay content of about 65 %, and the remaining material being fine to medium silt.

**Table C.1:** *Soil parameters resulting from index and CRS oedometer testing performed on block sample of Esp clay from 8.22-8.34 m depth.*

Parameters from index testing		
Density, $\rho$	1.886	[g/cm <sup>3</sup> ]
Density of soil grains, $\rho_s$	3.01	[g/cm <sup>3</sup> ]
Undrained shear strength, $s_u$	24	[kPa]
Remoulded undrained shear strength, $s_r$	0.2	[kPa]
Sensitivity, $S_t$	120	[-]
Plasticity index, $I_p$	24	[%]
Porosity, $n$	54	[%]
Void ratio, $e$	1.2	[-]
Water content, $w$	37.3	[%]
Parameters from CRS oedometer test		
Modulus, $E_{oed}$	4.5	[MPa]
Modulus number, $m$	17	[-]
Consolidation coefficient, $c_v$	40	[m <sup>2</sup> /year]
Preconsolidation stress, $p'_c$	200	[kPa]
OCR	2.6	[-]



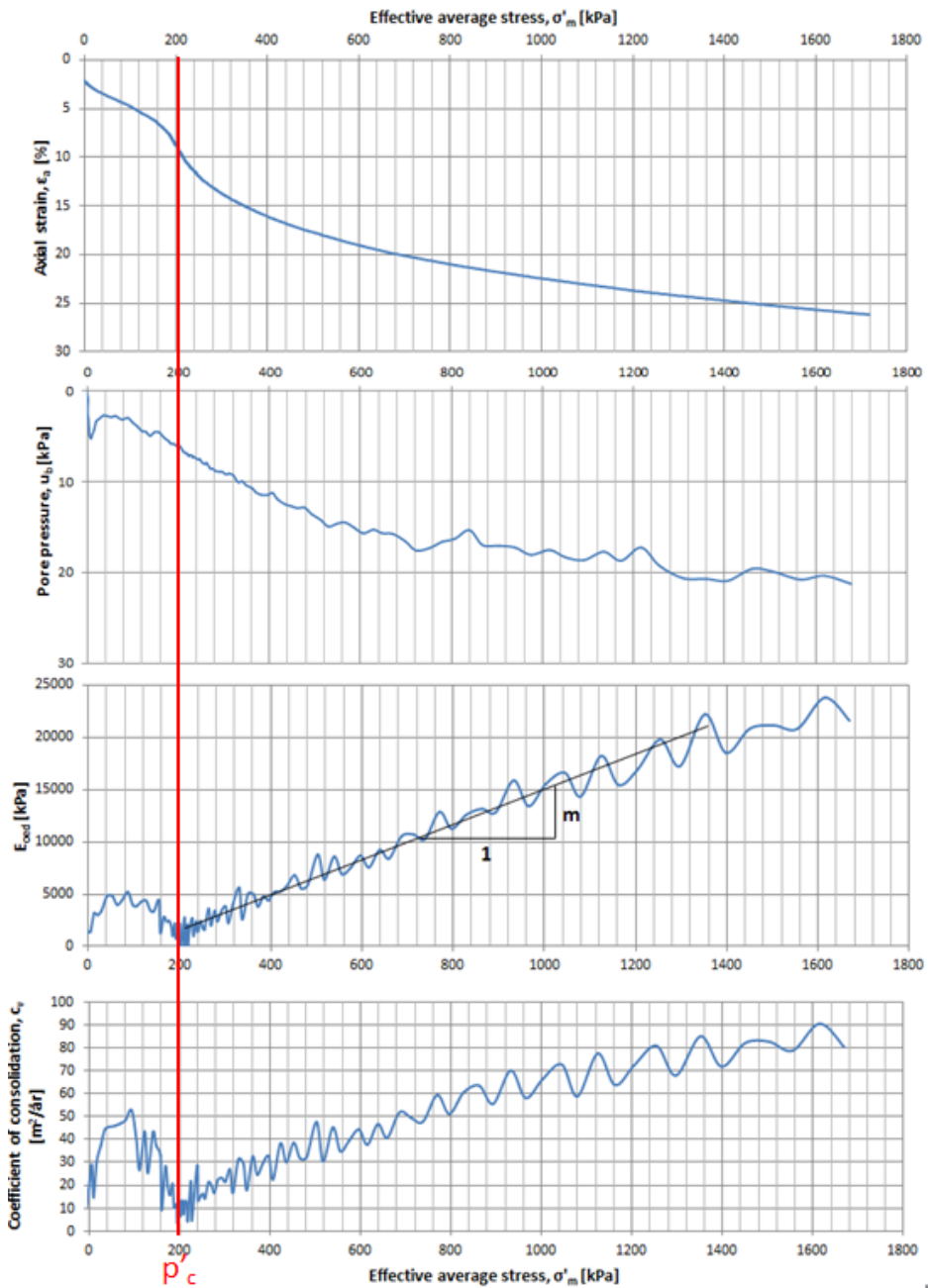
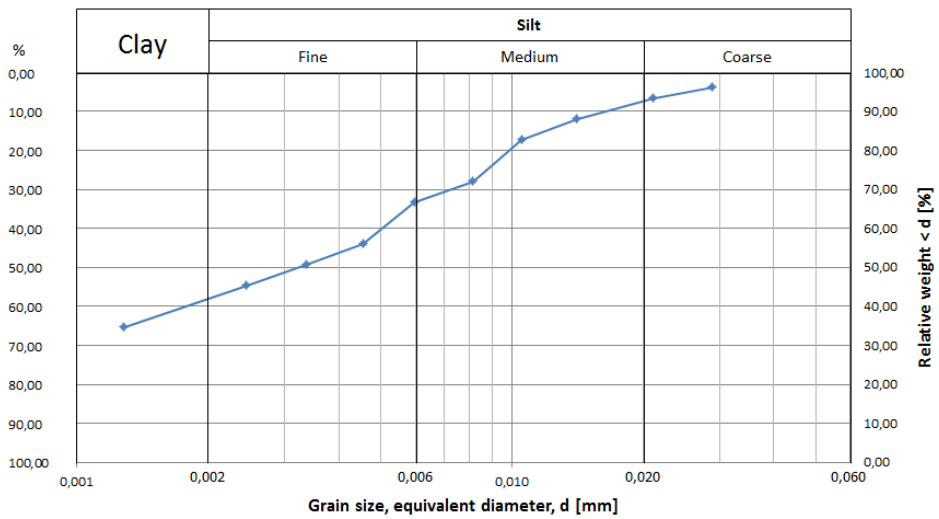


Figure C.1: Results from CRS oedometer test performed on an Esp clay sample from 8.27 m depth.



**Figure C.2:** Grain size distribution curve of Esp clay at 8.3 m depth, resulting from hydrometer analysis.

Date of sampling:	09.05.2014					
Date of sample opening:	12.05.2014					
Site:	Esp, Byneset					
Depth:	8,22-8,34 [m]					
<b>Pycnometer</b>		<b>Density from oedometer</b>				
Density water	0,997 g/cm <sup>3</sup>	Sample height, h <sub>0</sub>	2 [cm]			
Mass pycnometer + water	150,8 g	Sample diameter, d	5,05 [cm]			
Mass pycnometer+sample+water	154,51 g	Sample Area, A	20,0296 [cm <sup>2</sup> ]			
Total dry mass	298,43 g	Sample Volume, V <sub>0</sub>	40,0592 [cm <sup>3</sup> ]			
Mass of cup	292,88 g	Mass oedometer ring+sample	114,82 [g]			
Mass of dry sample	5,55 g	Mass oedometer ring	39,27 [g]			
Density of soil grains	3,01 g/cm <sup>3</sup>	Mass sample	75,55 [g]			
		Mass dry sample	54,77 [g]			
<b>Index parameters</b>		Density	1,886 [g/cm <sup>3</sup> ]			
Liquid limit, w <sub>l</sub>	54,7 %					
Plastic limit, w <sub>p</sub>	30,7 %	<b>Falling cone</b>				
Plasticity index, I <sub>p</sub> =w <sub>l</sub> -w <sub>p</sub>	24 %	Sample no.	s <sub>u</sub> [kPa]	s <sub>r</sub> [kPa]	S <sub>t</sub>	
Flydeindeks I <sub>f</sub> =(w-w <sub>p</sub> )/(w <sub>l</sub> -w <sub>p</sub> )	0,273 %	1	24	0,2	120,0	
Porosity, n	54,54 %					
Void ratio, e	1,20					
Metningsgrad Sr	95,1 %					
<b>Water content, w [%]</b>	Sample 1	Sample 2	Sample 3	Average		
Cup no.	241	223	59			
Total wet mass [g]	67,56	69,02	81,88			
Total dry mass [g]	56	57,2	66,85			
Mass water [g]	11,56	11,82	15,03			
Mass of cup [g]	24,07	27,11	25,41			
Mass of dry sample [g]	31,93	30,09	41,44			
<b>Water content, w [%]</b>	36,2	39,3	36,3	<b>37,3</b>		

**Figure C.3:** Results of index testing performed on Esp clay from 8.22-8.34 m depth.



## Appendix D

# Empirical Determination of $G_{max}$

Hand calculations are performed to give an empirical value of  $G_{max}$  for each sample used for bender element testing. The  $G_{max}$  relationship given in equation (3.6) is used.

Hardin (1978) suggests  $A = 625$  and  $n = 0.5$ , hence this is used for the following calculations of  $G_{max}$ .

Two proposals for the function of void ratio,  $F(e)$  are given in section 3.3.3 (equations (3.11) and (3.12)). Both are evaluated, and consequently two values of  $G_{max}$  are calculated and presented here.

Values for the overconsolidation ratio exponent,  $k$ , is given in Table D.1.

The atmospheric pressure is taken as  $p_a = 100$  kPa.

**Table D.1:** *Overconsolidation Ratio Exponent,  $k$ . (From Hardin 1978.)*

Plasticity Index, $I_p$ [%]	$k$
0	0.00
20	0.18
40	0.30
60	0.41
80	0.48
$\geq 100$	0.50

## D.1 Stjørdal Clay

The clay samples from the Stjørdal site has plasticity index,  $I_p = 18\%$  (Table 7.1). Linear interpolation of the values in Table D.1 then gives  $k = 0.16$ .

The two suggestions for the function of void ratio given in Section 3.3.3 is determined using void ratio  $e = 0.904$ , as given for Stjørdal clay in Table 7.1. This gives:

$$F^1(e) = \frac{1}{(0.3 + 0.7e^2)} = \frac{1}{(0.3 + 0.7 \times 0.904^2)} = 1.147 \quad (\text{D.1})$$

$$F^2(e) = \frac{1}{e^{1.3}} = \frac{1}{0.904^{1.3}} = 1.140 \quad (\text{D.2})$$

### D.1.1 First Test

An error related to drainage led to a pore pressure of 22 kPa during consolidation (Table 8.2). Initial stresses as determined in equations (7.3) and (7.4) are adjusted by this, giving mean principal effective stress:

$$\sigma'_m = \frac{\sigma'_1 + 2\sigma'_3}{3} = \frac{(110.5 + 2 \times 84) \text{ kPa}}{3} = 93 \text{ kPa} \quad (\text{D.3})$$

Due to the drainage error during consolidation,  $OCR$  related to the initial state (Table 7.1) is corrected to the stress state actually present in the sample at the assumed end of consolidation. The preconsolidation stress is determined from initial  $OCR$ , and  $OCR$  related to the actual stress state is then determined from the stress ratio.

$$p'_c = \sigma'_{1,initial} \times OCR_{initial} = 132kPa \times 1.7 = 224kPa \quad (D.4)$$

$$OCR_{ny} = \frac{224}{110} = 2 \quad (D.5)$$

Assuming the function of void ratio  $F^1(e) = 1.147$ , the maximum shear modulus is calculated as:

$$\begin{aligned} G_{max}^1 &= 625 \times 1.147 \times 2^{0.16} \times 100^{1-0.5} \times 93^{0.5} \\ &= 77241kPa \approx 77MPa \end{aligned} \quad (D.6)$$

Assuming the function of void ratio  $F^2(e) = 1.140$ , the maximum shear modulus is calculated as:

$$\begin{aligned} G_{max}^2 &= 625 \times 1.140 \times 2^{0.16} \times 100^{1-0.5} \times 93^{0.5} \\ &= 76770kPa \approx 77MPa \end{aligned} \quad (D.7)$$

### D.1.2 Second Test

Initial stresses as determined in equations (7.5) and (7.6) gives the mean principal stress:

$$\sigma'_m = \frac{\sigma'_1 + 2\sigma'_3}{3} = \frac{(129.8 + 2 \times 103.8)kPa}{3} = 112.5kPa \quad (D.8)$$

Assuming the function of void ratio  $F^1(e) = 1.147$ , the maximum shear modulus is calculated as:

$$\begin{aligned} G_{max}^1 &= 625 \times 1.147 \times 2^{0.16} \times 100^{1-0.5} \times 112.5^{0.5} \\ &= 84954kPa \approx 85MPa \end{aligned} \quad (D.9)$$

Assuming the function of void ratio  $F^2(e) = 1.140$ , the maximum shear modulus is calculated as:

$$\begin{aligned} G_{max}^2 &= 625 \times 1.140 \times 2^{0.16} \times 100^{1-0.5} \times 112.5^{0.5} \\ &= 84436kPa \approx 84MPa \end{aligned} \quad (D.10)$$

## D.2 Tiller Clay

The clay sample from the Tiller site has plasticity index,  $I_p = 5.5\%$  (Table 7.2). Linear interpolation of the values in Table D.1 gives  $k = 0.05$ .

The two suggestions for the function of void ratio given in Section 3.3.3 is determined using void ratio  $e = 1.07$ , as given for the Tiller clay in Table 7.2. This gives:

$$F^1(e) = \frac{1}{(0.3 + 0.7e^2)} = \frac{1}{(0.3 + 0.7 \times 1.07^2)} = 0.908 \quad (D.11)$$

$$F^2(e) = \frac{1}{e^{1.3}} = \frac{1}{1.07^{1.3}} = 0.916 \quad (D.12)$$

Initial stresses as determined in equations (7.7) and (7.8) gives the mean principal stress:

$$\sigma'_m = \frac{\sigma'_1 + 2\sigma'_3}{3} = \frac{(93.3 + 2 \times 65.3)kPa}{3} = 74.6kPa \quad (D.13)$$

Assuming the function of void ratio  $F^1(e) = 0.908$ , the maximum shear modulus is calculated as:



$$\begin{aligned} G_{max}^1 &= 625 \times 0.908 \times 1.8^{0.05} \times 100^{1-0.5} \times 74.6^{0.5} \\ &= 50477kPa \approx 50MPa \end{aligned} \quad (D.14)$$

Assuming the function of void ratio  $F^2(e) = 0.916$ , the maximum shear modulus is calculated as:

$$\begin{aligned} G_{max}^2 &= 625 \times 0.916 \times 1.8^{0.05} \times 100^{1-0.5} \times 74.6^{0.5} \\ &= 50922kPa \approx 51MPa \end{aligned} \quad (D.15)$$

### D.3 Esp Clay

The clay sample from the Tiller site has plasticity index,  $I_p = 24\%$  (Table 6.1). Linear interpolation of the values in Table D.1 gives  $k = 0.20$ .

The two suggestions for the function of void ratio given in Section 3.3.3 is determined using void ratio  $e = 1.2$ , as given for the Esp clay in Table 6.1. This gives:

$$F^1(e) = \frac{1}{(0.3 + 0.7e^2)} = \frac{1}{(0.3 + 0.7 \times 1.2^2)} = 0.765 \quad (D.16)$$

$$F^2(e) = \frac{1}{e^{1.3}} = \frac{1}{1.2^{1.3}} = 0.789 \quad (D.17)$$

Initial stresses as determined in equations (7.9) and (7.10) gives the mean principal stress:

$$\sigma'_m = \frac{\sigma'_1 + 2\sigma'_3}{3} = \frac{(79.3 + 2 \times 63.4)kPa}{3} = 68.7kPa \quad (D.18)$$

Assuming the function of void ratio  $F_1(e) = 0.765$ , the maximum shear modulus is calculated as:

$$\begin{aligned} G_{max}^1 &= 625 \times 0.765 \times 2.6^{0.2} \times 100^{1-0.5} \times 68.7^{0.5} \\ &= 47975kPa \approx 48MPa \end{aligned} \tag{D.19}$$

Assuming the function of void ratio  $F_2(e) = 0.789$ , the maximum shear modulus is calculated as:

$$\begin{aligned} G_{max}^2 &= 625 \times 0.789 \times 2.6^{0.2} \times 100^{1-0.5} \times 68.7^{0.5} \\ &= 49480kPa \approx 49MPa \end{aligned} \tag{D.20}$$

## Appendix E

# Results of Cross-Hole Testing at Esp, Byneset

This appendix presents the total response registered by accelerometers A1 and A2 for all cross-hole tests performed at Esp, Byneset. For assessment of the shear wave arrival at A1 and A2, close-ups are made at intervals where the s-wave appeared evident. Arrows mark the points used for determination of time difference, i.e. the s-wave travel time. Largest deflections were observed in the y-direction. Hence, plots of the y-directional response alone, simplifying the identification of s-waves, were used for determination of  $v_s$ .

The software used for registration of the signals do not register the time of load application. It only displays a time interval of one second, and measured response can be displayed anywhere within this range. Hence, the time axes do not start at zero, but is a random time interval where signals were registered. Since only the difference in s-wave arrival times at A1 and A2 is of interest for determination of  $v_s$ , an adjustment putting  $t=0$  at the time of loading is considered not to be important.

## E.1 Cross-Hole Test 1

For test 1, a vertical strike of a sledge hammer on the steel rod served as source. Figure E.1 shows the total response registered by accelerometers A1 and A2.

A close-up used for determination of the s-wave travel time, and consequently  $v_s$  and  $G_{max}$ , is shown in Figure E.2.

The vertical strike of a sledge hammer was assumed to produce evident fluctuation in the z-(vertical) direction. This was not the case, however the z-directional response was greater for vertical strikes than for horizontal strikes. Figure E.3 shows a close-up of the response in z-direction for test 1. An assumed s-wave is quite evident at A1, but is very difficult to identify at A2. Hence, this plot is not suitable for determination of shear wave travel time, and  $v_s$ .

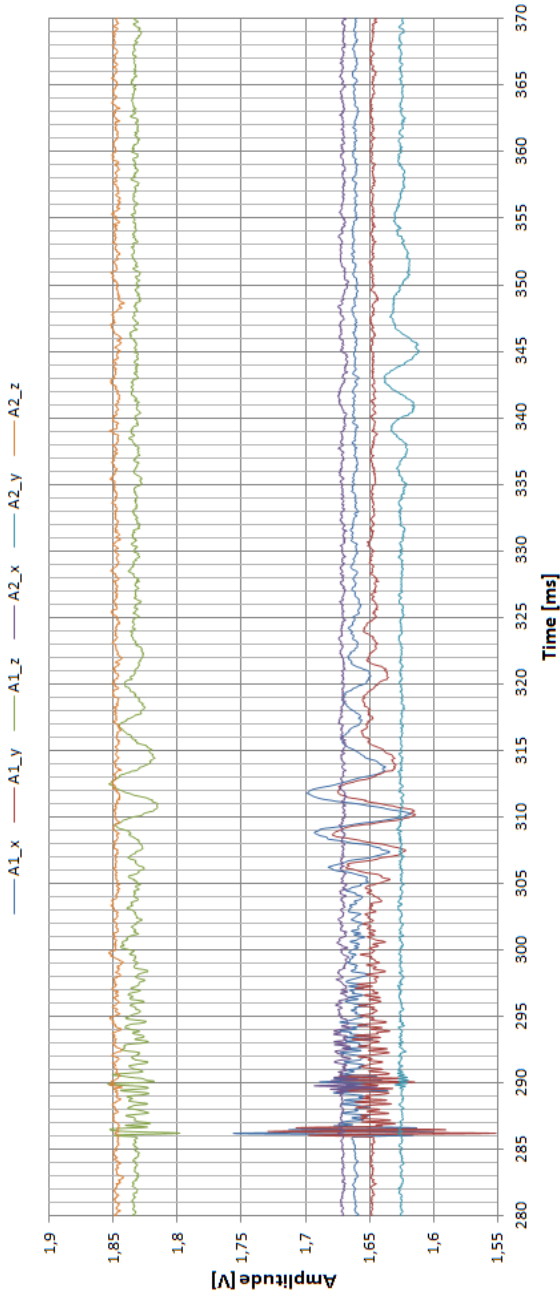


**Figure E.1:** Total range of received signals from cross-hole test number 1. The six curves represent response in  $x$ -,  $y$ - and  $z$ -directions at A1 and A2.

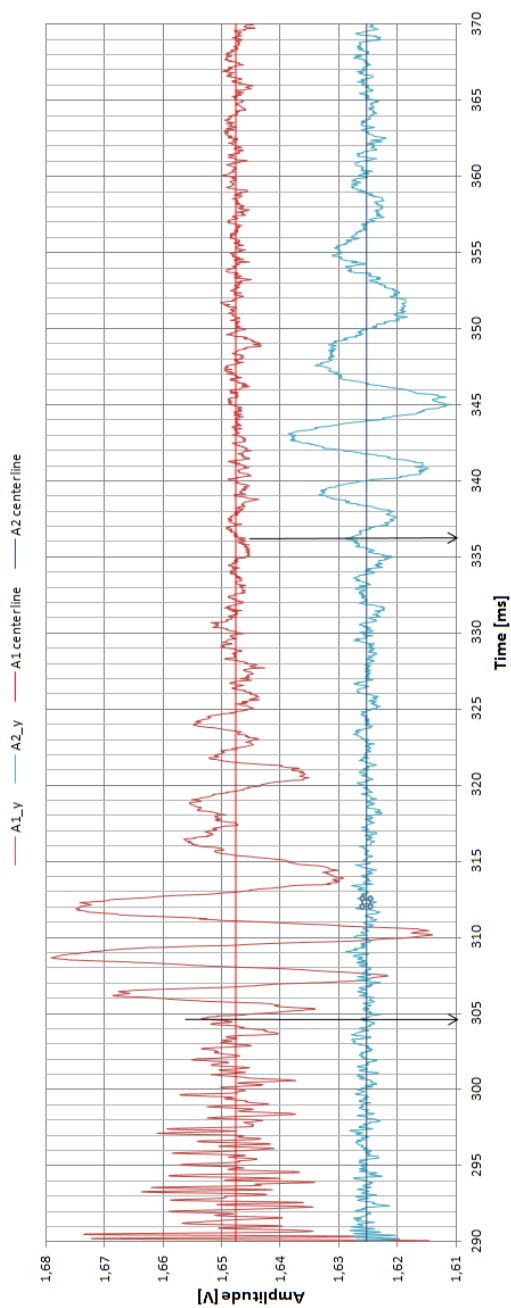


**Figure E.2:** Close-up of received signals from cross-hole test number 1, showing the range relevant for determination of  $v_s$ . Arrows mark the points of assumed s-wave arrivals from which s-wave travel time is determined. Both curves represent response in y-direction, the red curve at A1 and the blue curve at A2.

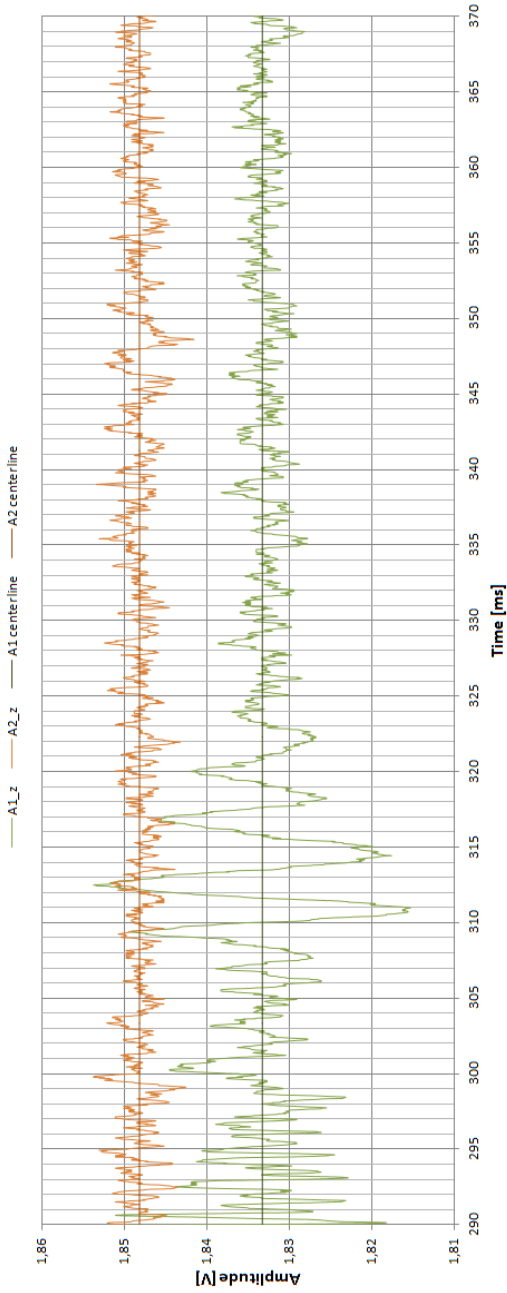


**Figure E.3:** Close-up of received signals from cross-hole test number 1, showing the range relevant for determination of  $v_s$ . Arrows mark the points of assumed s-wave arrivals from which travel time is determined. Both curves represent response in z-direction, the red curve at A1 and the blue curve at A2.

## E.2 Cross-Hole Test 2

For test 2, a horizontal strike of a sledge hammer served as source. The steel rod was struck normal to the direction of wave propagation, from left to right, defined when standing by the rod looking towards A1 and A2. An illustration clarifying the strike direction is presented in Figure 6.6.

Figure E.4 shows the total response registered by accelerometers A1 and A2.

A close-up used for determination of the s-wave travel time, and consequently  $v_s$  and  $G_{max}$ , is shown in Figure E.5.



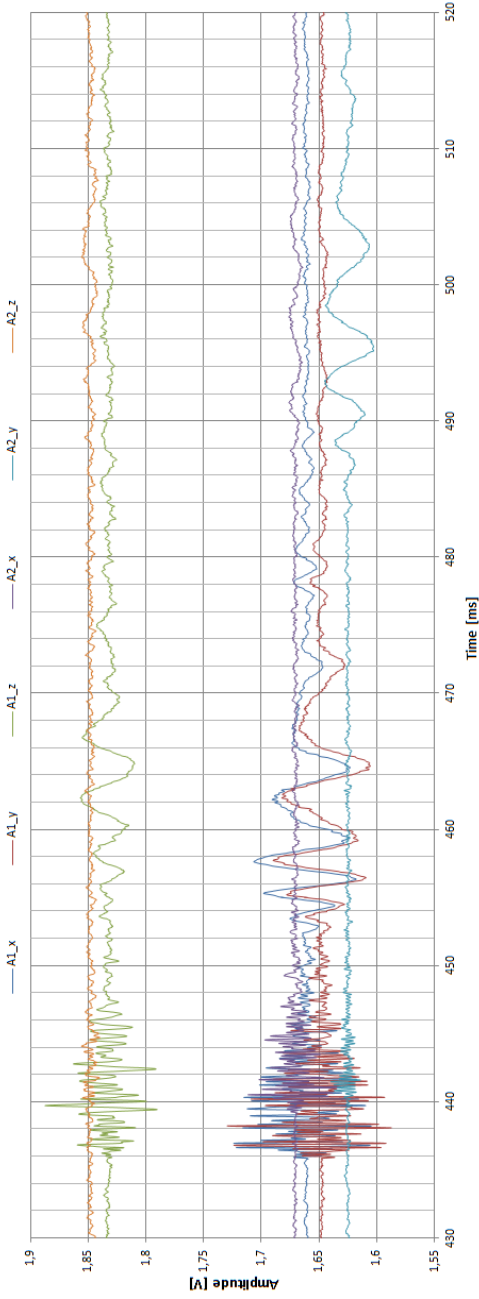


**Figure E.4:** Total range of received signals from cross-hole test number 2. The six curves represent response in  $x$ -,  $y$ - and  $z$ - directions at A1 and A2.

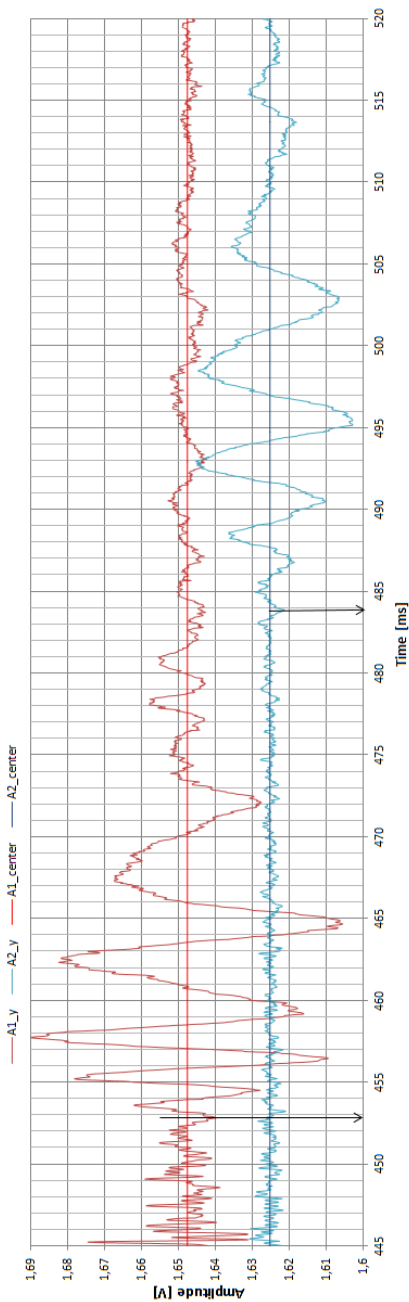


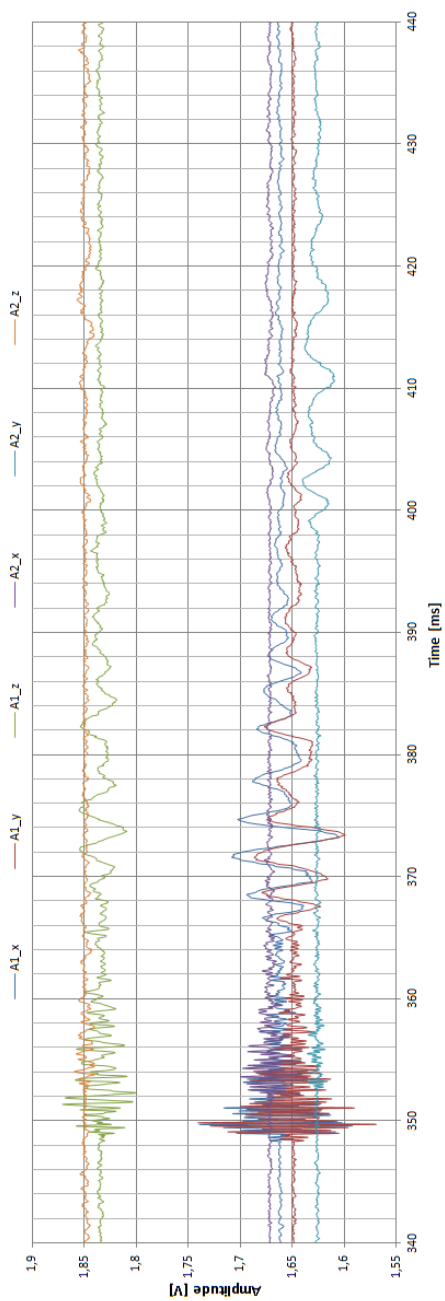
**Figure E.5:** Close-up of received signals from cross-hole test number 2, showing the range relevant for determination of  $v_s$ . Arrows mark the points of assumed s-wave arrivals from which travel time is determined. Both curves represent response in  $y$ -direction, the red curve at A1 and the blue curve at A2.

### E.3 Cross-Hole Test 3

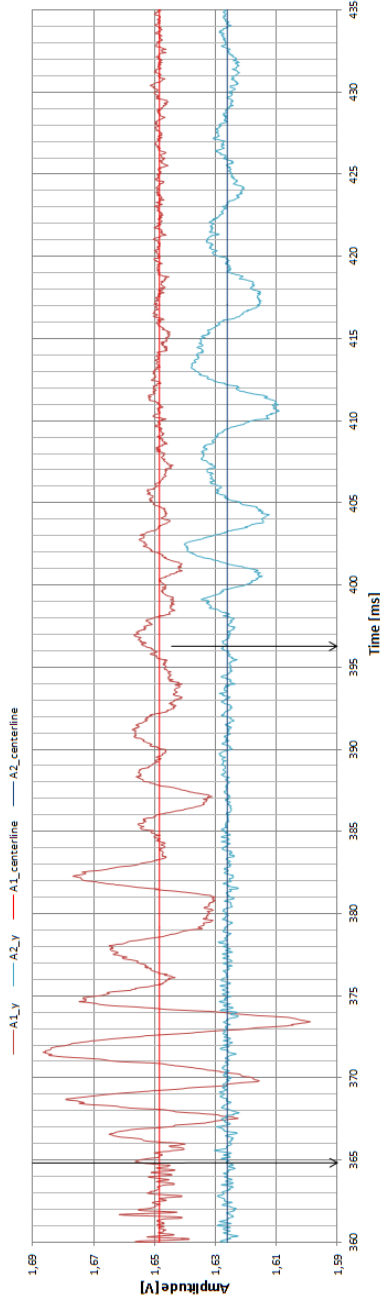
For test 3, a horizontal strike of a sledge hammer served as source. The steel rod was struck normal to the direction of wave propagation, from the right to the left, defined when standing by the rod looking towards A1 and A2. An illustration clarifying the strike direction is presented in Figure 6.6.

Figure E.6 shows the total response registered by accelerometers A1 and A2.

A close-up used for determination of the s-wave travel time, and consequently  $v_s$  and  $G_{max}$ , is shown in Figure E.7.



**Figure E.6:** Total range of received signals from cross-hole test number 3. The six curves represent response in  $x$ -,  $y$ - and  $z$ - directions at A1 and A2.



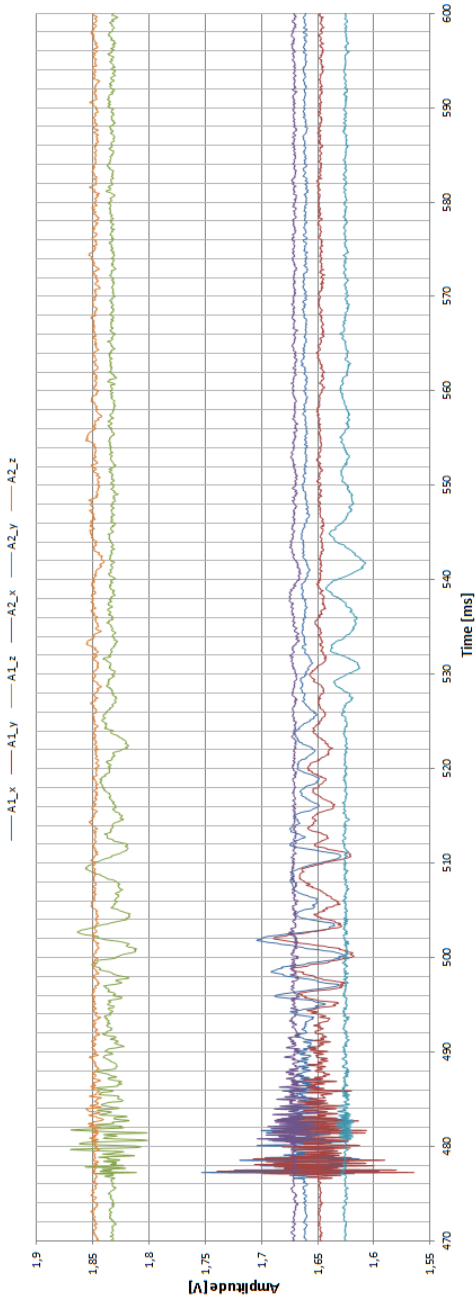
**Figure E.7:** Close-up of received signals from cross-hole test number 3, showing the range relevant for determination of  $v_s$ . Arrows mark the points of assumed s-wave arrivals from which travel time is determined. Both curves represent response in  $y$ -direction, the red curve at A1 and the blue curve at A2.

## E.4 Cross-Hole Test 4

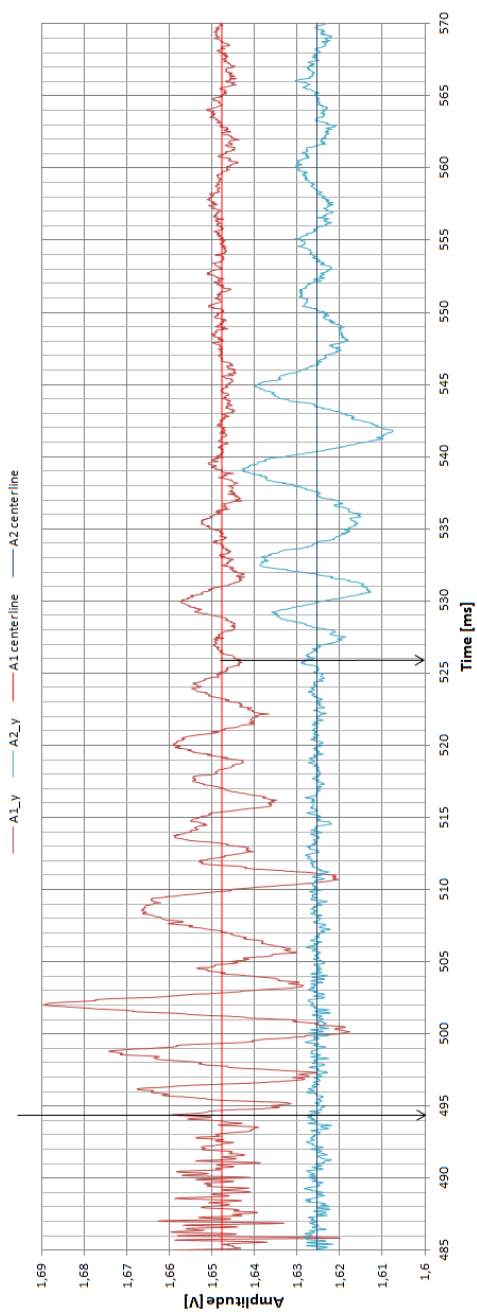
For test 4, a horizontal strike of a sledge hammer served as source. The steel rod was struck parallel, and in direction with wave propagation. An illustration clarifying the strike direction is presented in Figure 6.6.

Figure E.8 shows the total response registered by accelerometers A1 and A2.

A close-up used for determination of the s-wave travel time, and consequently  $v_s$  and  $G_{max}$ , is shown in Figure E.9.



**Figure E.8:** Total range of received signals from cross-hole test number 4. The six curves represent response in  $x$ -,  $y$ - and  $z$ -directions at A1 and A2.



**Figure E.9:** Close-up of received signals from cross-hole test number 4, showing the range relevant for determination of  $v_s$ . Arrows mark the points of assumed s-wave arrivals from which travel time is determined. Both curves represent response in  $y$ -direction, the red curve at A1 and the blue curve at A2.

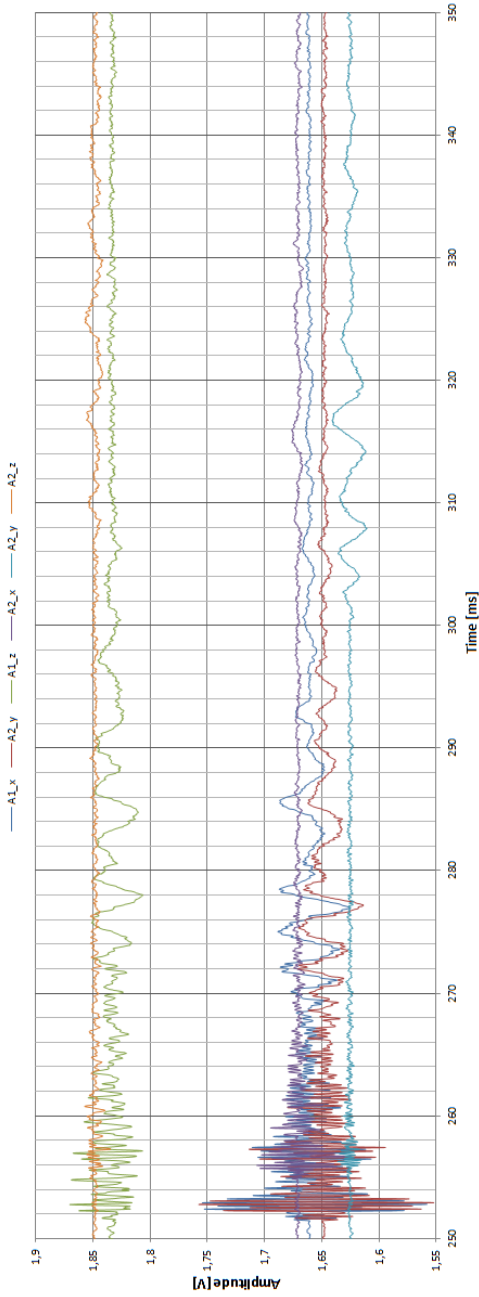


## E.5 Cross-Hole Test 5

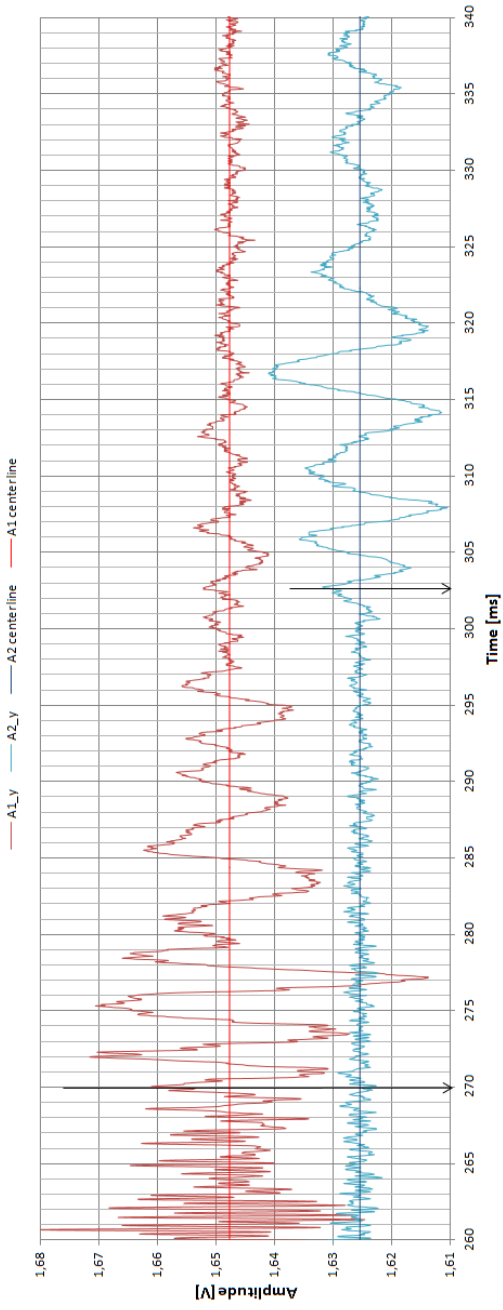
For test 5, a horizontal strike of a sledge hammer served as source. The steel rod was struck parallel to, but against the direction of wave propagation. An illustration clarifying the strike direction is presented in Figure 6.6.

Figure E.10 shows the total response registered by accelerometers A1 and A2.

A close-up used for determination of the s-wave travel time, and consequently  $v_s$  and  $G_{max}$ , is shown in Figure E.11.



**Figure E.10:** Total range of received signals from cross-hole test number 5. The six curves represent response in  $x$ -,  $y$ - and  $z$ - directions at A1 and A2.



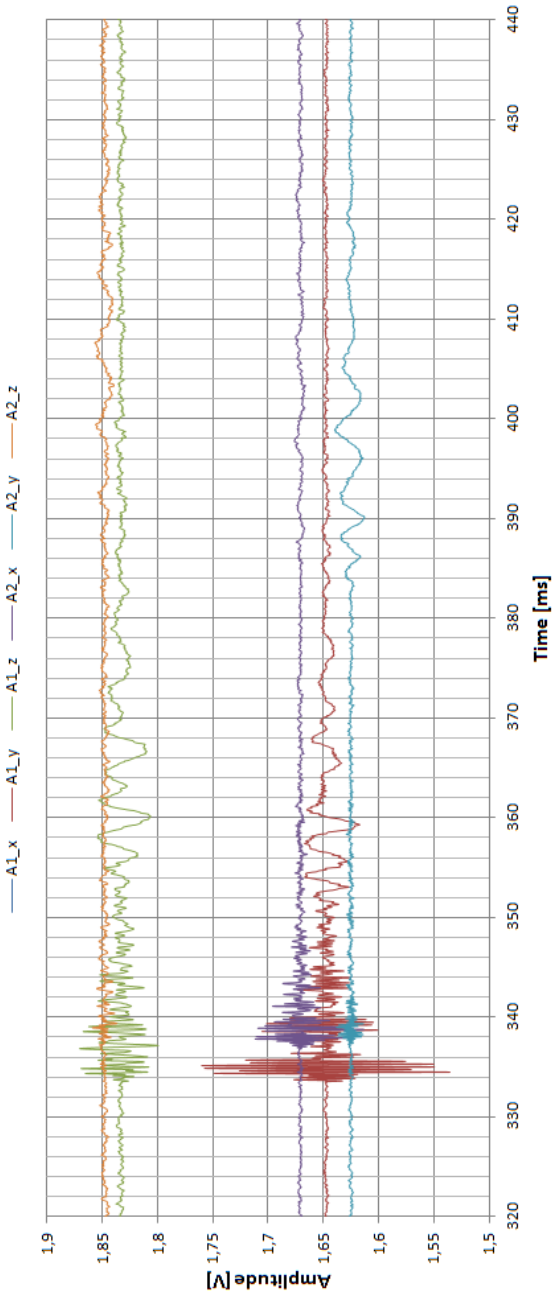
**Figure E.11:** Close-up of received signals from cross-hole test number 5, showing the range relevant for determination of  $v_s$ . Arrows mark the points of assumed s-wave arrivals from which travel time is determined. Both curves represent response in y-direction, the red curve at A1 and the blue curve at A2.

## E.6 Cross-Hole Test 6

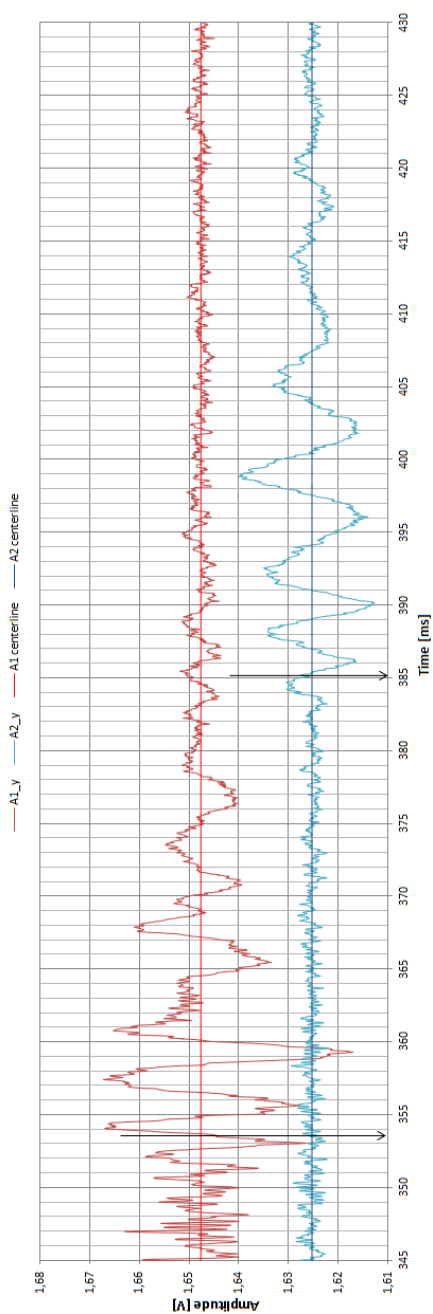
For test 6, a horizontal strike of a sledge hammer served as source. The steel rod was struck parallel to, but against the direction of wave propagation. An illustration clarifying the strike direction is presented in Figure 6.6.

Figure E.12 shows the total response registered by accelerometers A1 and A2.

A close-up used for determination of the s-wave travel time, and consequently  $v_s$  and  $G_{max}$ , is shown in Figure E.13.



**Figure E.12:** Total range of received signals from cross-hole test number 6. The six curves represent response in  $x$ -,  $y$ - and  $z$ - directions at A1 and A2.



**Figure E.13:** Close-up of received signals from cross-hole test number 6, showing the range relevant for determination of  $v_s$ . Arrows mark the points of assumed s-wave arrivals from which travel time is determined. Both curves represent response in y-direction, the red curve at A1 and the blue curve at A2.

## E.7 Cross-Hole Test 7

For test 7, a horizontal strike of a sledge hammer served as source. The steel rod was struck parallel, and in direction with wave propagation. An illustration clarifying the strike direction is presented in Figure 6.6.

Figure E.14 shows the total response registered by accelerometers A1 and A2.

A close-up used for determination of the s-wave travel time, and consequently  $v_s$  and  $G_{max}$ , is shown in Figure E.15.

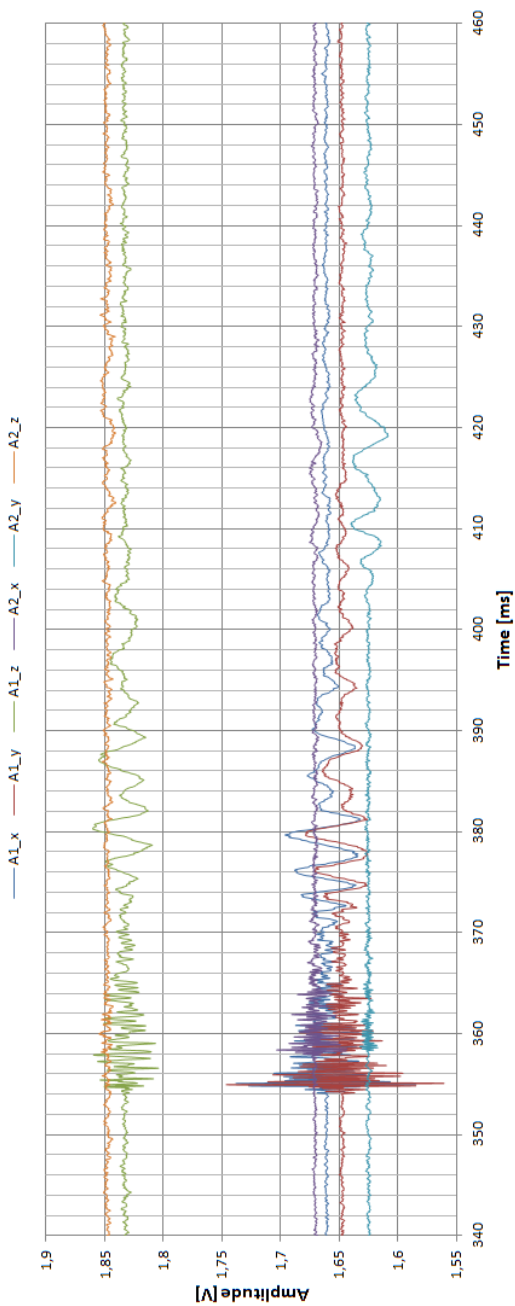


**Figure E.14:** Total range of received signals from cross-hole test number 7. The six curves represent response in  $x$ -,  $y$ - and  $z$ -directions at A1 and A2.



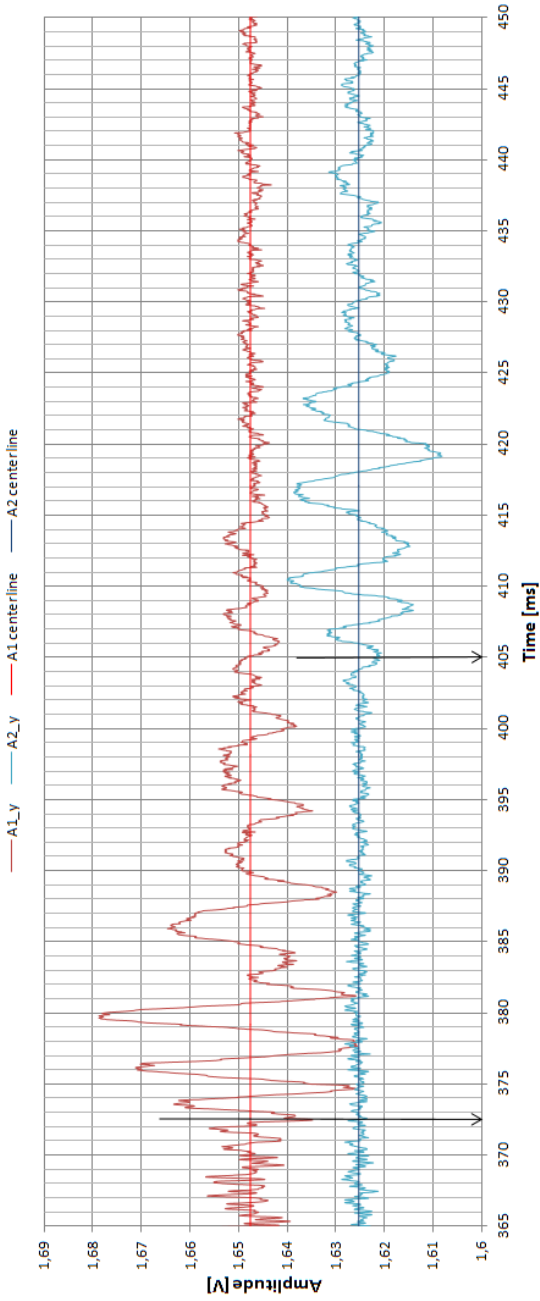


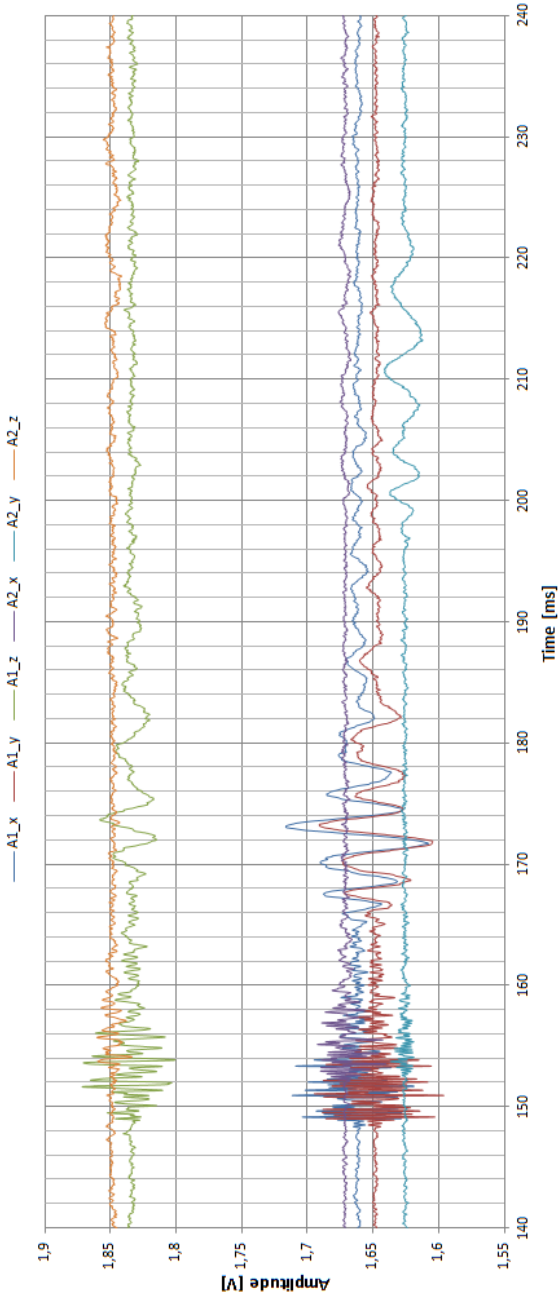
**Figure E.15:** Close-up of received signals from cross-hole test number 7, showing the range relevant for determination of  $v_s$ . Arrows mark the points of assumed s-wave arrivals from which travel time is determined. Both curves represent response in y-direction, the red curve at A1 and the blue curve at A2.

## E.8 Cross-Hole Test 8

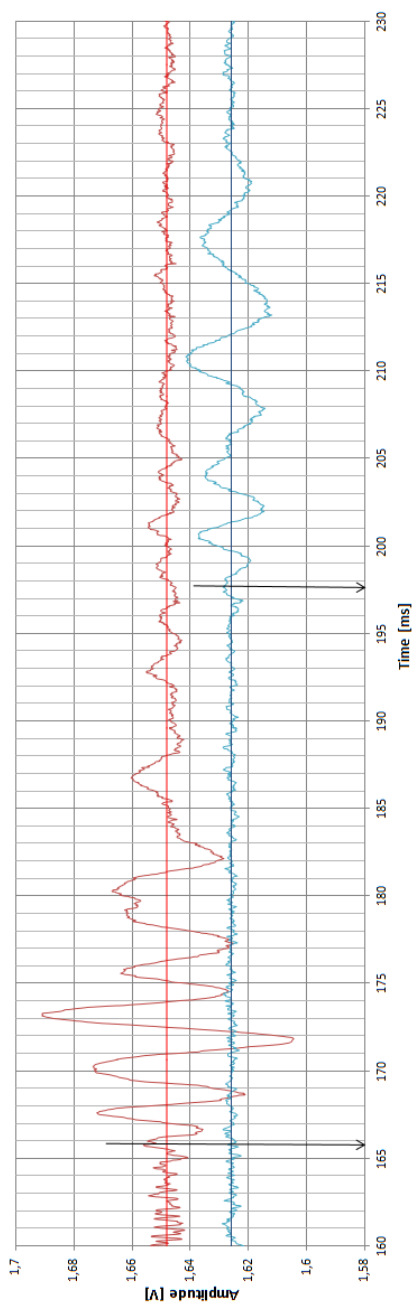
For test 8, a horizontal strike of a sledge hammer served as source. The steel rod was struck normal to the direction of wave propagation, from the right to the left, defined when standing by the rod looking towards A1 and A2. An illustration clarifying the strike direction is presented in Figure 6.6.

Figure E.16 shows the total response registered by accelerometers A1 and A2.

A close-up used for determination of the s-wave travel time, and consequently  $v_s$  and  $G_{max}$ , is shown in Figure E.17.



**Figure E.16:** Total range of received signals from cross-hole test number 8. The six curves represent response in  $x$ -,  $y$ - and  $z$ - directions at A1 and A2.



**Figure E.17:** Close-up of received signals from cross-hole test number 7, showing the range relevant for determination of  $v_s$ . Arrows mark the points of assumed s-wave arrivals from which travel time is determined. Both curves represent response in y-direction, the red curve at A1 and the blue curve at A2.

## Appendix F

# Results of Shear Tests

Shear tests were performed on samples from every site. All tests were run undrained. For information about the behavior of the soils, the results are presented here.

Resulting parameters, deformation modulus  $M$ , friction angle  $\phi$  and attraction  $a$ , is given in table F.1.

The modulus and friction angle is determined from equations (F.1) and (F.2).

$$q = M(p' + a) \quad (\text{F.1})$$

$$M = \frac{6 \sin \phi}{3 - \sin \phi} \quad (\text{F.2})$$

### The Stjørdal Clay

The stress path of the Stjørdal clay used for bender element testing is shown in Figure F.1. The sample shows an initial dilative behavior before

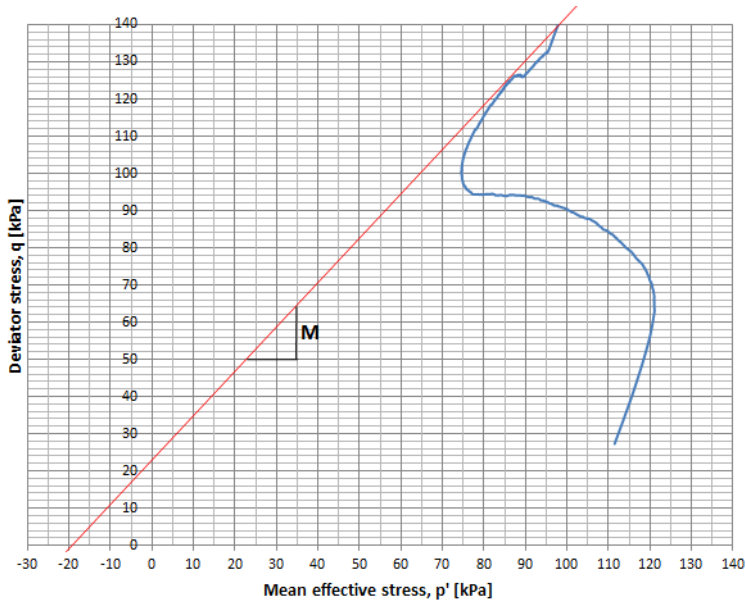
**Table F.1:** *Soil parameters resulting from shear tests.*

	Modulus, $M[-]$	Attraction, $a[kPa]$	Friction angle, $\phi[deg]$	$\tan\phi$ [-]
Stjørdal clay	1.19	19	30	0.573
Tiller clay	1.25	8	31	0.604
Esp clay	1.13	10	28	0.541

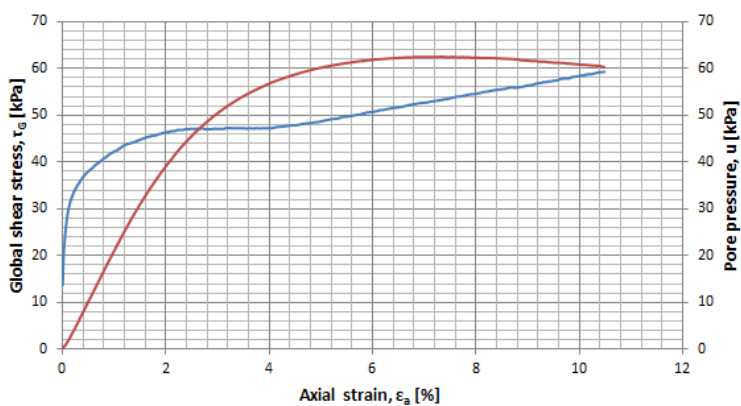
it contracts, and then dilates again. Also, the sample shows an initial drained behavior which is hard to explain.

Figure F.2 shows the development in shear stress with axial strain. The pore pressure is plotted in the same diagram, showing a normal build-up of pore pressure.

Testing performed on the same clay during the autumn of 2012, as part of the NTNU course Geotechnics, Field and Laboratory Investigations, showed  $\phi = 25^\circ$  and  $a = 17$  kPa. The results of this test (Table F.1) deviate some in comparison to previous results, but not to an unreasonable extent. The friction angle determined here is somewhat higher, giving some doubt to what results should be trusted.



**Figure F.1:** Stress path of Stjørdal clay, for the second test performed, shown with assumed failure line.



**Figure F.2:** Development in shear stress and pore pressure with axial strain during the second shear test performed on Stjørdal clay.

### **The Tiller Clay**

The stress path of the Tiller clay used for bender element testing is shown in Figure F.3. The clay show a contractive failure mechanism. Also, the sample shows an initial drained behavior which is hard to explain.

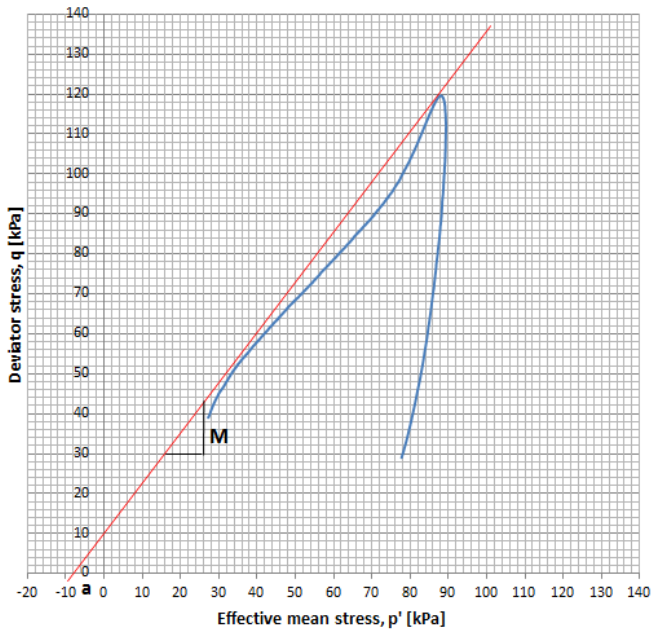
Figure F.4 show the development in shear stress with axial strain. The pore pressure is plotted in the same diagram, showing a build-up of pore pressure which may be somewhat low.

### **The Esp Clay**

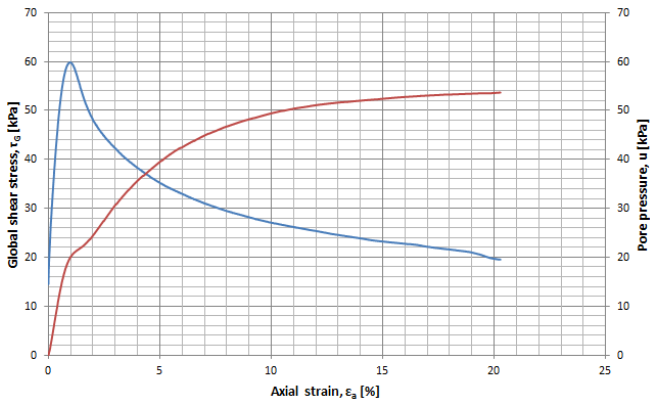
The stress path of the Esp clay used for bender element testing is shown in Figure F.5. The clay show a contractive failure mechanism, similar to that of the Tiller clay.

Figure F.6 show the development in shear stress and pore pressure with axial strain.





**Figure F.3:** *Stress path of Tiller clay. shown with assumed failure line.*



**Figure F.4:** *Development in shear stress and pore pressure with axial strain during shear test performed on Tiller clay.*

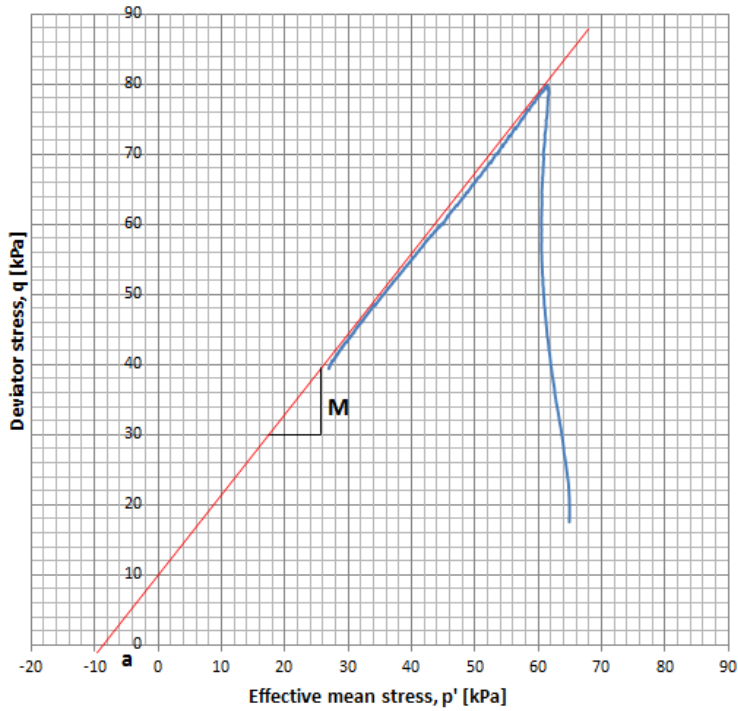


Figure F.5: Stress path of *Esp* clay, shown with assumed failure line.

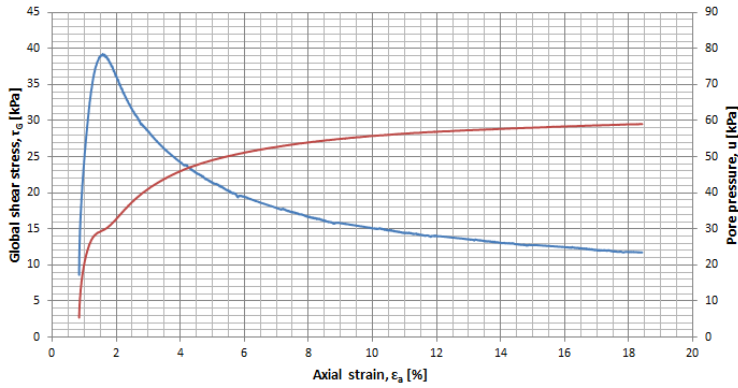


Figure F.6: Development in shear stress and pore pressure with axial strain during shear test performed on *Esp* clay.

## Appendix G

# Variation in $v_s$ with Time of Consolidation

### G.1 Observations from Bender Element Tests

#### Stjørdal Clay

Figure G.1 shows the variation in shear wave velocity,  $v_s$ , and axial strain,  $\varepsilon_a$ , with time of consolidation for the second bender element test performed on Stjørdal clay. A clear increase in  $v_s$ , and consequently  $G_{max}$ , is observed.

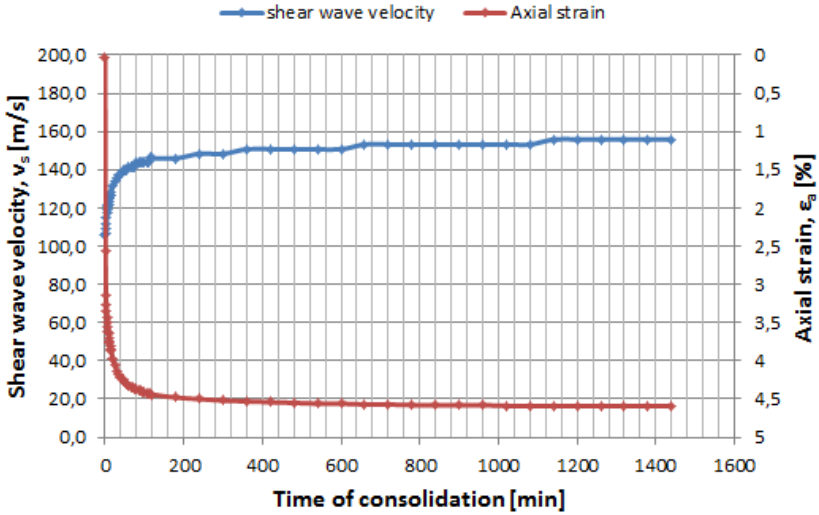


**Figure G.1:** Variation in shear wave velocity and vertical strain with consolidation time. The plot presents the results of the second bender element test performed on Stjørdal clay.

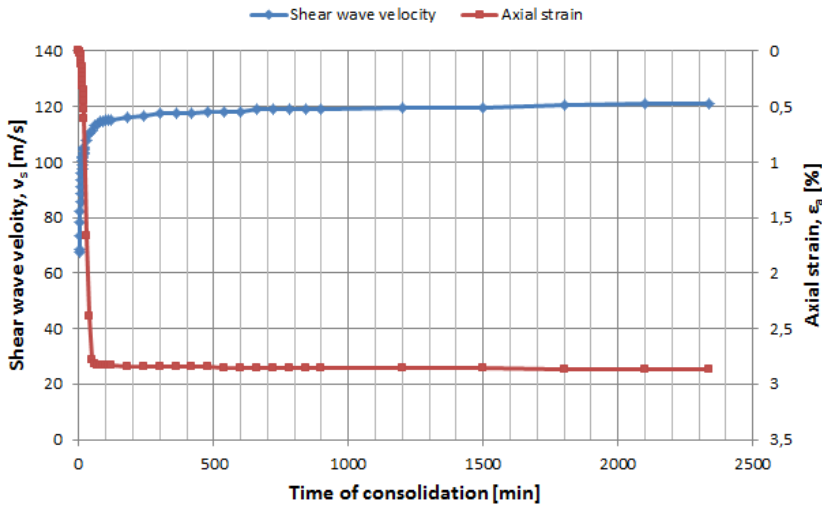
## Esp Clay

Figure G.2 shows the variation in  $v_s$  and  $\epsilon_a$  with time of consolidation for the first bender element test performed on Esp clay. The development of the first 90 minutes of consolidation is shown in Figure G.3. Although  $v_s$  is seen to level out some time before  $\epsilon_a$  stabilizes, the tendency of increasing  $v_s$  with increasing  $\epsilon_a$  is evident.

Figure G.4 shows the variation in  $v_s$  and  $\epsilon_a$  with time of consolidation for the second bender element test performed on Esp clay. The development of the first 60 minutes of consolidation is shown in Figure G.5, giving a more detailed view of the corresponding effects of increasing  $v_s$  with increasing  $\epsilon_a$ .

The effect of time of consolidation is similar for all tests, showing an increasing  $v_s$  with time. For the Esp clay, a larger increase is measured

during the second test than for than during the first. This may be related to sample quality. Both samples were taken from the same block sample, however the first sample was built in the triaxial apparatus the same day as the block was opened. The second test was run ten days after opening the block sample, hence the sample used for this test was expected to be somewhat more disturbed. Although measured  $v_s$  is lower at the start of the second test than the first, and show a larger increase in the initial consolidation phase, both tests level out at about the same values of  $v_s$ . This substantiates the validity of the tests.



**Figure G.2:** Variations in shear wave velocity and vertical strain with consolidation time. The plot presents the results of the first bender element test performed on Esp clay.

Figure G.6 shows the variation in  $v_s$  and  $\epsilon_a$  with time of consolidation for the bender element test performed on a half-height sample of Esp clay. The development in  $v_s$  with time is similar as for the longer samples, although the maximum value obtained is lower.

APPENDIX G. VARIATION IN  $V_S$  WITH TIME OF CONSOLIDATION

---

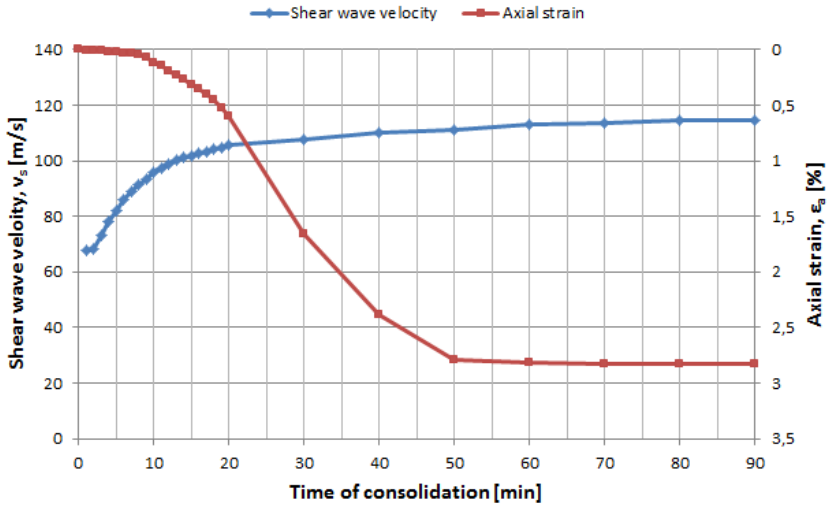


**Figure G.3:**  $V_s$  variation of *Esp* clay for the first 90 min of consolidation. Results presented are from the first bender element test performed on *Esp* clay.

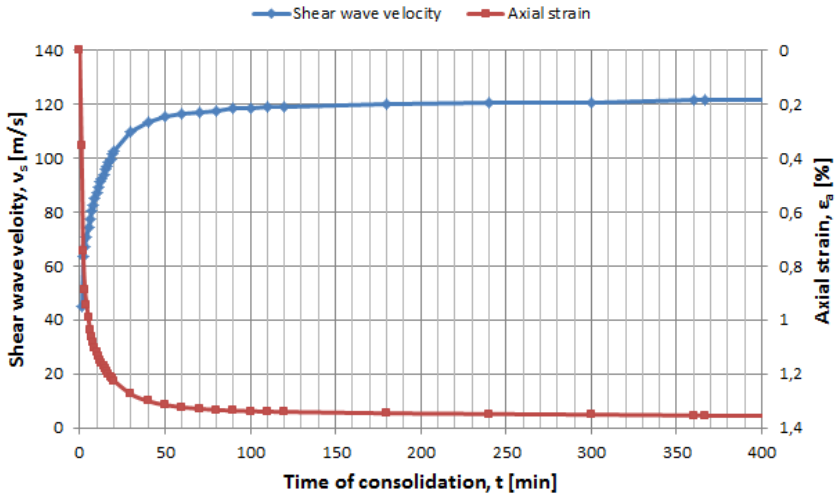


**Figure G.4:** Variations in shear wave velocity and vertical strain with consolidation time. The plot presents the results of the second bender element test performed on *Esp* clay.

## G.1. OBSERVATIONS FROM BENDER ELEMENT TESTS

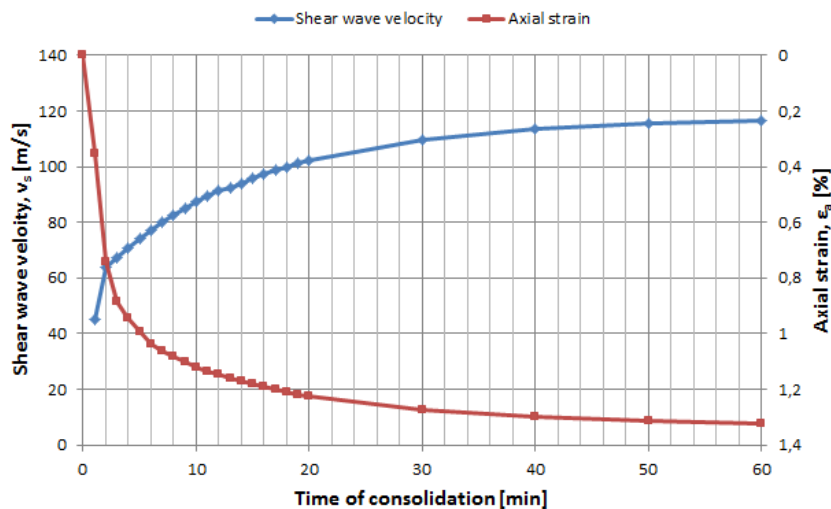


**Figure G.5:**  $V_s$  variation of *Esp* clay for the first 90 min of consolidation. The plot presents the results of the second bender element test performed on *Esp* clay.

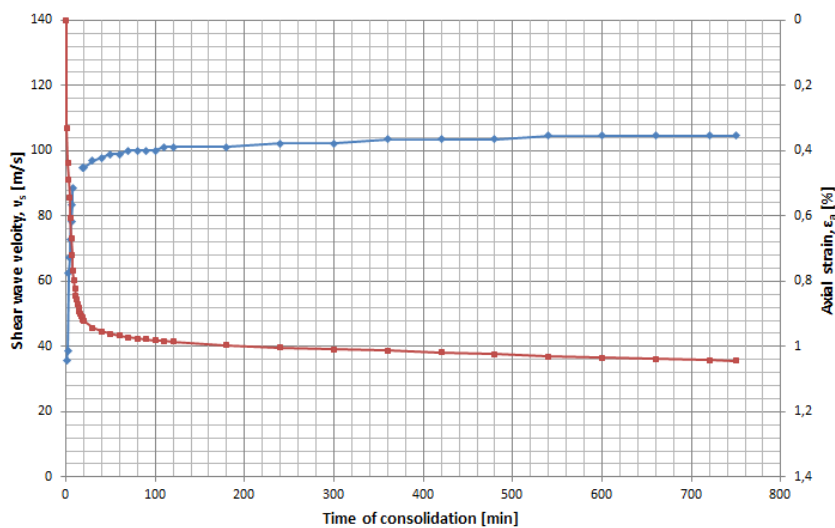


**Figure G.6:** Variations in shear wave velocity and vertical strain with consolidation time. The plot presents the results of the bender element test performed on a half-height sample of *Esp* clay.

## G.2 Observations from Previous Study

Figure G.7 presents variation in shear wave velocity with time of consolidation resulting from a resonant column test performed by Westerlund (1978). Long-term consolidation showed increasing  $G_{max}$  due to secondary effects (Westerlund, 1978). The results of this study matches the findings of Westerlund (1978).



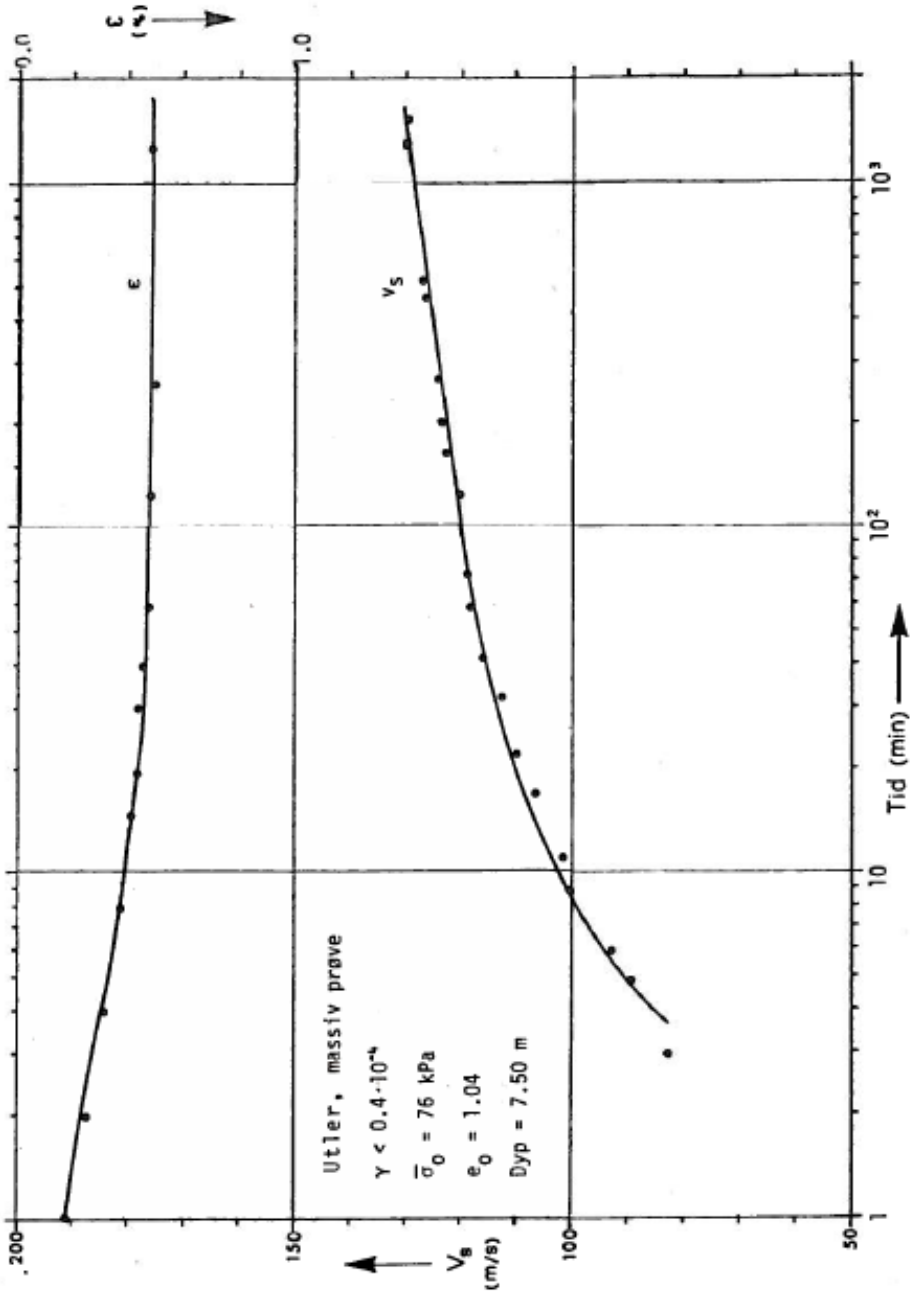


Figure G.7: Variation in  $v_s$  with time of consolidation observed by Westerlund (1978). (From Westerlund 1978.)

*APPENDIX G. VARIATION IN  $V_S$  WITH TIME OF  
CONSOLIDATION*

---

## Appendix H

# Signals of Opposite Polarity for Identification of the S-Wave

During cross-hole testing at Esp, Byneset, sources producing opposite initial particle motion were used. Observations of received signals of opposite polarity were used for a more reliable determination of the s-wave arrival time.

For test number 2 and 8, the rod was inflicted with hammer blows from opposite directions, for the purpose of reversing the signal. The signals received at A1 and A2 during test 2 and test 8 were plotted together for comparison. This is presented in Figure H.1.  $V_s = 155$  m/s and the distance between the rod and A1 (2 m) is used for extrapolation of the signals, giving a corresponding starting point in  $t = 0$ , assumed to be at the time of the hammer blow.

Figure H.2 shows the peaks used for determination of the s-wave travel time,  $t_s$ . The selection of these particular points was based on observations of opposite polarity.

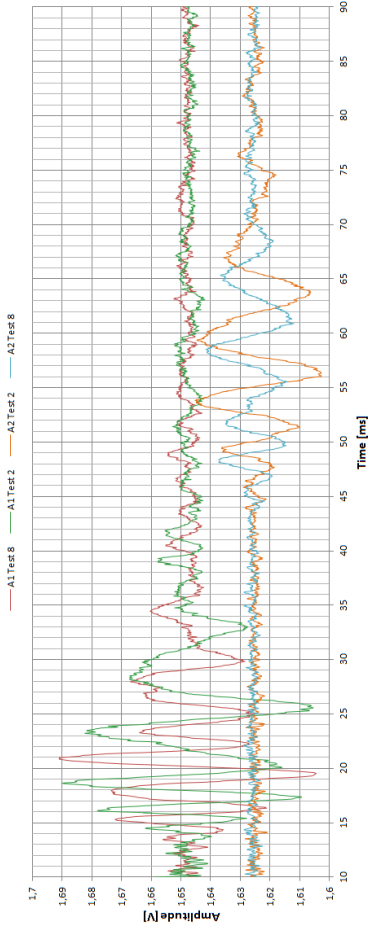


**Figure H.1:** During cross-hole test 2 and 8, the rod was inflicted with horizontal hammer blows of opposite direction. Signals registered at A1 and A2 show the resulting change in polarity of the s-wave.

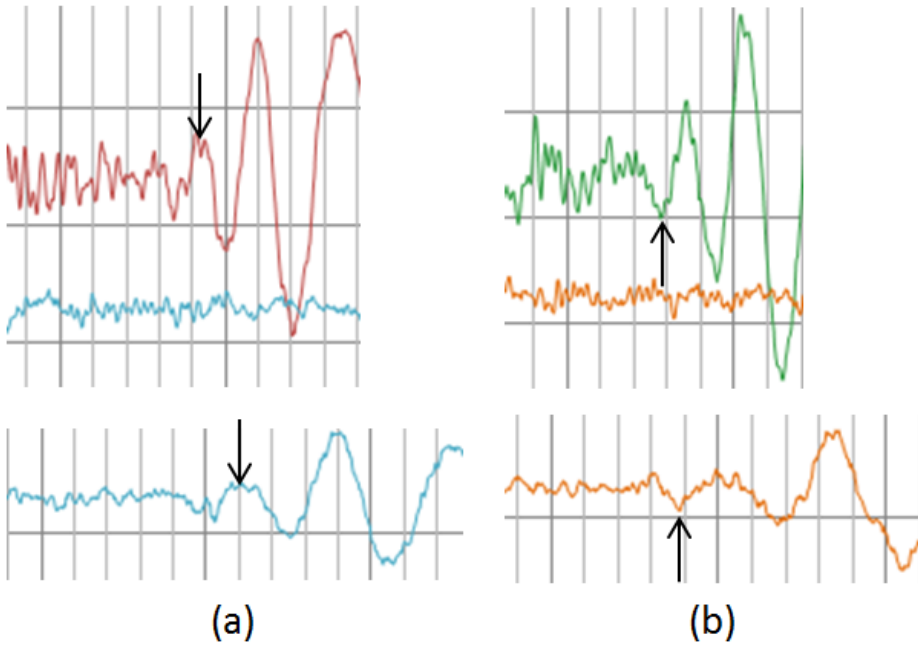


**Figure H.2:** *First peak of the s-wave identified based on observations of opposite polarities. (a) First peak of test 2. The red and blue curve represents signal registered at A1 and A2, respectively. (b) First peak of test 8. The green and orange curve represents signal registered at A1 and A2, respectively.*